Tesis defendida por

Mariana Jeannete Oviedo Bandera

y aprobada por el siguiente Comité

Dr. Gustavo Alonso Hirata Flores
Director del Comité

Dr. Oscar Edel Contreras López
Miembro del Comité

Dr. Joanna McKittrick
Miembro del Comité

Dr. Rafael Vazquez Duhalt
Miembro del Comité

Dr. Alexei Fedorovish Licea Navarro
Miembro del Comité

Dr. Felipe Francisco Castillón Barraza
Miembro del Comité

Dra. Laura Cecilia Viana Castrillón
Coordinador del Programa de Posgrado en Física de Materiales

Dr. David Hilario Covarrubias Rosales
Director de Estudios de Posgrado

29 de *octubre* de 2012

CENTRO DE INVESTIGACIÓN CIENTÍFICA Y DE EDUCACIÓN SUPERIOR DE ENSENADA

PROGRAMA DE POSGRADO EN CIENCIAS EN FISICA DE MATERIALES

Luminescent nanomaterials for biomedical applications

Thesis

Submitted in partial satisfaction of the requirements for the degree of Doctor of Science

Presents:

Mariana Jeannete Oviedo Bandera

CICESE, Ensenada, Baja California, México.
2012

Abstract of the thesis presented by Mariana Jeannete Oviedo Bandera as a partial requirement to obtain the Doctor of Science degree in Materials Physics. Ensenada, Baja California, México October. 2012.

Luminescent nanomaterials for biomedical applications

Abstract approved by:

_____

Dr. Gustavo Alonso Hirata Flores
Advisor

Synthetic hydroxyapatite ($Ca_{10}(PO_4)_6(OH)_2$, HA) exhibits excellent biocompatibility and has therefore been proposed for diverse medical applications. On the other hand, bismuth germanate ($Bi_4Ge_3O_{12}$, BGO) is commonly employed as high energy detector in industry and medicine. However, to the best of our knowledge, this is the first work that studies the biomedical applications of BGO nanoparticles. This work is focused on the production of europium-activated hydroxyapatite and bismuth germanate nanoparticles with low potential toxicity, stable luminescence properties in body fluids and capable of identifying human tumor cells.

HA activated with Eu^{3+} (HA:Eu) and BGO nanoparticles were synthesized using the sol–gel technique and subsequent annealing. Their crystal structure was analyzed by X-ray diffraction and morphology by transmission electron microscopy. Their luminescence properties were tested in body fluids at different pH values. Oxidative stress induced by BGO was estimated in different tissues of zebrafish. Finally, both types of nanoparticles were functionalized with W6/32 antibody against leukemia human tumor cells, and their capacity to attach to neoplastic cells was studied using the THP-1 cell line.

HA:Eu nanoparticles under λ= 394 nm excitation yielded typical luminescence bands centered at 575 nm ($^5D_0 \rightarrow {}^7F_0$), ~590 nm ($^5D_0 \rightarrow {}^7F_1$), 613 nm ($^5D_0 \rightarrow {}^7F_2$) and 626 nm ($^5D_0 \rightarrow {}^7F_2$). HA:Eu dispersed in urine and blood serum also showed excellent optical properties.

On the other hand, BGO nanoparticles showed luminescence in organic fluids at different pH conditions, and the BSA functionalized nanoparticles preserved their optical properties when they were irradiated for 1.3 s with X-rays (53 keV) with a current of 255 mA. Additionally, BGO presented lower oxidative stress in different tissues of zebrafish at concentration of 0.5 ppm.

The capacity to be functionalized with W6/32 antibody and their specificity to identify THP-1 cells, indicate that BGO and HA:Eu nanoparticles are promising candidates for biomedical applications as synthetic biomarkers.

Keywords: HA:Eu, BGO, nanoparticle, PL, stability, oxidative stress, functionalization, biomarker

Resumen de la tesis de Mariana Jeannete Oviedo Bandera, presentada como requisito parcial para la obtención del grado de Doctor en Ciencias en Física de Materiales. Ensenada, Baja California. Octubre 2012.

Nanomateriales luminiscentes para aplicaciones biomédicas

Resumen aprobado por:

_____

Dr. Gustavo Alonso Hirata Flores
Director de Tesis

La hidroxiapatita sintética ($Ca_{10}(PO_4)_6(OH)_2$, HA) posee una excelente biocompatibilidad por lo que ha sido propuesta para diversas aplicaciones biomédicas. Por otro lado, el gemanato de bismuto ($Bi_4Ge_3O_{12}$, BGO) se emplea comúnmente como detector de altas energías en la industria y en medicina. Sin embargo, tras una exhaustiva búsqueda y revisión bibliográfica, este es el primer trabajo en el que se estudian las aplicaciones biomédicas de nanopartículas (NP) de BGO. Este trabajo se enfoca en la producción de NP de HA impurificada con europio (HA:Eu) y de BGO, con bajo nivel de toxicidad, propiedades luminiscentes estables en diferentes fluidos corporales y con capacidad de identificar células tumorales.

Se sintetizaron NP de HA:Eu y BGO por el método sol-gel y posteriormente fueron calcinadas. Su estructura cristalina se identificó por difracción de rayos-X, y su morfología por microscopia electrónica de transmisión. Sus propiedades luminiscentes se estudiaron en fluidos corporales a diferentes valores de pH. El estrés oxidativo inducido por el BGO se estimó en diversos tejidos de pez cebra. Finalmente, ambas NP fueron funcionalizadas con anticuerpos W6/32 y se exploró su capacidad de reconocer células tumorales de leucemia (línea celular THP-1).

Al excitar las NP de HA:Eu con λ= 394 nm se detectaron las bandas centradas en 575 nm ($^5D_0 \rightarrow {}^7F_0$), ~590 nm ($^5D_0 \rightarrow {}^7F_1$), 613 nm ($^5D_0 \rightarrow {}^7F_2$) y 626 nm ($^5D_0 \rightarrow {}^7F_2$). La HA:Eu dispersa en orina y suero mostró propiedades ópticas.

Por otro lado, las NP de BGO mostraron luminiscencia en fluidos orgánicos a diferentes condiciones de pH, y la funcionalización de las NP con BSA preservaron sus propiedades ópticas al ser irradiadas por un tiempo de 1.3 s con rayos-X (53 keV) con una corriente de 255 mA. Adicionalmente, el BGO presentó menor estrés oxidativo que el H_2O_2 y los nanotubos de carbono en los diferentes tejidos de pez cebra a una concentración de 0.5 ppm.

La capacidad de ser funcionalizadas con anticuerpos y su especificidad para identificar las células, indican que las nanopartículas de BGO y HA:Eu pueden ser excelentes candidatos para aplicaciones biomédicas como biomarcadores sintéticos.

Palabras clave: HA:Eu, BGO, NP, PL, estrés oxidativo, funcionalización, biomarcador

TO

MY PARENTS AND GRANMA,

Sabina Bandera, Luis Eduardo Oviedo & Celia Carranza

ACKNOWLEDGEMENTS

I would like to begin by thanking God for the special energy and love that he gives me to push myself.

I am indebted to my advisors Professors Gustavo Hirata, Oscar Edel Contreras, and Joanna McKittrick for their expert advice and guidance and their continuous support. I am also thankful to my committee members, Professors Rafael Vázquez Duhalt, Felipe Castillón and Alexei Licea for their important recommendations and their enthusiasm in this work. I am especially grateful to Professors Ivonne Rosenstein and María Teresa Viana for providing me a space at their laboratories to develop the biomedical applications presented in this study.

I would sincerely like to thank my teacher and friend Maria Isabel Perez-Montfort for English guidance and revision of this thesis and of the articles it has generated.

I gratefully acknowledge the technical support provided by E. Aparicio, F. Ruiz, I. Gradilla, J.A. Peralta, M. Vega, E. Flores, and D. Dominguez. I also thank the financial support from CONACYT (Grant No. 100555 and 82984) and DGAPA UNAM (Grant IN-114010 and IN-109612).

Financial support was granted for this work by the Consejo Nacional de Ciencia y Tecnología (CONACYT) (#165782). The Centro de Nanociencias y Nanotecnología, UNAM and Centro de Investigación Científica y de Educación Superior de Ensenada (CICESE) are also gratefully acknowledged. This study was partially supported by the U.S. Department of Energy, Grant DE-EE002003. I also thank the Brazilian Synchrotron Light Laboratory (LNLS), proposal D04B-XAFS1-9349.

I would like to say a special thank you to my family: Sabina Bandera, Eduardo Oviedo, Celia Carranza, Luis Oviedo, Edgar Oviedo, Airam Oviedo, Mitzi Oviedo, Milka Oviedo, Junior Oviedo and Tristan Oviedo for their infinite love and guidance.

My adorable and special friends, the “Mueganitos”: Oscar Jaime, Noemí Abundiz, Aldo Guerrero, Miguel Angel Estrada, César Meza, Carlos Belman, Duilio Valdespino, Juan Jesús Velarde and Marichuy Martínez, I am also grateful to them for all the meaningful moments that we spent together. Thanks to my best friend Laura Arroyo for having been with me all this time.

To my special friend Tito Quiroz as a birthday present. I promised to give you something that I had done with my own hands and brain, and that it would last forever.

I am especially grateful to all the teachers who taught me along my undergraduate, master and PhD student time.

To the great people whom I’ve met along this amazing and incredible time: Gregorio Carbajal, Sergio Castro (my first undergraduate student), Fernanda Samaniego, Victor Mendoza, Richard Williams, Leonardo de la Rosa, Brenda Anda, Francisco Castro, Fátima Pérez, Roberto San Juan, Patricia Nazario, Jair Manjarrez, Gilberto Moreno (*post mortem*) and the list continues.

I am grateful to Mariscos “La Guerrerense” for unconditional support and for giving me work and food every day.

Thanks to Physics, Life and God.

TABLE OF CONTENTS

TABLE OF CONTENTS (Cont.)

TABLE OF CONTENTS (Cont.)

TABLE OF CONTENTS (Cont.)

LIST OF FIGURES

LIST OF FIGURES (Cont.)

LIST OF FIGURES (Cont.)

LIST OF FIGURES (Cont.)

LIST OF FIGURES (Cont.)

LIST OF FIGURES (Cont.)

LIST OF FIGURES (Cont.)

LIST OF TABLES

Chapter I

Introduction

Materials science and engineering involves the characterization of the physical and chemical properties of solid materials such as metals, ceramics, magnetic materials, polymers, optical materials, semiconductors, superconductors, and composites. Its main purpose is to modify, change, or enhance the inherent properties of materials with the aim of creating new products. These have found applications in the areas of physics, chemistry, biotechnology, medicine and many others (Jandeleit, 1999). For example, inorganic nanoparticles are particularly attractive building blocks for the generation of larger superstructures, for example, nanomotors, electronic devices that use DNA as scaffold, and others (Schmid, 1994; Remacle *et.al.,* 2001). Such nanoparticles can readily be prepared in large quantities from various precursor materials by relatively simple methods, controlling the dimensions of the nanoparticles from one up to several hundred nanometers with a fairly narrow size distribution. Most often, the particles are comprised of metals, metal oxides, and semiconductor materials, such as Ag_2S, CdS, CdSe, and TiO_2 .

Nanoparticles have characteristic optical, electronic, and catalytic properties, which are very different from those of the corresponding bulk materials and often depend strongly on particle size in a highly predictable way. Some examples involving semiconductor nanocrystals include the specific wavelength and the intensity of the emitted light, which differ from the bulk material. These nanocrystals are used for biolabelling (Bruchez *et.al.,* 1998; Chan *et.al.,* 1998), or in lasers (Grundmann, 1995). Another example is the external magnetic field

required to switch a magnetized particle, which is highly relevant in hard disk drives (Dunin-Borkowski, 1998; Sun *et*.al., 2000). Additionally, certain types of nanoparticles can be considered as artificial atoms (Eychmüller, 2000) since they are obtainable as highly perfect nanocrystals, which can be used as building blocks for the assembly of larger two- and three-dimensional structures such as nanocrystal aggregates of TiO_2 and iron oxyhydroxide minerals (Alivisatos, 2000).

Materials science and engineering combined with biotechnology have provided solutions to medical problems, for example, by the novel use of drug delivery systems and *in vivo* imaging. Materials with nanoscopic dimensions (2-100 nm) such as nanoparticles, nanowires, and quantum dots have potential technological applications in areas such as device technology and medicine (Martin, 1994). Currently, however, a gap exists in the engineering of small-scale devices. While conventional top-down processes hardly allow the production of structures smaller than about 100-200 nm, the limits of regular bottom-up processes are in the range of about 2-5 nm (Niemeyer, 2001). Commercial requirements to produce increasingly miniaturized microelectronic devices strongly motivate the elaboration of nanoscale systems. The structural dimensions of computer microprocessors are currently in the range of about 100 nm. They have only recently become accessible by conventional top-down processes (miniaturization processes) such as photolithography. But for the foreseeable future, the large-scale production by photolithography of parts that are significantly smaller than 100 nanometers is limited.

There is plenty of room at the bottom, as Nobel physicist Richard Feynman pointed out more than 50 years ago (Feynman, 1961), and thus today's nanotechnology research places great emphasis on the development of bottom-up strategies (enlargement strategies), which involve the self-assembly of molecular and colloidal building blocks to create larger, functional components (Whitesides et. al., 1991). These nanotechnologically produced biological components will allow us to generate new smart materials, and together with other advanced materials

this will contribute to the solution of medical and technological problems. For these applications, biotechnology and materials science are currently interested in developing structures, focusing their attention on the same scale (Figure 1) (Niemeyer, 2001).

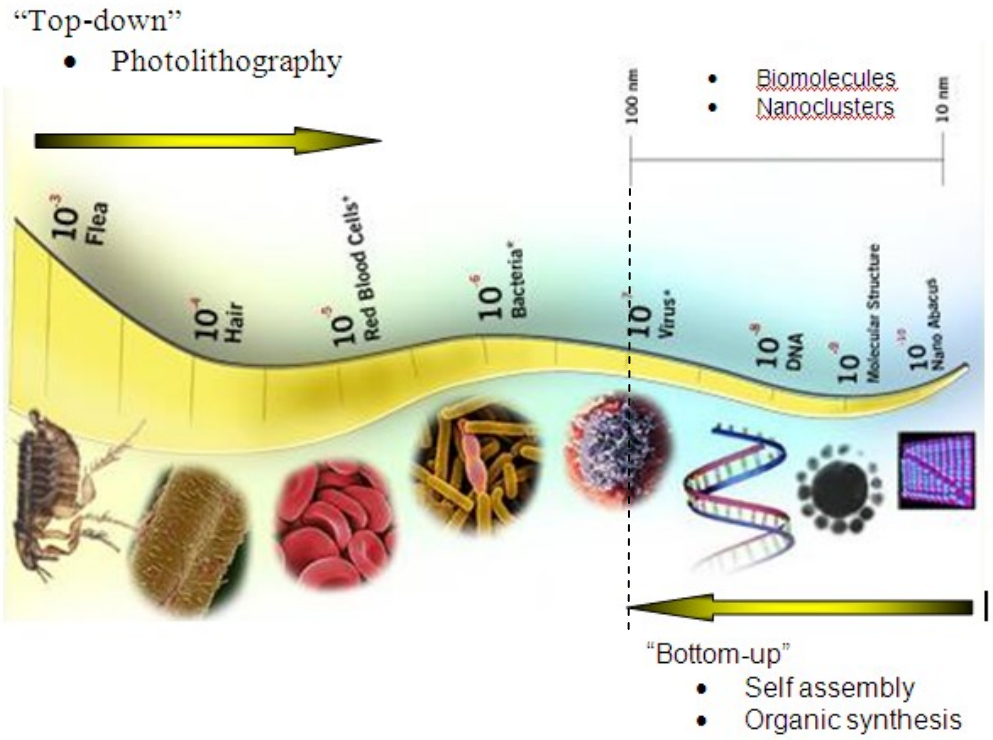

Figure 1 . *Biomolecules have typical size dimensions in the range of about 5 to 200 nm.*

Biomaterial developments are at the forefront of the biotechnological revolution and include materials for the components of artificial joints, heart valves, and other body part replacements. A biomaterial can be defined as a substance (other than a drug) or a combination of substances of either synthetic or natural origin, used for any period of time as a whole or as a part of a system, which treats, replaces or substitutes a tissue, an organ or a function of the body (Von Recum, 1995; Ratner *et.al.,* 1996). Biomaterials have potential applications in the dental and medical fields; for example, shape-memory alloys have been produced that

correct misplaced teeth or spine curvature, compressible stents that return to their intended shape upon contact with body heat once inserted into an artery, and, of importance to this study, hydroxyapatite, which has been used for bone repair (Ratner *et.al.,* 1996; Leukers *et.al.,* 2005; Gervaso *et.al.* 2011).

At present, biomaterials have important applications in medicine. An emblematic example is its present day use in cancer treatments. The evolution of cancer diagnosis and treatments began with invasive surgery, followed by new techniques in cancer diagnosis that entered the field in the 1970s, such as ultrasound (sonography), computed tomography (CT scans), magnetic resonance imaging (MRI scans), and positron emission tomography (PET scans), which have since replaced most exploratory operations. Today, CT scans and ultrasound are now used to guide biopsy needles into tumors; physicians can use fiber-optic technology and miniature video cameras to look inside the body, and surgeries are performed by special surgical tools which are introduced through narrow tubes placed into small incisions. This latter technique is called endoscopic surgery, and is used to remove tumors from the colon, esophagus, or bladder. Similar instruments are used to look and work inside the abdomen (laparoscopic surgery) or chest (thorascopic surgery). In short, cancer diagnosis and treatment has placed special emphasis in evolving towards less invasive ways of tumor localization and destruction.

There is a wide array of methods to diagnose cancer. For example, biomaterials such as polypyrrole has been used as intrinsically colored labels in immunoassays; colloidal silica combined with polypyrrole have also been shown to function well in immunoassays of cancer diagnosis (Pope *et.al.*, 1996). Diagnostic tools such as CT and PET scans are used non-invasively (non-surgically) to look inside the body. CT uses an X-ray tube combined with a computer to create a detailed picture of the body's tissues and structure, using a contrast material which is administrated to the patient prior to the scan. PET scans measure emissions from positron-emitting molecules such as carbon, nitrogen and oxygen. This is the

main difference between the CT and PET. PET shows molecular function and activity, not structure, and can therefore often differentiate between normal and abnormal (cancerous tumor) or live versus dead tissue. PET can also produce three-dimensional images, and is usually used to complement rather than to replace the information obtained from CT.

In recent times, scintillator materials have also acquired importance in diagnosis tools. A scintillator is a luminescent material that converts high energy incident radiation into emission of light with very short decay time (<< μs). Some luminescent materials have scintillator properties and are used in the biomedical industry as detectors of high-energy gamma photons and positron annihilation radiation (Macedo *et al.*, 2004; Nick 2006; Person *et al.*, 2011). The major application of scintillators such as bismuth germanate single crystals has been in the medical imaging field as detectors in positron emission tomography (PET) equipment (Valais *et al.*, 2008). New biomaterials and scintillator materials are currently being tested for medical diagnosis and for tool diagnosis, respectively. Biomaterials for diagnosis are ever less invasive due to their dimensions and biocompability. A biocompatible material has been defined as a material that does not induce an acute or chronic inflammatory response and does not hinder the proper differentiation of implant-surrounding tissues (Williams, 1987)

Highly sensitive and biocompatible methods are urgently needed for disease diagnosis to detect markers (antigens) present during early stages of disease in corporal fluids such as blood serum, cerebrospinal fluid and/or urine. A proposal to identify the markers is by attaching biological molecules which can also detect antigens (Figure 2) to inorganic luminescent material surfaces, and use them as synthetic biomarkers.

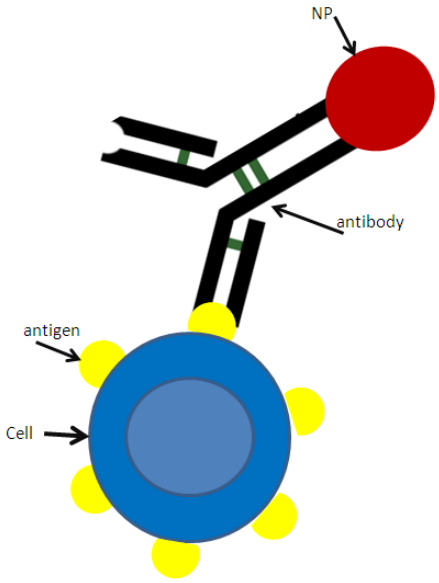

Figure 2. *A new approach to treat cancer is the use of nanoparticles to which antibodies have been attached to recognize specific neoplastic cells antigens.*

The luminescent activation of biomarkers can provide signs that enable earlier diagnosis or discern the presence of certain compounds at a primitive stage of the disease. Among biomarkers, luminescent materials have been investigated. Some synthetic materials have been applied in biomedicine and biotechnology as biomarkers. Examples are, nanocrystalline silicon, which has been used as a biomarker and is biocompatible, however, when inside a biological tissue its luminescence properties decrease considerably (Park *et al*, 2009); quantum dots (QD) for *in-vivo* imaging, which have a wide range of optical properties not present in organic fluorophores such as rhodamine 6G and fluorescein (Alivasatos *et.al.* 2005). QD also display brighter emission and higher signal noise ratio compared with organic dyes. They are 10-20 times brighter and can identify specific cells when these have been functionalized with antibodies (Gao *et. al.*, 2005).

Biomarkers have also been developed which identify information of disease in body fluids. Blood, urine, and cerebrospinal fluid are convenient for diagnosis because they can be easily obtained and they contain significant biological

information such as antibodies, antigens or changing pH. Biomarkers are used to detect a biological factor that can reveal either a stage of the disorder, or a surrogate manifestation of the disease (Mayeux, 2004).

The goal of the present research was to investigate the synthesis and properties of two inorganic materials, europium-activated hydroxyapatite and bismuth germanate, and explore their possible use as biomarkers. Additionally, bismuth germanate nanoparticles were tested as scintillators. When hydroxyapatite is activated with rare earths such as europium or dysprosium, the obtained compound acquires luminescent properties. Activated hydroxyapatite has been recently applied to diagnosis and/or disease treatment with successful results (Rauschmann *et al.*, 2005; Wang *et al.*, 2006; De Araujo *et al.*, 2007; Yang *et al.*, 2008). The compound has several advantages: a) specific light emission spectra due to the electronic transitions, b) long lifetime, c) excellent photostability, d) chemical stability, e) biocompatibility, f) nanoparticles size smaller than 100 nm, and h) excitation wavelength >300nm.

In the first part of the thesis, europium activated hydroxyapatite nanoparticles (HA:Eu) were synthesized by the sol-gel technique and subsequently annealed. Then, the nanoparticles were characterized and their optical properties studied by photoluminescence spectroscopy (PL) in different body fluids such as urine and blood serum at different pH conditions. Thereafter, the HA:Eu nanoparticles were functionalized with antibodies and tested on human cancer cells.

On the other hand, BGO crystals have been the focus of several studies due to their scintillation properties. BGO is generally used in the single crystal form and, because of the difficulty of producing these single crystals alternative powders ceramics are been investigated. BGO single crystals are usually obtained by the Czochralski technique; while the powders are traditionally synthesized by the Pechini route or solid-state reaction (de Jesus *et. al.*, 2010; Weber and Monchamp, 1973). However, the scintillator properties of BGO nanoparticles smaller than 100 nm in diameter have not been explored yet.

In the second part of this thesis, I synthesized and characterized bismuth germanate (BGO) nanoparticles and investigated the possibility of using BGO as synthetic biomarker. We studied the optical and structural properties of BGO nanoparticles produced by the sol-gel method and post-annealed by a slow thermal treatment. The interaction of BGO with corporal fluids such as human urine, blood serum and proteins was then explored. Finally, the BGO nanoparticles were functionalized with antibodies and tested in human cancer cells. To the best of our knowledge, this is the first work that studies the properties of BGO as a synthetic biomarker.

In summary, this work was mainly focused on the production of europium-activated hydroxyapatite and bismuth germanate nanoparticles with low potential toxicity, stable luminescence properties in body fluids. Their capacity to be functionalized and identify human tumor cells was also explored.

Research hypothesis

The luminescent properties of europium-activated hydroxyapatite and bismuth germanate nanoparticles are stable in body fluids, and they can therefore be used as biomarkers. When appropriately functionalized, these nanoparticles can identify human tumor cells.

General objectives:

1. Synthesis and characterization of europium-activated hydroxyapatite and bismuth germanate nanoparticles.
2. Analysis of nanoparticle photoluminescence stability in body fluids.
3. Development of a new method to functionalize the nanoparticle surface with antibodies for the identification of human tumor cells.
4. Identification of human tumor cells with the functionalized nanoparticles.

Specific Objectives:

1. Synthesis of europium-activated hydroxyapatite and bismuth germanate nanoparticles by the sol-gel method.
2. Characterization of both types of nanoparticles by X-ray diffraction (XRD), transmission electron microscopy (TEM), photoluminescence (PL), and bismuth germanate by radioluminescence (RL) and scintillating decay time.
3. Photoluminescence analysis of both types of nanoparticles in different body fluids.
4. Functionalization of both types of nanoparticles with antibodies against human tumor cells.
5. Experimental study of human tumor cell recognition by functionalized nanoparticles.

Chapter II

Background

The properties and applications of hydroxyapatite and bismuth germanate are described in this chapter. It then includes an explanation of the concept of bionanotechnology, a description of nanomaterials that can be applied in nanomedicine, and, finally, an account of the use of nanomaterials for cancer diagnosis and treatment.

II.1 Physical concepts

II.1.1 Luminescent Materials

A luminescent material (phosphor) emits visible electromagnetic radiation when exposed to external energy excitation (Blasse, 1994). Luminescence can be excited by many types of energy. For example, photoluminescence is excited by electromagnetic radiation (e.g. ultraviolet), cathodoluminiscence by a beam of energetic electrons, electroluminescence by an electric voltage, X-ray luminescence by X-rays, and so on (Blasse, 1994; Gfroerer, 2000). Figure 3 shows a diagram representing a crystal or a grain (host lattice) of a luminescent material. The system consists of a host lattice and a luminescent center (activator, A).

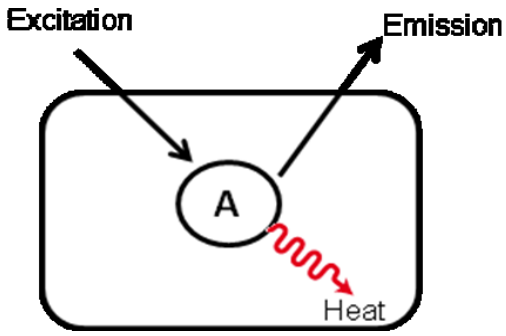

Figure 3. *Luminescent ion A inside a host lattice. Excitation, emission (radiative process) and heat (non-radiative return to the ground state).*

The luminescence processes in such a system are as follows: the exciting radiation is absorbed by the activator raising it to an excited state (A*) (Figure 4). The excited state returns to the ground state (A) by emission of radiation. This would seem to suggest that every ion and every material should show luminescence, which is not true. The reason for this is that luminescence has radiative and nonradiative processes. In the nonradiative process, when the energy of the excited state returns to the ground state, the energy is dissipated as vibrations of the host lattice, *i.e.* phonons (Blasse, 1994).

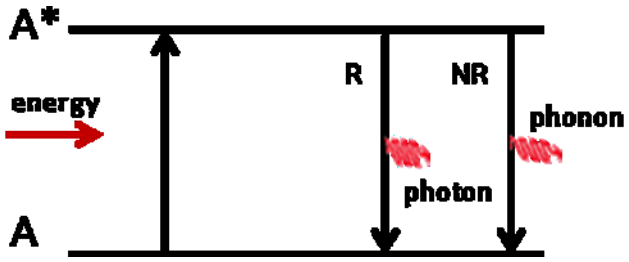

***Figure 4**. Energy level scheme of the luminescent ion A. A* is the excited state, R the radiative return and NR the nonradiative return to the ground state.*

Figure 5 shows the configurational coordinate diagram where *E* is plotted versus *R* explaining the luminescence processes in a luminescent center. The configurational diagram shows the potential energy curves of the absorbing center as a function of a configurational coordinate. Consider the first curve for the lowest state, the ground state. Its shape is parabolic with a minimum at R_0. This parabolic shape follows from the fact that the vibrational motion is assumed to be harmonic, the restoring force *F* is proportional to the displacement*:* $F=-k(R-R_0)$. A force of this form corresponds to a potential energy whose dependence on *R* is parabolic: $E=K/2(R-R_0)^2$. The minimum R_0 of the parabola corresponds to the equilibrium distance in the ground state. The quantum mechanical solution of this problem yields, for the energy levels of the oscillator, $E_v=(v+1/2)h\nu$, where $v=0, 1, 2,\ldots$ and ν is the oscillator frequency. Some of these levels have been drawn in Figure 5. In optical absorption the luminescent center is promoted from its ground state to an excited state. The luminescent center first returns to the lowest vibrational level of the excited state ($v=0'$), and gives up the excess energy to the surroundings; this process is called relaxation (Blasse, 1994). During relaxation, no emission usually occurs, and certainly not of high intensity. From the lowest vibrational level of the excited state the system can return to the ground state spontaneously accompanied by emission of radiation. For emission, the luminescent center reaches a high vibrational level of the ground state. Again relaxation occurs, but now to the lowest vibrational level of the ground state. The emission has a lower energy than the absorption due to the relaxation processes.

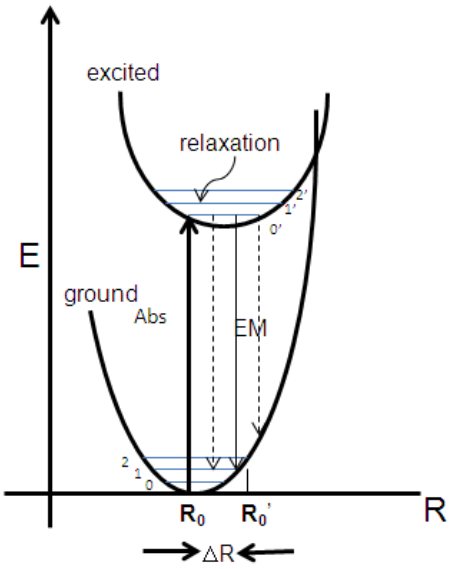

Figure 5. The absorption transition ground→excited state. After absorption the system reaches high vibrational levels of the excited state. Subsequently, it relaxes to the lowest vibrational level 0' from where emission excited→ground occurs in a broad band.

II.1.2 Rare earth (RE) ions

The rare-earth ions (named RE due to the difficulty of finding them in nature) are most commonly used for applications as phosphors, lasers, and amplifiers. Rare earths are located in the periodic table after lanthanum: from the cerium atom (atomic number 58), which has an outer electronic configuration $5s^2\ 5p^6\ 5d^1\ 4f^1\ 6s^2$, to the ytterbium atom (atomic number 70), with an outer electronic configuration $5s^2\ 5p^6\ 4f^{14}\ 6s^2$. These atoms are usually incorporated in crystals as divalent or trivalent cations. In trivalent ions, 5d, 6s, and some 4f electrons are removed and so $(RE)^{3+}$ ions deal with transitions between electronic energy sublevels of the $4f^n$ electronic configuration. Divalent lanthanide ions contain one more f electron (for instance, the Eu^{2+} ion has the same electronic configuration as the Gd^{3+} ion, the next element in the periodic table) but, differing from trivalent ions, they show f→d interconfigurational optical transitions (Solé *et.al.,* 2005).

Figure 6 shows a substantial part of the energy levels originating from the $4f^n$ configuration as a function of n for the trivalent ions. The width of the bars represents the order of magnitude of the crystal field splitting (Blasse, 1994).

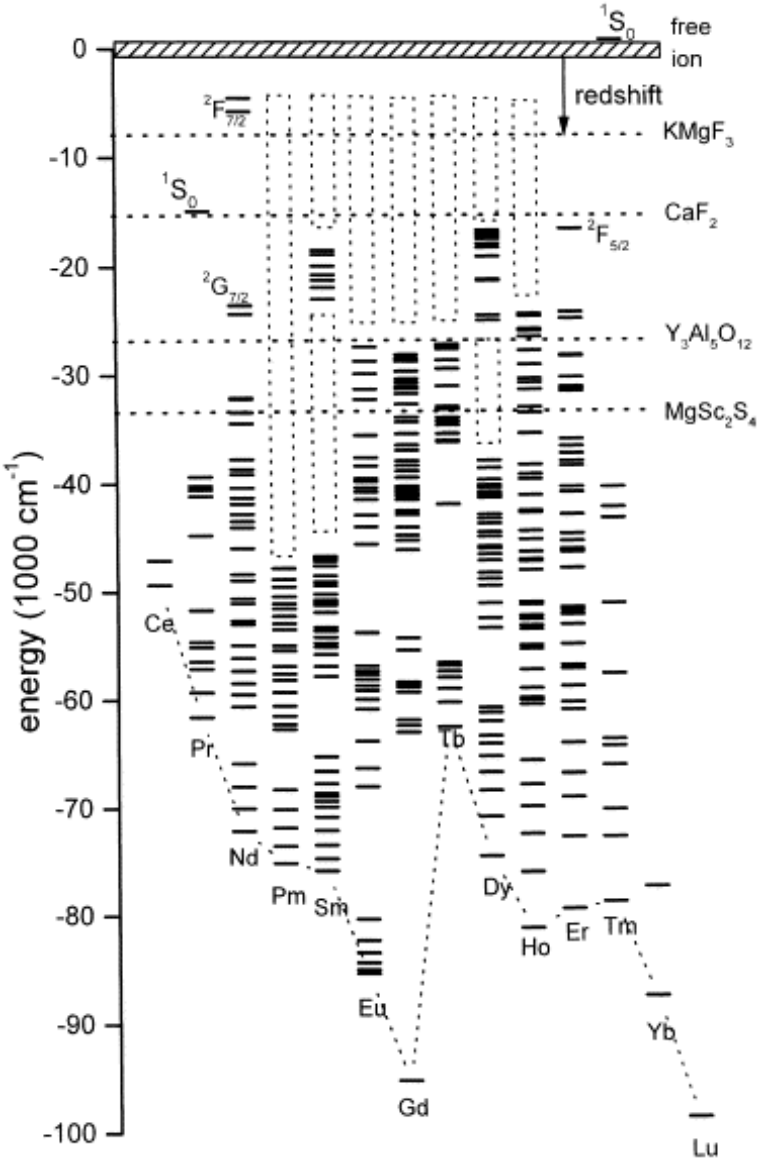

Figure 6. *Level diagram of 4f*n *states in the trivalent lanthanides 4F*^{n} *energy levels. (Dorenbos, 2002, p. 157)*

The emission peaks of the europium ion (Eu^{3+}), for example, usually fall in the red spectral area. These emissions have found important applications in

lighting and display technologies. They correspond to the optical absorption transitions of Eu^{3+} from the excited $^5D_0$ level to the ^7F_j (j=0, 1, 2, 3, 4, 5, 6) levels of the $4f^6$ configuration.

II.1.3. Ions with s^2 configuration

Ions with s^2 configuration show strong optical absorption in the ultraviolet due to a $s^2 \rightarrow sp$ transition. The s^2 configuration gives one level for the ground state $^1S_0$. The subscript indicates the value of *J*, the total angular momentum of the ion. The sp configuration yields, in sequence of increasing energy, the $^3P_0$, $^3P_1$, $^3P_2$, and $^1P_1$ levels. The optical absorption transitions observed are $^1S_0 \rightarrow {}^1P_1$ and $^1S_0 \rightarrow {}^3P_1$. Luminescent ions with this configuration are Tl^+, Pb^{2+}, Bi^{3+}.

II.1.4 Scintillators

A scintillator is a luminescent material that converts high-energy incident radiation into visible light with very short decay time (<< μs). The main application of scintillators has been in the medical imaging field as detectors of high-energy gamma photons and positron annihilation radiation in positron emission tomography (PET) equipment (Macedo *et al.*, 2004; Nick 2006; Person *et al.*, 2011;Valais *et al.*, 2008).

Wide band-gap materials are employed for transformation of X-rays to ultraviolet/visible photons. Scintillation conversion is a relatively complicated issue, which can be divided into three consecutive sub-processes: 1) conversion, 2) transport, and 3) luminescence (as shown in Figure 7).

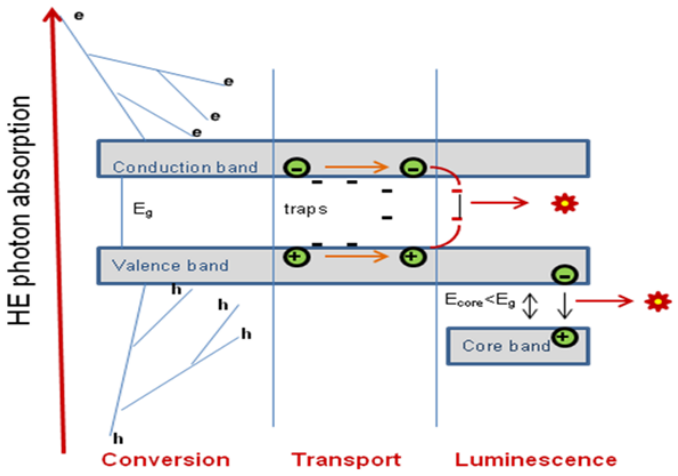

Figure 7. *Scintillator conversion mechanism in a wide band-gap single crystal (from Nikl, 2006, p. R38), where e are electrons and h are holes.*

During conversion, a multi-step interaction of a high-energy (here considered ~ 1MeV) photon with the lattice of the scintillator material occurs through the photoelectric effect and the Compton scattering effect. Many electron-hole pairs are created and thermalized in the conduction and valence bands, respectively. In the transport process, electrons and holes, which eventually create excitons, migrate through the material. In terms of energy states, the exciton corresponds to elevation of the electron to a state higher than the valence but lower than the conduction band (Tsoulfanidis, 1995). Considerable delay in migration can be introduced owing to the mentioned charge carrier recapture at trapping levels in the forbidden gap of the material. This stage is the least predictable, as material point defects, flaws, surfaces and interfaces can introduce energy levels into the forbidden gap and strongly modify/degrade otherwise intense intrinsic scintillation behavior. Apparently, these physical phenomena are strongly synthesis-technique dependent (Shepherd *et al.*, 1997). The final stage, luminescence, consists in consecutive trapping of the electron and hole at the luminescence center, their recombination and emission of photons (radiation). In a particular group of materials, light generation occurs in radiative transitions between the valence and first core bands as sketched in Figure 9; these are so-

called cross luminescence scintillators (Rodnyi, 1997). The luminescence in BGO is a result of the trivalent bismuth (Bi^{3+}) cations in inorganic hosts, and exhibits interesting luminescence properties originating from the excitation and relaxation of its $6s^2$ electronic level (Blasse, 1968; Weber and Monchamp, 1973).

II.2 Hydroxyapatite (HA)

Calcium phosphates are compounds of great interest in interdisciplinary fields of sciences involving materials, chemistry, biology, medicine and geology. Hydroxyapatite ($Ca_{10}(PO_4)_6(OH)_2$, HA), is the most stable calcium phosphate salt at normal temperatures and pH between 4 and 12. It is a compound of great interest in catalysis, the fertilizer and pharmaceutical products industries, in protein chromatography applications, water treatment processes, preparation of biocompatible materials mostly because it is the main inorganic component in calcified hard tissues (e.g., bone and teeth) of vertebrates HA is also formed pathologically as a result of functional irregularities resulting in cartilage arthritis, formation of renal, bladder, and bile stones, atheromatic plaque, and calcification of transplanted cardiac valves (Hamlekhan *et al.*, 2010; Joris *et.al.,* 1971; Kibby and Hall, 1972; Uchida *et.al.,* 1992; Kawasaki, 1991; Christofferse *et.al.,* 1991; Walsh and Guzelsu, 1994; Khan, 1995; Nancollas, 1977; Cohen *et.al.,* 1987; Schmid *et.al., 1980;* Koutsopoulos *et.al.,* 1998). In the research, HA is considered as a model compound to study biomineralization phenomena. For this reason, there is a strong interest in synthetic, well-defined HA nanoparticles for use in detailed physicochemical *in vitro* and *in vivo* studies, medical applications, and surgery (e.g., middle-ear implants, reconstructive bone replacement, *etc.*) (Drucker *et.al.,* 1991; Deeb *et.al.,* 1989; Jahn, 1992).

Several methods to prepare HA crystals have been reported including solid state reactions, plasma techniques, crystal growth under hydrothermal conditions, layer hydrolysis of other calcium phosphate salts, and sol-gel crystallization (Paschalis *et.al.,*1995; Fowler, 1974; Yamasaki *et.al.,* 1990; Nishioka *et.al.,* 1986).

Essentially, the synthesis of HA crystals from supersaturated aqueous solutions is advantageous due to its low cost and simplicity (lasic *et.al.,* 1996), but most of the procedures followed until now have led to the formation of nonstoichiometric products (Kandori *et.al.,* 1995; Heughebaert *et.al.,* 1990). Deviation from the stoichiometry of HA is due to the presence in the crystal lattice of vacancies and ion substitutes such as carbonates, hydrogen phosphates, potassium, sodium, nitrates, and chloride (Heughebaert *et.al.,* 1990; Zawacki *et.al.,* 1990; Hlady *et.al.,* 1979; Nelson *et.al., 1989)*. Contamination of HA with these ions or formation of deficient hydroxyapatites are the result of significant changes in their crystallographic characteristics and have different crystal morphology as compared to the stoichiometric product (Nelson *et.al., 1989)*.

II.2.1 Physical and chemical properties of HA

Hydroxyapatite is the calcium phosphate compound most commonly used as a biomaterial because of its perfect biocompatibility and its bioactivity in the human body (Mavropoulos *et al.*, 2011). It is compatible with various tissue types and can adhere directly to osseous, soft, and muscular tissue without an intermediate layer of modified tissue (Denissen *et.al.,* 1980; Black, 1999). It also displays osteoconductivity, a property of a material that encourages bone already being formed to lie closely to, or adhere to its surface (Black, 1999). This is used in bone implants where fast healing is required. Despite its excellent properties as a biomaterial, the inherent mechanical properties of HA, specifically its brittleness, poor tensile strength, and poor impact resistance have restricted its application in many load-bearing situations (Jarcho, 1981). Therefore, the concept of applying HA onto metallic implants as a surface coating was developed, and the HA-coated implant combined the good strength and ductility of the metal with the excellent biocompatibility and bioactivity of the HA (Tsui *et.al.,* 1998; Berndt *et.al.,* 1990).

Hydroxyapatite crystallizes in a hexagonal structure $P6_3/m$ (JCPDS No. 9-432) with the following crystallographic parameters (Posner *et al.*, 1957): a= 9.418

Å, c= 6.881 Å and β= 120°. The HA crystallographic structure consists of a quasi-compact packing of phosphate groups, which form two types of tunnels parallel to axis C, in which the Ca^{2+} ions are located, Figure 8. An interesting property of the apatite structure is that it allows a large number of substitutions (Young, 1975; Legeros, 1980).

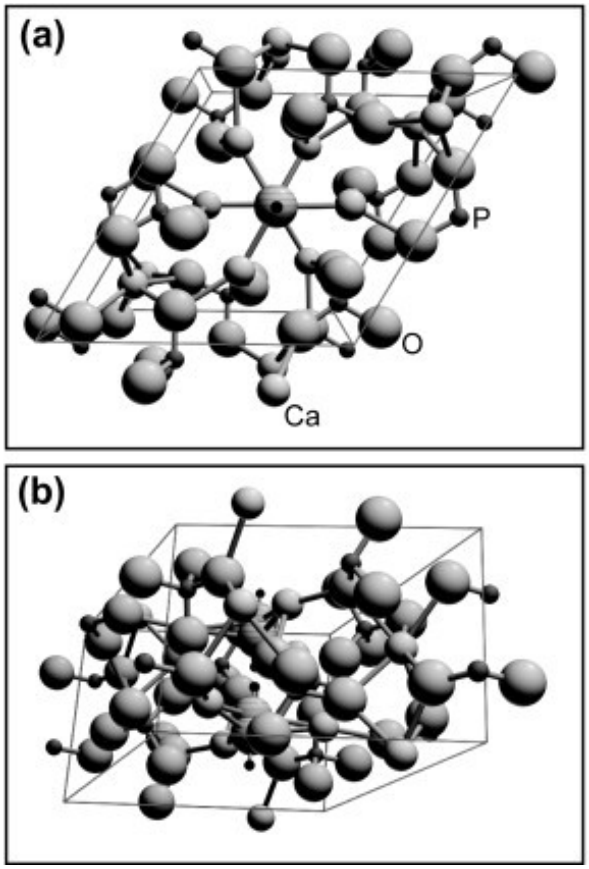

Figure 8*. Crystal structure of hydroxyapatite (a) along the c-axis and (b) off-axis. (Graeve et.al.,* 2010, p.4266)

Table I shows some physical parameters of HA. For example, the fracture toughness of HA does not exceed the value of 1 MPa-$m^{1/2}$ compared with the human bone: 2-12 MPa-$m^{1/2}$ (Hench and Ethridge, 1982). The Weibull modulus is related to the strength properties as well as with fracture toughness (Barbero *et.al., 2000).*

Table I. *Physical parameters of hydroxyapatite.*

Parameter	***Value***
Melting point	1200°C
Fracture toughness (K_{Ic})	1 MPa-$m^{1/2}$
Weibull modulus (n)	5-12

II.2.2 Hydroxyapatite synthesis

Natural forms of this material are available, but synthetic versions with specific morphologies, physical and chemical properties are more important in biomedical practice (Tadic *et al.*, 2004). Multiple techniques have been used to prepare synthetic HA powders such as precipitation, hydrothermal, hydrolysis and solid state reactions (Aoki, 1991; Townley, 1995; Balamurugan *et al.*, 2002; Lin *et al.*, 1998). Low-temperature techniques generally result in amorphous or lightly crystalline HA material, which must then be annealed in order to obtain crystallinity. Stoichiometry and hexagonal structure is not obtained (Lebugle *et al.*, 1986; Betts and posner, 1974). Crystallinity is obtained as a function of temperature (Mortier *et al.*, 1989; Monna *et al.*, 1981), as in the case of calcium-deficient hydroxyapatite, as illustrated by reaction (1). At higher temperatures (800 °C to melting point) the whitlockite phase ($Ca_3(PO_4)_2$, β-TCP) is always formed (Bohner 2000; Toriyama *et al.*, 1996; Lin *et al.*, 1998). Furthermore, the formation of agglomerates is evident as the temperature increases (Liu *et al.*, 2001; Murray *et al.*, 1995).

$$\begin{aligned} &Ca_{10-z}(HPO_4)_z(PO_4)_{6-z}(OH)_{2-z}nH_2O^{<250°C\,(I)} \rightarrow \\ &Ca_{10-z}(HPO_4)_z(PO_4)_{6-z}(OH)_{2-z}\cdot(H_2O)_z + (n-z)H_2O^{250-600°C\,(II)} \rightarrow \\ &Ca_{10-z}(HPO_4)_{2z}(PO_4)_{6-2z}(OH)_2^{350-720°C\,(III)} \rightarrow \\ &Ca_{10-z}(P_2O_7)_{z-s}(PO_4)_{6-2z+2s}(OH)_{2(1-s)} + (z+s)H_2O^{700-900°C\,(IV)} \rightarrow \\ &(1-z)Ca_{10}(PO_4)_6(OH)_2 + 3zCa_3(PO_4)_2 + (z-s)H_2O \end{aligned} \quad (1)$$

II.2.3 Luminescence activation of Eu^{3+} in HA

When hydroxyapatite is activated with certain rare-earth ions, the compound acquires luminescent properties (De Araujo *et al.*, 2007). Specifically, when HA is impurified with europium (HA:Eu), HA exhibits luminescence for the typical transitions associated with Eu^{3+} *i.e.* $^5D_0 \rightarrow {}^7F_1$, $^5D_0 \rightarrow {}^7F_2$, electron transitions under UV excitation. When HA:Eu is excited with a wavelength of 395 nm, the brighter emissions are found for the $^5D_0 \rightarrow {}^7F_1$ transition centered around 590 nm and for the $^5D_0 \rightarrow {}^7F_2$ transition at around 611 nm (Graeve *et.al.,* 2010; Doat *et.al.,* 2004). The labeling of the emission peaks corresponds to typical transitions attributed to Eu^{3+} as listed in Table II for some studies. Thus the emission peaks observed correspond to $^5D_0 \rightarrow {}^7F_0$ at 575 nm, $^5D_0 \rightarrow {}^7F_1$ at 605 nm, $^5D_0 \rightarrow {}^7F_2$ at 625 nm and 631 nm, and $^5D_0 \rightarrow {}^7F_3$ at 661 nm.

According to Martin *et al*. (1994) charge compensation for occupancy of Eu^{3+} into Ca^{2+} sites in apatites occurs by a substitution of OH^- with O^{2-} through the following reaction (2):

$$Eu^{3+} + O^{2-} \rightarrow Ca^{2+} + OH^- \rightarrow Ca_{10-x}Eu_x(PO_4)_6(OH)_{2-x}O_x \qquad (2)$$

From this reaction (equation 2) it may be concluded that the Eu^{3+} ion will occupy sites, which are closer to O^{2-} ions in apatite materials (Ternane *et al.*, 1999). The efficiency of this charge-compensation mechanism is high.

Table II. *Fluorescence transitions of* Eu^{3+} *in apatites.*

Electron transition	***Wavelength (nm)***	***Reference***
$^5D_0 \rightarrow {}^7F_0$	573, 578, 579 574, 577 573, 576, 578 575	Gaft *et al.*, 1997 Ternane *et al.*, 1998 El-Ouenzerfi *et al.*, 1999 Graeve *et al.*, 2010
$^5D_0 \rightarrow {}^7F_1$	590, 608 590, 591, 592, 595 583, 610 605	Gaft *et al.*, 1997 Zounani *et al.*, 1990 El-Ouenzerfi *et al.*, 1999 Graeve *et al.*, 2010
$^5D_0 \rightarrow {}^7F_2$	615, 616, 618, 627, 631 610, 613, 614, 616, 618 Approximately 600-620 625, 631	Gaft *et al.*, 1997 Zounani *et al.*, 1990 Lazoryak *et al.*, 1996 Graeve *et al.*, 2010
$^5D_0 \rightarrow {}^7F_3$	653 650, 653, 655 Approximately 640-660	Gaft *et al.*, 1997 Zounani *et al.*, 1990 Lazoryak *et al.*, 1996
$^5D_0 \rightarrow {}^7F_4$	700 689, 692, 694-5, 698, 699, 700-706 Approximately 680-710	Gaft *et al.*, 1997 Zounani *et al.*, 1990 Lazoryak *et al.*, 1996

II.3 Bismuth germanate (BGO)

Bismuth germanate $Bi_4Ge_3O_{12}$ (BGO) has cubic structure with a space group $I\bar{4}3d$ with a crystallographic parameter *a= 10.5187* Å and Bi^{3+} site coordinated by a distorted octahedron of oxygen ions, Figure 9. BGO has been used as a scintillator for the past forty years (Weber and Monchamp, 1973). Scintillators are materials that produce light when they are excited by ionizing radiation (X-rays, gamma rays). They are utilized as detectors in scientific research, industry and medicine (Chung and Chang, 2003; Macedo *et al.*, 2004), often in the single crystalline form. Because of the difficulties involved in producing good quality large samples, research has turned to polycrystalline ceramics that

can be used in place of single crystals (Greskovich and Duclo,1997). The advantages of using polycrystalline samples include more uniform doping and reduced costs for large samples, which can be produced in a variety of shapes and sizes that can broaden the scintillator's applicability (De Jesus *et al.*, 2010).

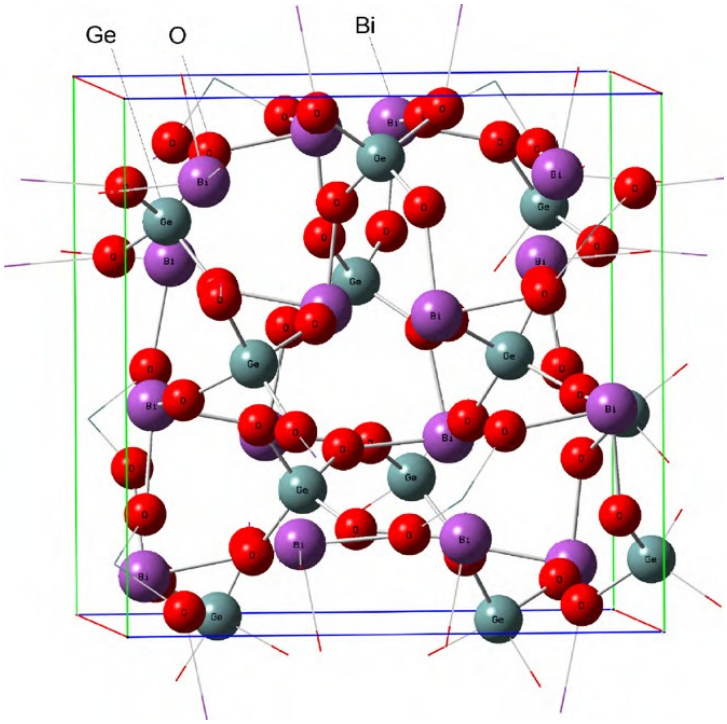

Figure 9. *BGO structure (ICSD 39227). (Polosan, 2010, p. 1494)*

Nanoparticles are a topic of extensive research for the development of new luminescent materials, which are essential components for emerging technologies in imaging, lighting and display devices. BGO powders have been synthesized by solid state reaction, combustion synthesis and by a polymeric precursor method (De Jesus *et al.*, 2009; Polosan 2010). Sol-gel among other chemical methods, are versatile techniques used to produce nanoparticles. Nevertheless, to the best of our knowledge, BGO nanocrystalline materials with particles size smaller than 500 nm in diameter and with good scintillator properties have not been obtained.

II.3.1 Physical and chemical properties of BGO

Some properties of bismuth germanate ($Bi_4Ge_3O_{12}$, BGO) are summarized in Table III. Due to its interesting scintillator properties, BGO is used in calorimeters and PET scanners. Because BGO has properties such as short decay time (300 ns), the afterglow is weak (0.005 ms) and the density is high (7.13 gr/cm^3); BGO is therefore used as detector oh high energy radiation.

***Table III**. Properties of $Bi_4Ge_3O_{12}$ single crystal.*

Property	***$Bi_4Ge_3O_{12}$***
Density (gr/cm^3)	7.13
Emission maximum (nm)	480
Light yield (photons/MeV)	9000
Decay time (ns)	300
Afterglow (% after 3 ms)	0.005
Melting point (°C)	1050
Radiation length (cm)	1.12
Stokes shift (cm^{-1})	17600
Bandgap	5.17 eV
Refractive index	2.15

BGO single crystals are used in the field of radiation detection due to the low number of defects which can negatively influence the scintillating parameters. Scintillation detectors consist of a phosphor material followed by an optional optical relay element and a photodetector. After X- or γ- ray photon absorption, the ultraviolet/visible light is converted into scintillation (flash of light produced in a material by an ionization), which is focused by the optical relay element onto the

photodetector, at the output of which an electrical signal is available for further processing (Nikl, 2006). However, the scintillation mechanism in BGO materials is based on intrinsic luminescence of Bi^{3+} ions owing to the $6s6p \rightarrow 6s^2$ transition under UV or X-ray radiation (Chapman *et al.*, 2008). This luminescence has a decay time of 300 ns, at room temperature (Van Rijk, 2002).

II.3.2 Synthesis of BGO

BGO single crystals are usually obtained by the Czochralski method. Their synthesis, however, entails high production costs, and presents some limitations mainly due to incongruent melting and different phase transitions resulting from the different partial pressure of the components. For example, when growing $Bi_4Ge_3O_{12}$ crystals from Bi_2O_3 and GeO_2, Bi_2O_3 has a lower melting point than GeO_2 (823°C *vs.* 1050°C); thus, 0.01 % mol excess of Bi_2O_3 is required (Polosan, 2010); Glass-ceramics or polycrystalline powders may be an alternative to single crystals for scintillator purposes because of their low cost and easy preparation either from a high temperature melt by fast cooling (Polosan *et al.*, 2005), by controlled crystallization of a fraction of glasses or, more recently, by the sol-gel technique (Chiodini *et al.*, 2002). Figure 10 shows the endothermic peaks at 880ºC and 1050ºC corresponding, respectively, to the eutectic point, in which the liquid phase coexists with the crystalline phases $Bi_4Ge_3O_{12}$ and $Bi_{12}GeO_{20}$, and to the melting point of $Bi_4Ge_3O_{12}$ (Macedo *et.al.,* 2004). The eutectic mixture consists of two or more phases with a lower melting point than $Bi_4Ge_3O_{12}$, and, in this temperature (Muldrey *et.al.,* 2006).

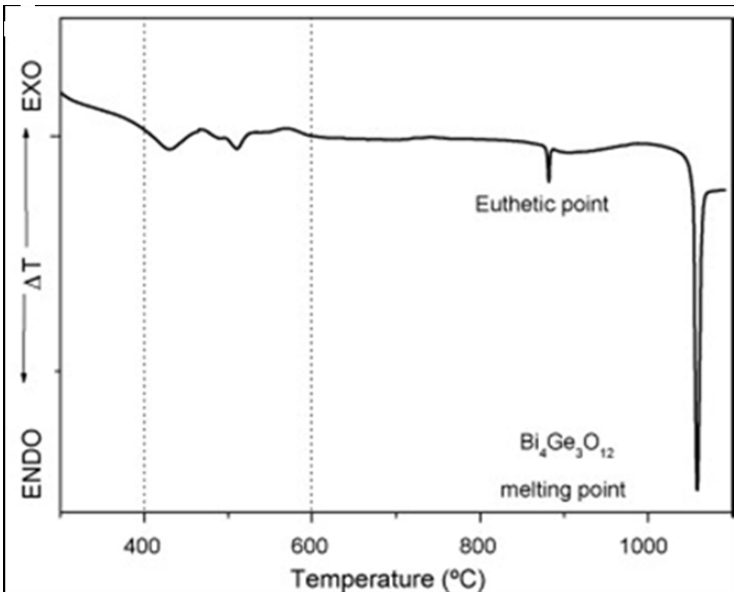

Figure 10. *Differential thermal analysis (DTA) of BGO. (De Jesus et.al., 2009, p. 127)*

To produce $Bi_4Ge_3O_{12}$, alternative methods such as combustion synthesis have been explored. This method in particular produced agglomerated microcrystalline material (de Jesus *et al.*, 2009). An interest challenge will be to synthesize nanoparticles of $Bi_4Ge_3O_{12}$ with scintillator applications.

In the following section I expose how nanomaterials such as hydroxyapatite and bismuth germanate can be applied in nanomedicine as targeting nanoparticles (synthethic biomarkers) for cancer diagnosis and treatment. The new developments in medicine and biology using nanotechnology are a novel fusion of these research areas, which has been labeled bionanotechnology.

II.4 Biomolecular concepts

II.4.1 Bionanotechnology

The recent developments of nanoscale materials in physical sciences and the advances in molecular biology, provide novel methodologies for applications in life sciences, electronics, and optics, among others. Bionanotechnology is the application of nanotechnology to biological fields or the fusion of nanotechnology with biotechnology. Nanotechnology can be defined as a novel scientific approach that involves new materials and techniques capable of manipulating physical and chemical properties at the nanoscale. On the other hand, biotechnology uses the knowledge and techniques of biology to manipulate molecular, genetic and cellular processes to develop products and devices, and is used is medicine, biology and agriculture among other fields (Kakruddin *et.al.,* 2012).

Bionanotechnology is focused on the development of new nanomaterials (<100 nm) for applications in diagnosis and therapy against degenerative diseases. Important limitations in nanomaterial production are mostly associated with the synthesis of nanoscale objects. In biological systems, highly organized biological materials are self-assembled into ordered structures of controlled size and organization and of two or three dimensional arrangements, depending on their function (Tamerler *et.al.,* 2009). This characteristic can be useful to synthesize specific nanomaterials using self-assembled organic molecules as scaffold, such as nanowires produced by molecular lithography.

The interaction between nanotechnology and biological systems can lead to the design of novel diagnosis and therapy tools. By nanotechnological techniques,

different materials can be fabricated with distinct properties such as optical, electrical or magnetic properties. These new materials can be functionalized with organic and biological molecules and then interact with biological systems with low risk of rejection by the system. For example, magnetic nanoparticles have been functionalized with herceptin antibody and used as a contrast agent for tumor imaging (Jun *et.al.,* 2005). The size of nanomaterials is similar to most biological molecules, therefore, nanomaterials can be useful for *in vivo* and *in vitro* biomedical research and applications.

Nanomaterials such as nanoparticles can be functionalized and effectively used to diagnose and deliver drugs. Drug-loading onto functionalized nanoparticles allows selective delivery of these drugs to specific sites within the organism. This can enhance drug efficacy at the diseased site and reduce drug toxicity for the whole organism (Figure 11) (Fakruddin, 2012; Mitchell *et. al.,* 1999; Taton *et.al.,* 2000). Visionaries in the field of bionanotechnology have predicted that one day, researchers will incorporate multifuncionality into nanomaterials. With these multifunctional nanodevices, molecules and motors will guide nanomaterial movements, sensors for diagnosis, actuators connected to the sensors to release therapeutic drugs, and secondary sensors to monitor the disease as it is being treated (Chan, 2006).

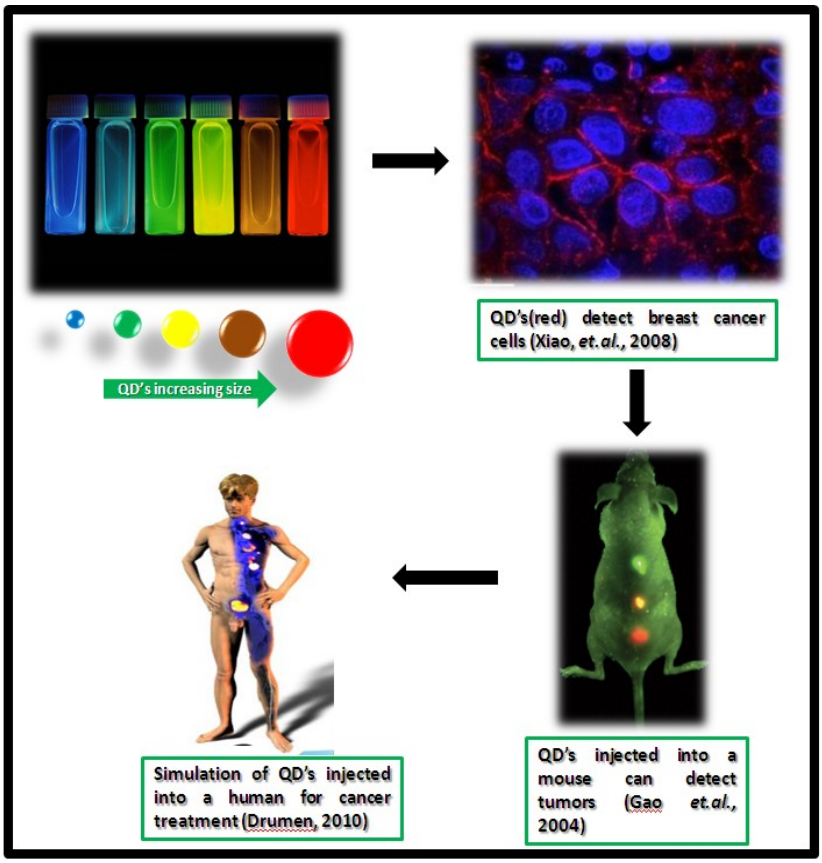

Figure 11. *Applications of quantum dots for detection of human cancer cells.*

Such devices will be able to diagnose and treat presently challenging diseases such as cancer, diabetes and/or Alzheimer disease. Predictions as to how long this will probably take range from 50 to 100 years (Chan, 2006).

II.4.2 Cellular targeting by nanoparticles

Nanotechnology applications in medicine, termed nanomedicine, aim to overcome problems related to diseases at the nanoscale where most of the biological molecules exist and operate (Wang and Thanou, 2010). Today, there is a strong focus on nanotechnological applications to diagnose and treat cancer. At present, the conventional cancer treatments work on the basis of chemical gradients of drugs that are delivered non-specifically to the whole body, as is the case with chemotherapy. This originates highly toxic side effects to normal or

healthy cells. One of the main goals of nanomedicine is to develop a safe and effective drug delivery system or drug carrier without damaging normal cells.

Nanocarriers such as drug-polymer conjugates, micelles, liposomes and nanoparticles hold great promise for cancer diagnosis and simultaneous drug delivery and therapy. Nanoparticles used as nanocarriers must be biocompatible and capable of identifying and delivering the drug at the required zone. This specificity of a nanoparticle can be made possible with adequate targeting. The targeting process itself is a multi-step process consisting of initial cell recognition by means of cell surface receptors, cell entry across the membrane in such a way that undesired alterations of the nanomedical system are prevented, re-targeting to the appropriate sub-region of the cell where the therapeutic package (drugs) should be delivered, and potentially controlling drug dosification (Haglund *et.al.,* 2009).

There are two different targeting strategies: passive and active. Passive targeting is achieved when the nanoparticles remain in the blood-stream at places where the vessel structure is normal, but extravasate through the leaky vasculature characteristic of the tumor site. Upon arrival at the target site, the nanoparticles release the drug in the close vicinity of the tumor cells (Lee et.al., 2007).

On the other hand, active targeting involves conjugating or functionalizing the nanoparticle with targeting molecules such as antibodies, ligands (linkers), peptides, nucleic acids that bind to the surface of nanoparticles. The targeting molecules recognize and bind directly to a receptor overexpressed on a tumor-cell surface (Gulloti and Yeo, 2009).

Basically, the idea translates directly to the ongoing effort in cancer research to reduce the systemic toxicity of chemotherapy. In particular, the actively targeted nanocarriers can provide a finely aimed intracellular drug reservoir (Gulloti and Yeo, 2009).

II.4.3 Nanotechnology for cancer treatment

Nanotechnology for cancer treatment is a rapidly growing field and has made a remarkable contribution to treatment strategies, by enabling site-specific release of chemotherapeutic agent, based on their physicochemical characteristics and biological properties (Ranganathan *et.al.*, 2012; Cho *et.al.,* 2008). Cancer is a highly heterogeneous and complex disease that encompasses a group of disorders characterized by continuous and indefinite cancer cell growth. Nanomedicine, previously defined, has introduced a number of functionalized nanoparticles of variable chemistry and structure for cancer diagnosis, treatment and imaging. Currently used nanoparticles in cancer therapeutics include liposomes, dendrimers, lipids, proteins, semiconductors, ceramics, viral and carbon nanotubes (CNT) (Byrne *et.al.,* 2008; Hahn *et.al.,* 2011; Naga and Siddiqui, 2011). The first nanoparticle systems for delivering cancer chemotherapy were the liposomes. Basically, liposomes are the essential building block of every cell membrane in the human body. Liposomes are usually sized from 25 nm to 1μm and consist of a lipid bilayer surrounding a water core hosting the drug. The first studies to report the efficiency of liposomes as nanoparticles focused on the improvement of biodistribution of the drug doxorubicin. The nature of doxorubicin, unfortunately also induces cardiotoxicity and this can limit the administered dose (Wang and Thanou, 2012). To avoid cardiotoxicity, doxorubicin was encapsulated in anionic liposomes, liposomal doxorubicin has been shown to be safe and efficient clinically, in ovarian and breast cancer (Straubinger *et.al.,* 1988; Robert *et.al.,* 2004).

Despite extensive research on nanoparticles for cancer therapeutics, there are only a few nanoparticles for drug delivery approved by the US Federal Drug Administration and European Medicines Agency. Specifically, the nanoparticles that have been approved include liposomal doxorubicin (Myocet; Elan Pharmaceuticals, Cedar Knolls, NJ), PEGylated liposomal doxorubicin (Doxill;

Ortho Biotech, and Caelyx; Schering Plough), PEGylated liposomal daunorubicin (DaunoXome Diatos), and the recently approved albumin-bound paclitaxel-loaded nanoparticles (Abraxane; Abraxis Bioscience) (Byrne *et.al.,* 2008).

Recently, carbon nanotubes (CNT) have shown great promise as nanoscale vehicles for targeted drug delivery, nanoscale size and easy functionalization makes single-walled carbon nanotubes (SWCNT) useful for drug delivery. In the past, CNT have been functionalized with antibodies and loaded with chemotherapeutic agents (Madani *et.al.,* 2011). It has been suggested that CNT could be used as nanocarriers for delivering drugs into the body via intravenous routes (Beg *et.al.,* 2011). CNT functionalized with drugs, in particular SWCNT, can be used as a new tool and useful method for potential drug delivery in cancer treatments (Khazaei *et.al.,* 2008). One important disadvantage of SWCNT is poor solubility. The multi-wall carbon nanotubes (MWCNT) have a shorter incubation time and present cytotoxicity (Jabir *et.al.,* 2012).

At present, due to the cytotoxicity and the poor solubility of CNT, research is concentrating on obtaining new biocompatible inorganic materials to be applied as nanocarriers. The present work studies the physical and biological properties of hydroxyapatite impurified with europium and bismuth germanate nanoparticles and their applicability as nanocarriers.

Chapter III

Experimental Techniques

This chapter describes the experimental techniques used for the synthesis and characterization of europium-activated hydroxyapatite and bismuth germanate nanoparticles. It further on details the molecular techniques for nanoparticle functionalization with bovine serum albumin (BSA) protein and monoclonal W6/32 antibody. Additionally, it explains the targeting techniques for monocityc leukemia human tumor cells.

III.I Physical and chemical techniques

III.I.1 Sol-gel method

The sol-gel technique has proved to be a convenient route to prepare organic-inorganic hybrid compounds. Figure 12 shows the different stages of the sol-gel method: The first step of a sol-gel reaction is the formation of an inorganic polymer by hydrolysis and condensation reactions, i.e., the transformation of the molecular precursor into a highly crosslinked solid. Hydrolysis of this compound leads to a sol, a dispersion of colloidal particles in a liquid, and further condensation results in a gel, an interconnected, rigid and porous inorganic network enclosing a continuous liquid phase. This transformation is called the sol-gel transition. When the gel is dried, agglomeration of dense colloidal particles occurs and this is named a xerogel. One of the highly attractive features of the sol-gel process is the possibility of shaping the material into any desired form such as monoliths, films, fibers and nanoparticles, and to subsequently convert it into a ceramic material by heat treatment (Brinker and Scherer, 1990).

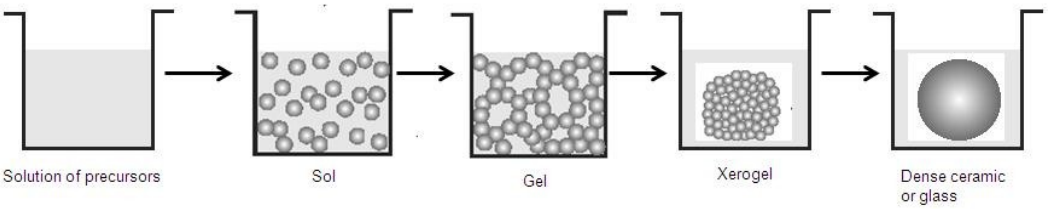

Figure 12. *Stages of the sol-gel technique.*

The sol-gel processes can be classified into two different routes depending on the nature of the precursors, which can be a) an aqueous solution of an inorganic salt or b) a metal-organic compound. The metal-organic route, which was used in this study, involves the formation of condensed species from aqueous solutions of inorganic powders by adjusting the pH, by increasing the temperature or by changing the oxidation state (Livage, *et.al.,*1988).

III.I.2 X-ray diffraction (XRD)

X-ray diffraction (XRD) is a versatile, non-destructive technique that reveals detailed information about the crystalline structure of materials and can identify chemical compounds. The crystal structure is studied by analyzing the diffraction of photons, neutrons and electrons. The diffraction pattern will depend on both the crystal structure and the wavelength (Kittel, 2005).

X-rays are electromagnetic waves with a wavelength (λ) in the order of 0.1 nm. X-ray diffraction methods are based on the phenomenon of wave interferences. Two light waves with the same wavelength and traveling in the same direction can either reinforce or cancel each other, depending on their phase difference. When they have a phase difference of $n\lambda$ (n is an integer) it is called in-phase, constructive interference occurs. When they have a phase difference of $n\lambda/2$, called out-of-phase, destructive interference occurs (Leng, 2008).

X-ray beams incident on a crystalline solid will be diffracted by the crystallographic planes as illustrated in Figure 13. Two incident waves in phase (1 and 2) are deflected by two crystal planes (A and B). The deflected waves will not be in phase except when the Brag law is satisfied (equation 3).

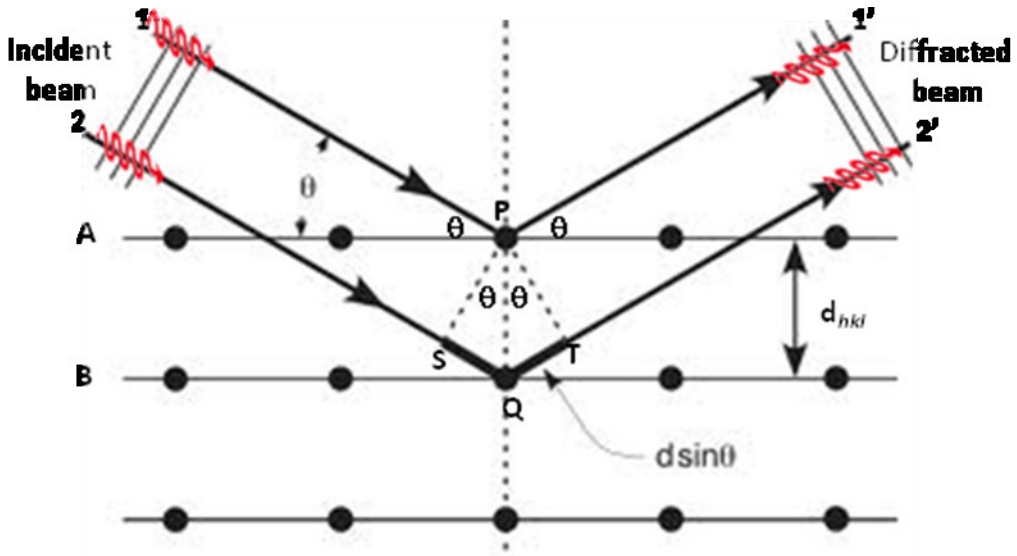

Figure 13. *Derivation of the Bragg equation, where d is the spacing of parallel atomic planes and 2πn is the difference in phase between reflections from successive planes.*

The Brag law can be obtained by calculating the path differences between the two beams in Figure 13. The path difference depends on the incident angle (θ) and spacing between the parallel crystal planes (d). In order to keep these beams in phase, their path difference (SQ+QT=2dsinθ) has multiple X-ray wavelengths (nλ) (Leng, 2008).

$$2d \sin \theta = n\lambda, \qquad (3)$$

We are able to obtain information on the spacing between atomic planes of a crystal when constructive interference is detected at a given incident angle and a wavelength of the incident beam, based on Bragg's law. Knowing the spacing of

crystallographic planes by diffraction methods, we can determine the crystal structure of materials. For example, the plane spacing (*d*) of a cubic crystal relates to the lattice parameter (*a*) by the following equation

$$d_{hkl} = a/(h^2+k^2+l^2)^{1/2}, \quad (4)$$

The Miller indices (h, k, l) represent a series of parallel planes in a crystal with spacing of d_{hkl}. Combining equation (3) and (4) we obtain the following relationship between diffraction data and crystal parameters for a cubic crystal system (Kittel, 2005).

$$Sin^2\theta = (\lambda^2/4a^2)(h^2+k^2+l^2), \quad (5)$$

Equation 5 does not directly provide the Miller indices of crystallographic planes, it is necessary to convert $(h^2+k^2+l^2)$ to (h k l) or {h k l} .

III.I.3 Transmission Electron Microscopy (TEM)

Electron microscopes generate images of material microstructures with much higher magnification and resolution than light microscopes. The high resolution of electron microscopy results from short wavelengths of the electrons used for microscope illumination (Leng, 2008). The wavelength of electrons in electron microscopes is about 10, 000 times shorter than the wavelength of visible light. Electron microscope resolution reaches the order of 0.1 nm. Such high resolution makes electron microscopes extremely useful for revealing ultrafine details of material microstructure.

The transmission electron microscope has the following components along its optical path: light source, condenser lens, specimen stage, objective lens and projector lens as shown in Figure 14.

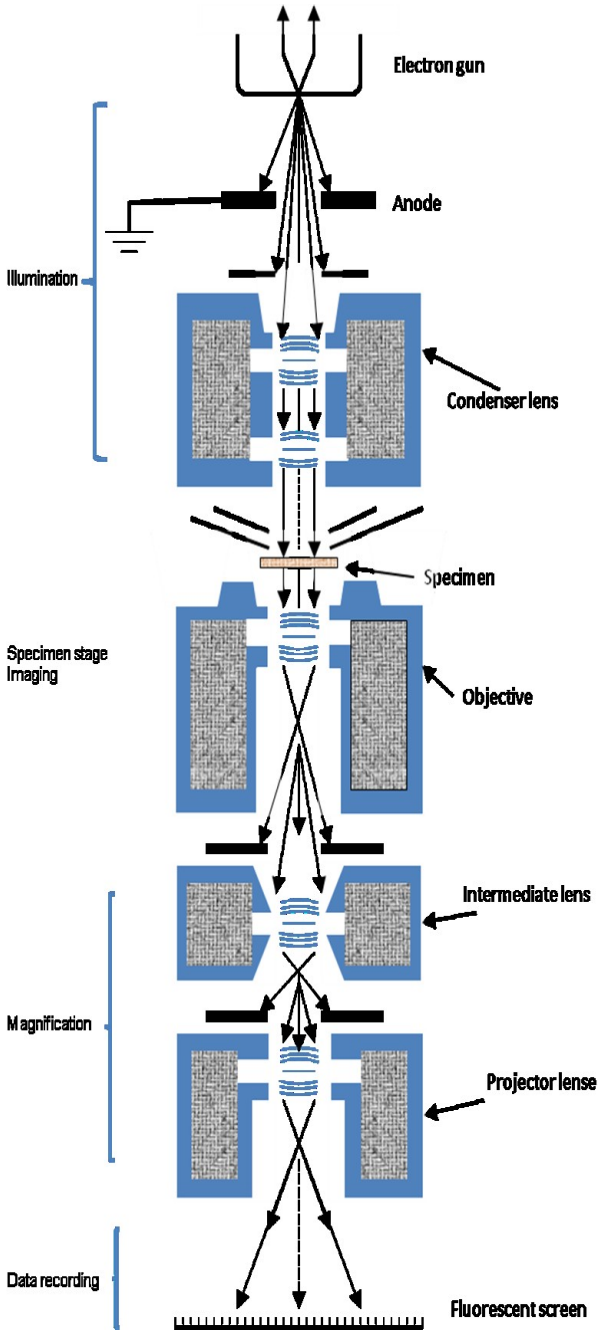

Figure 14. *Structure of a transmission electron microscope and components of the optical path. (Guerrero, 2012, p. 25)*

The main differences with a light microscope are that, in a TEM, the visible light ray is replaced by an electron ray and glass lenses for visible light are replaced by are electromagnetic lens for the electron beam. The TEM has more

lenses (intermediate lens) and more apertures. The TEM contains further features arising from using electrons as illumination (Leng, 2008). For example, a vacuum environment is required in a TEM because collision between high energy electrons and air molecules significantly absorb electron energy.

In a TEM system, an electron gun generates a high energy electron beam for illumination. In the electron gun, the electrons emitted from a cathode, a solid surface, are accelerated by high voltage (V_0) to form a high energy electron beam with energy $E=eV_0$, because electron energy determines the wavelength of electrons, and wavelength largely determines the resolution (R) of the microscope.

The TEM has special requirements for specimen observation; it does not have the same flexibility in this regard as a light microscope. TEM specimens must be a thin foil because they should be able to transmit electrons. A thin specimen is mounted in a specimen holder (carbon meshes) in order to be inserted into the TEM column for observation.

III.I.4 Photoluminescence spectroscopy

Photoluminescence (PL) spectroscopy has emerged as an important tool for studying the optical and electronic properties of solid state materials suited for optoelectronic applications. PL experiments provide relatively direct information about electron recombination and relaxation processes. In general, these experiments are useful for the investigation of the electronic properties of the excited state and offer several advantages over other optical techniques.

Metals, semiconductors and insulators such as bismuth germanate (BGO) have an energy gap for electron conduction. Consider that some of the electrons in a solid are not firmly attached to the atoms, as they are for single atoms, but can jump from one atom to another. These electrons are bound in the solid and thus have much different energy. Electrons having energies above a certain value are referred to as conduction electrons, while electrons having energies below a certain value are referred to as valence electrons. This is shown in the diagram

(Figure 15), where they are labeled conduction and valence bands. Furthermore, there is an energy gap between the conduction and valence electron states. The band gap is the difference in energy between the lowest point of the conduction band and the highest point of the valence band (Kittel, 2005). If a light particle (photon) has energy greater than the band gap energy, then it can be absorbed and thereby raise an electron from the valence band up to the conduction band across the forbidden energy gap, as shown in Figure 15 (Heiman, 2004).

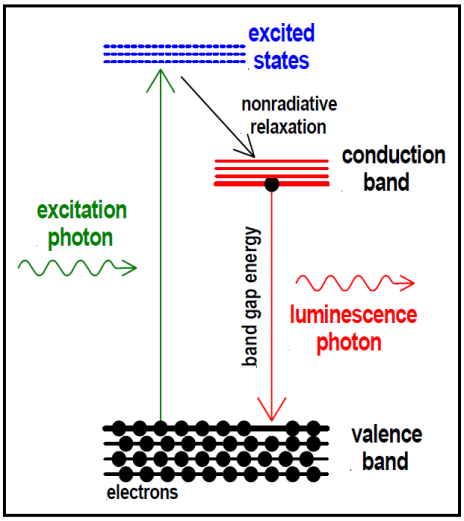

Figure 15. *Photoluminescence process in semiconductor material.*

In this process of photoexcitation, the electron generally has excess energy which it loses before coming to rest at the lowest energy of the conduction band. At this point, the electron eventually falls back down to the valence band. As it falls down, the energy it loses is converted back into a luminescent photon which is emitted from the material. Thus the energy of the emitted photon is a direct measure of the band gap energy, *Eg*. The process of photon excitation followed by photon emission is called photoluminescence. On the other hand, Radioluminescence (RL) is the phenomenon by which photons are produced in a material by the incidence of ionizing radiation such as X-rays, beta or gamma particles. In RL, the scintillation process is observed in inorganic materials due to

the electronic band structure found in crystals (See section II.4 for an explanation of the scintillation phenomenon).

The trivalent Eu ions have an outer electronic configuration $5s^2 5p^6 4f^n$, where *n* indicates the number of electrons in the unfilled *4f* level. The $4f^6$ level for Eu^{3+} electrons are, in fact, the valence electrons responsible for the optical transitions (Solé *et.al.,* 2005).

Figure 16 shows the emission spectrum of the Eu^{3+} ion in a host matrix of, $LiNbO_3$. This rare-earth ion (together with Tb^{3+} and Eu^{2+}) is commonly used in the fabrication of phosphors for red, green, and blue lamps. Its luminescence spectrum produces red radiation and consists of four groups of lines. These lines correspond to different transitions from the singly degenerate excited state $^5D_0$ to the different sublevels within four terminal states ^7F_J (from J = 1,2, 3, 4), the $^5D_0 \rightarrow {}^7F_0$ emission is forbidden at the electric dipole order and is not observed. For instance, the $^5D_0 \rightarrow {}^7F_1$ emission transition shows two peaks, because the terminal level $^7F_1$ splits into two levels (one singly degenerate and the other doubly degenerate). Similar analyses can be carried out for the remaining emission peaks related to the other $^5D_0 \rightarrow {}^7F_J$ transitions, thus yielding the splitting components of the other ^7F_J terminal levels.

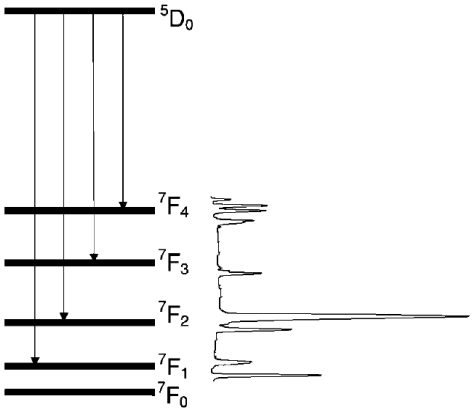

Figure 16. *Low temperature emission spectrum of Eu^{3+} in $LiNbO_3$.(Muñoz et.al., 1995, p.204)*

III.I.5 Decay time

The rate of decay of luminescence after excitation by a high energy particle (e.g. X-rays, γ-rays) is an important parameter for application and interpretation of scintillation phenomena.

To determine the decay rate, it must firstly be considered that the excitation intensity is kept constant at each wavelength. This situation corresponds to the stationary case (stationary optical excitation), in which optical feeding into the excited level equals the decay rate to the ground state, and so the emitted intensity remains constant with time. Relevant information can be obtained under pulsed wave excitation. This type of excitation promotes a nonstationary density of centers N in the excited state. These excited centers can decay to the ground state by radiative (light-emitting) and nonradiative processes, giving a decay-time intensity signal (Solé *et.al.,* 2005). The temporal evolution of the excited state population follows the general rule:

$$dN(t)/dt = -A_T\, N(t), \qquad (6)$$

where A_T is the total decay rate (or total decay probability), which is written as:

$$A_T = A + A_{nr}, \qquad (7)$$

where A is the radiative rate (labeled in such way that it coincides with the Einstein coefficient of spontaneous emission), and A_{nr} is the nonradiative rate; that is, the rate for nonradiative processes. The solution of the differential equation (6) gives the density of excited centers at any time t:

$$N(t) = N_0 e^{-A_T t}, \qquad (8)$$

where N_0 is the density of excited centers at $t = 0$; that is, just after the pulse of light has been absorbed.

The de-excitation process can be experimentally observed by analyzing the temporal decay of the emitted light. In fact, the emitted light intensity at a given time *t,* $I_{em}(t)$, is proportional to the density of centers de-excited per unit time, (d*N*/d*t*) radiative = $AN(t)$, so that it can be written as

$$I_{em}(t) = C \times AN(t) = I_0 e^{-A_T t}, \qquad (9)$$

where *C* is a proportionality constant and so $I_0 = C \times AN_0$ is the intensity at $t = 0$. Equation (9) corresponds to an exponential decay law for the emitted intensity, with a lifetime given by $\tau = 1/A_T$. This lifetime represents the time in which the emitted intensity decays to I_0/e and it can be obtained from the slope of the linear plot, log *I* versus *t* (Solé *et.al., 2005).*

III.I.6 Infrared (IR) and Raman spectroscopy

Infrared spectroscopy (IR) is one of the most important and widely used analytical techniques available to scientists working in a range of fields. IR is a versatile experimental technique, and can be used to obtain important information from delicate biological samples to tough minerals. Infrared spectroscopy is a technique based on the vibrations of the atoms of a molecule. An IR spectrum is commonly obtained by passing infrared radiation through a sample and determining what fraction of the incident radiation is absorbed at a particular energy. The energy at which any peak in an absorption spectrum appears corresponds to the frequency of a vibration of a part of a sample molecule.

The visible part of the electromagnetic spectrum is, by definition, radiation visible to the human eye. Other detection systems reveal radiation beyond the visible regions of the spectrum and these are classified as radiowave, microwave, infrared, ultraviolet, X-ray and γ-ray. These regions are illustrated in Figure 17, together with the processes involved in the interaction of the radiation of these

regions with matter. The electromagnetic spectrum and the varied interactions between these radiations and many forms of matter can be considered in terms of either classical or quantum theories (Stuart, 1997).

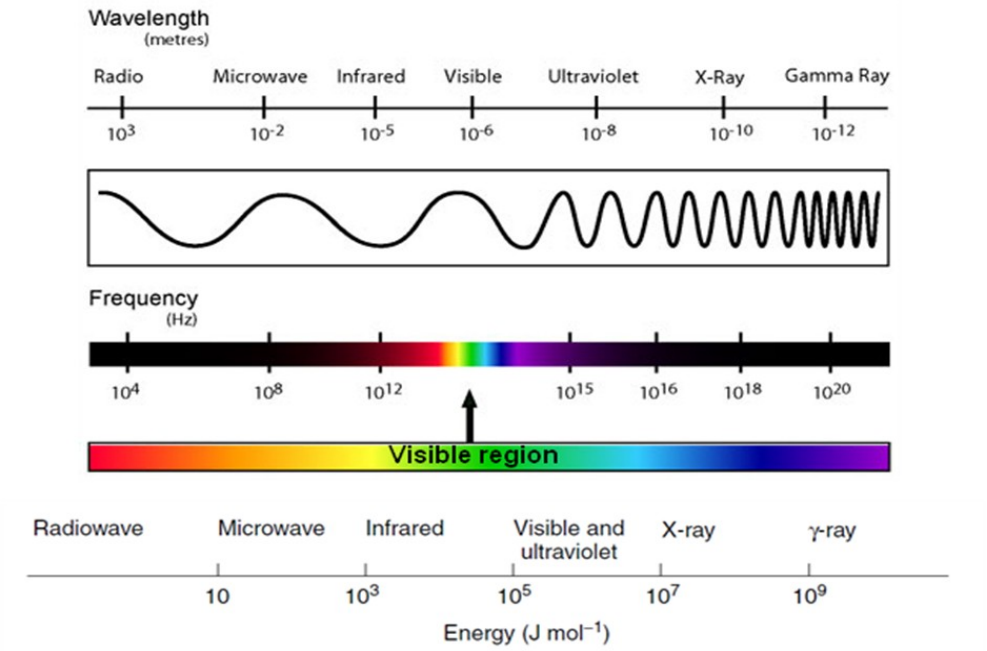

Figure 17. *Regions of the electromagnetic spectrum. (Stuart, 1997)*

For a molecule to show infrared absorption it must possess a specific feature, *i.e.* an electric dipole moment of the molecule must change during the vibration. This is the *selection rule* for infrared spectroscopy. Figure 18 illustrates a diagram of an ‘infrared-active’ molecule, a heteronuclear diatomic molecule. The dipole moment of such a molecule changes as the bond expands and contracts. By comparison, an example of an ‘infrared-inactive’ molecule is a homonuclear diatomic molecule because its dipole moment remains zero.

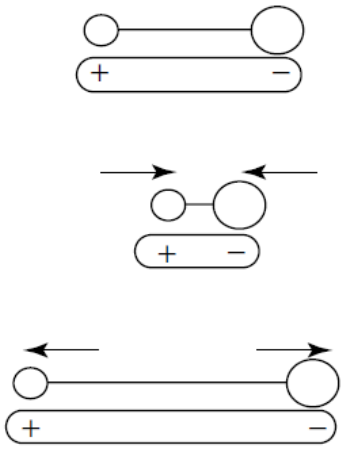

Figure 18. *Change in the dipole moment of heteronuclear diatomic molecule. (Stuart, 1997, p. 6)*

Infrared absorptions are not narrow and there are several factors that contribute to the broadening. For gases, the Doppler effect, in which radiation is shifted in frequency when the radiation source is moving towards or away from the observer, is a factor. There is also the broadening of bands due to the collisions between molecules. Another source of line broadening is the finite lifetime of the states involved in the transition.

The interactions of infrared radiation with matter may be understood in terms of changes in molecular dipoles associated with vibrations and rotations. Vibrations can involve either a change in bond length (*stretching*) or bond angle (*bending*), some bonds can stretch in-phase (*symmetrical* stretching) or out-of-phase (*asymmetric* stretching), as shown in Figure 19.

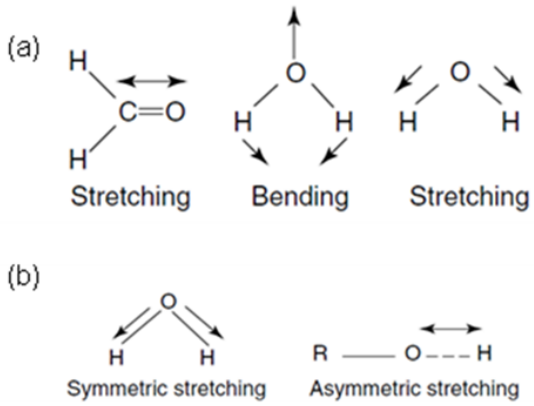

Figure 19. *Stretching and bending vibrations. (b) Symmetric and asymmetric stretching vibrations. (Stuart, 1997, p.7-8)*

One of the most common applications of infrared spectroscopy is the identification of organic compounds. For example, amines: primary ($^{-}NH_2$), secondary (^{-}NH) and tertiary (no hydrogen attached to N) amines may be differentiated by using infrared spectra. Primary amines have two sharp N–H stretching bands near 3335 cm^{-1}, a broad NH_2 scissoring band at 1615 cm^{-1}, and NH2 wagging and twisting bands in the 850–750 cm^{-1} range. Secondary amines show only one N–H stretching band at 3335 cm^{-1} and an N–H bending band at 1615 cm^{-1}. The N–H wagging band for secondary amines appears at 715 cm^{-1}. Tertiary amines are characterized by an N–CH_2 stretching band at 2780 cm^{-1}. All amines display C–N stretching bands, with aromatic amines showing such bands in the 1360–1250 cm^{-1} range and aliphatic amines showing bands at 1220–1020 cm^{-1} (Schrader, 1995).

On the other hand, the Raman spectroscopy is based on the inelastic scattering of light by matter and is capable of probing the structure of gases, liquids, and solids, both amorphous and crystalline. In addition to its applicability to all states of matter, Raman spectroscopy has a number of other advantages. It can be used to analyze tiny quantities of material (e.g., particles that are ~1 μm on edge), as well as samples exposed to a variety of conditions such as high temperature and high pressure and samples embedded in other phases, so long

as the surrounding media are optically transparent. Succinctly stated, Raman scattering results from incident radiation inducing transitions in the atoms/molecules that make up the scattering medium. The transition can be rotational, vibrational, electronic, or a combination (but first-order Raman scattering involves only a single incident photon) (Kaufmann, 2003).

In a Raman experiment, the sample is irradiated with monochromatic radiation. If the sample is transparent, most of the light is transmitted, a small fraction is elastically (Rayleigh) scattered, and a very small fraction is inelastically (Raman) scattered. The inelastically scattered light is collected and dispersed, and the results are presented as a Raman spectrum, which plots the intensity of the inelastically scattered light as a function of the shift in wavenumber of the radiation. The wavenumber of a wave is the reciprocal of its wavelength and is proportional to its momentum in units of reciprocal centimeters. Each peak in the spectrum corresponds to one or more vibrational modes of the solid. The total number of peaks in the Raman spectrum is related to the number of symmetry modes allowed. The Raman active modes are shown in Figure 20. Some of the modes may be degenerate and some may have Raman intensities that are too low to be measured, in spite of their symmetry allowed nature (Kaufmann, 2003).

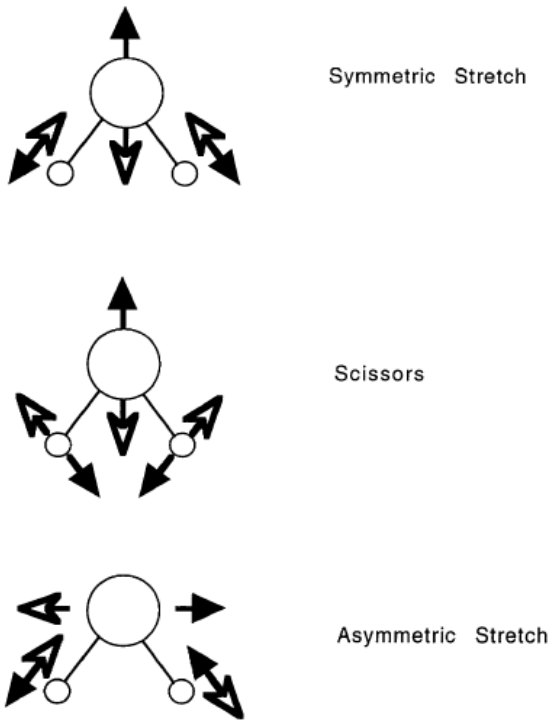

Figure 20. *Normal vibrational modes of H_20. (Kaufmann, 2003, p.698)*

Consequently, the number of peaks in the Raman spectrum will be less than or equal to the number of Raman active modes. The practical usefulness of Raman spectroscopy resides largely in the fact that the Raman spectrum serves as a fingerprint of the scattering material. In fact, Raman activity is a function of the point group symmetry of a molecule and the space group symmetry of a crystalline solid; it can provide a range of information, including the strength of interatomic and intermolecular bonds, the mechanical strain present in a solid, the composition of multicomponent matter, the degree of crystallinity of a solid, and the effects of pressure and temperature on phase transformations.

For materials that are both Raman active and IR active, the Raman scattering cross-section is much smaller than the IR absorption cross-section so the incident radiation needs to be more intense and the detectors need to be more sensitive for Raman spectroscopy than for IR spectroscopy. Because of the fundamental differences between absorption and scattering of electromagnetic

radiation, some vibrational modes of a material may be Raman active but not IR active. In particular, for a molecule with a center of symmetry, vibrational modes that are Raman active are IR inactive, and vice versa. Consequently, when deciding between IR and Raman spectroscopies, the point group or space group symmetry of the material needs to be taken into account (Scrhader, 1995).

III.I.7 Atomic Force Microscopy (AFM)

Atomic force microscopy (AFM) is currently applied to different environments (air, liquid, vacuum) and types of materials such as metal semiconductors, soft biological samples, conductive and non-conductive materials. With this technique, size measurements or even manipulation of nano-objects may be performed.

AFM provides a number of advantages over conventional microscopy techniques. For example, AFM can characterize contact lenses in their native liquid environment (operation in liquid), the AFM can observe live cells and/or bacteria in an appropriate environment, the technique is non-destructive in air or in liquid; the AFM characterizes the sample without damage. AFM can determine chemical and mechanical properties of materials including surface adhesion, hardness, and friction. An AFM tip can be chemically modified in order to measure tip/sample interactions. In contrast, the environment of the scanning and confocal microscopes is usually limited to ambient air or vacuum chamber, and these microscopes not useful for characterizing chemical and mechanical surface properties (Park and Brucker manuals). AFM probes the sample and makes measurements in three dimensions, x, y and z (normal to the sample surface), thus enabling the presentation of three-dimensional images of a sample surface. This provides great advantages over any microscope previously available. With good, clean samples with no excessively large surface features, resolution in the x-y plane ranges from 0.1-1.0 nm and in the z direction is 0.01 nm (atomic resolution).

AFM requires neither a vacuum environment nor special sample preparation, and can be used in either an ambient or liquid environment (Blanchard, 1996). Figure 21 shows the basic configuration for most AFMs. This AFM is typically used to measure a wide variety of samples of small roughness. The force between the atoms at the sample surface and those at the cantilever tip can be detected by monitoring how much the cantilever deflects. This deflection of the cantilever can be quantified by the measurement of a laser beam that is reflected off the backside of the cantilever and onto the position-sensitive photo detector (PSPD). The tube-shaped scanner located under the sample moves a sample in the horizontal direction (X-Y) and in the vertical direction (Z). It repetitively scans the sample line by line, while the PSPD signal is used to establish a feedback loop which controls the vertical movement of the scanner as the cantilever moves across the sample surface.

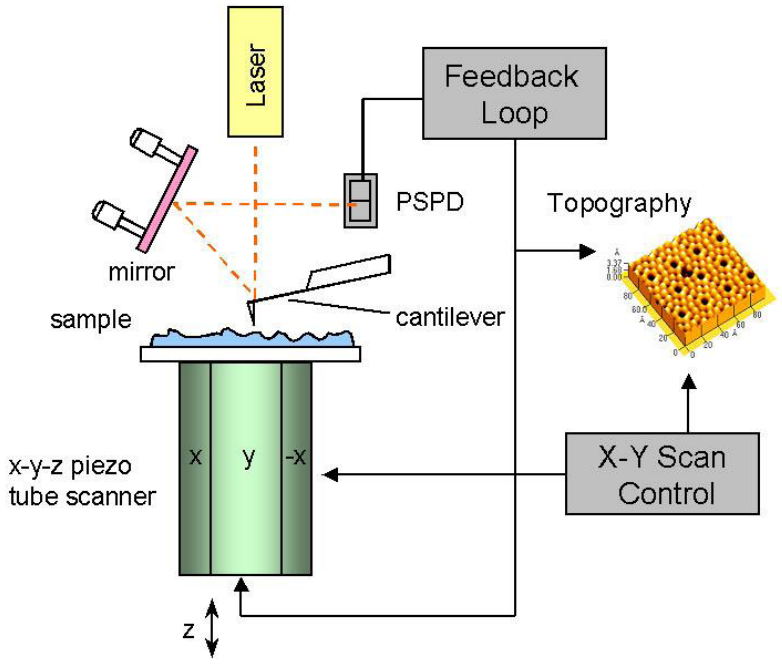

Figure 21. *Diagram of conventional AFM scanning. (Park, 2011, p.46)*

There are several types of cantilevers varying in material, shape, softness and intrinsic frequency, among others. The selection of cantilever from among

these is primarily determined by the type of the measurement mode. AFM have two modes of measurements: contact and non-contact mode.

- Contact mode: a soft cantilever, whith a small spring constant (0.01-0.3 N/m) responds sensitively to the tiny force between atoms is usually chosen. The probe tip used in the contact mode has a thickness of about 1μm to achieve a small spring constant. This is because a cantilever with a small spring constant makes a relatively large deflection to a small force, and can thus provide a very fine image of the surface structure.

- Non-contact mode: the cantilever has a larger thickness (~4μm) compared to the contact mode. It has a spring constant of 40 N/m which is very stiff and a relatively large resonant frequency. While the contact mode detects the bending of a cantilever, the non-contact mode vibrates the cantilever at a high resonant frequency, and measures the force gradient by the amplitude and phase change due to the interaction between the probe and the sample, which yields the topography of the sample. When an AFM is operating in the atmosphere, or if the probe tip is situated on a moist or contaminated layer, it may often stick to the layer due to the surface tension of the tip. This happens more frequently if the spring constant of the cantilever is smaller. Because of the small spring constant, it is difficult to bring it back to the original position. Therefore, it needs a cantilever with a spring constant which can overcome the surface tension (Park, 2011).

II.I.8 Medical radiology

Radiology is a non-invasive medical test that helps physicians diagnose and treat medical conditions such as tumors. X-rays imaging involves exposing a part

of the body to a small dose of ionizing radiation to produce pictures of the inside of the body; X-rays are the oldest and most frequently used form of medical imaging.

X-rays are a form of radiation, the rays pass through most objects, including the body. Once it is carefully aimed at the part of the body being examined, an X-ray machine produces a small burst of radiation that passes through the body, recording an image on photographic film or a special digital image recording plate. Different parts of the body absorb X-rays in varying degrees. Dense bone absorbs much of the radiation, while soft tissue, such as muscle, fat and organs, allow more of the X-rays to pass through them. As a result, bones appear white on the X-ray image, soft tissue shows up in shades of gray and air appears black. Radiology poses advantages and disadvantages, for example:

Advantages

- Bone X-rays are the fastest and easiest way for a physician to view and assess fractured bone and joint abnormalities, such as arthritis and spine injuries.
- X-ray equipment is relatively inexpensive and widely available in emergency rooms, physician offices, ambulatory care centers, nursing homes and other locations, making it convenient for both patients and physicians.
- Because X-ray imaging is fast and easy, it is particularly useful in emergency diagnosis and treatment.
- No radiation remains in a patient's body after an x-ray examination.
- X-rays usually have no side effects in the diagnostic range.

Disadvantages

- There is always a slight chance of cancer from excessive exposure to radiation. However, the benefits of accurate diagnosis far outweigh the risk. The effective radiation dose for this procedure varies.
- Special care is taken during X-ray examinations to use the lowest radiation dose possible while producing the best images for evaluation.

State-of-the-art X-ray systems have tightly controlled X-ray beams with significant filtration and dose control methods to minimize stray or scatter radiation. This ensures that those parts of a patient's body not being imaged receive minimal exposure to radiation. Table IV shows the comparisons of effective radiation dose with background radiation exposure for several radiological procedures (Radiological Society of North America, 2012)

Table IV. *Effective radiation dose for different radiological procedures. (Radiological Society of North America, 2012)*

Procedure	Approximate effective radiation dose (mSv)	Natural background radiation (years)	Lifetime risk of fatal cancer from examination
Abdominal region:			
Computer tomography (CT)-abdomen and pelvis	10	3	Low
Radiography (X-ray) – lower GI tract	8	3	Low
Radiography (X-ray) – upper GI tract	6	2	Low
BONE:			
Radiography (X-ray)-spine	1.5	6 months	Very low
Radiography (X-ray)-extremity	0.001	3 hours	Negligible
CHEST:			
Computed tomography (CT)-chest low dose	1.5	6 months	Very low
Radiography-chest	0.1	10 days	minimal
Women's imaging:			
Bone dositometry	0.001	3 hours	Negligible
Mammography	0.4	1 week	Very low

In this work, radiology was used to tested if could be possible to identify the bismuth germanate nanoparticles inside of a human body using a very low dose of high energy radiation.

III.2 Biomolecular techniques

III.2.1 Functionalization and protein quantification

Functionalization of nanoparticles consists in attaching proteins to their surface. These proteins will serve to locate and identify antigens or receptors on the surface of certain cells. In brief, nanoparticles are mixed with a known amount of protein and, after reaction, nanoparticles coated with protein are collected by centrifugation, and the amount of residual protein in the supernatant is estimated using a conventional protein assay. The amount of conjugated protein is then calculated as the difference between the fed and the residual protein (Voltan *et.al.,* 2007; Zhou *et.al.,* 2010; Cui *et.al.* 2011).

Commonly, the amount of protein conjugated to the surface of nanoparticles is determined by measuring remaining protein after bioconjugation, as described above. However, indirect and semi-quantitative methods have been used to determine the protein coating of nanoparticles, such as: UV absorption spectroscopy (Vinayaka *et.al.,* 2011; Choi *et.al.,* 2012), dynamic light scattering (DLS) (Zhou *et.al.,* 2010; Choi *et.al.,* 2012) , quartz crystal microbalance data (QCM) (Choi *et.al.,* 2012; Giri *et.al.,* 2011), transmission electron microscopy (TEM) (Yang *et.al.,* 2011), atomic force microscopy (AFM) (Valo *et.al.,* 2011; Ge *et.al.,* 2011), ultrafast X-ray scattering (Ibrahimkutty *et.al.,* 2011), Fourier transform infrared (FT-IR) spectroscopy (Samanta *et.al.,* 2008), thermo-gravimetry (Hommes *et.al.,* 2012) or enzymatic activity when enzymes are used (Hommes *et.al.,* 2012; Qhobosheane *et.al.,* 2001; Ha *et.al.,* 2005). In some cases, to verify the nanoparticle-protein interaction, another protein, such as green fluorescent protein (GFP) has been used (Valo *et.al.,* 2010). The labeling of superficial protein with a flourophore has also been performed (Chithrani *et.al.,* 2007). Attempts to directly

measure attached protein by conventional determinations, as used for protein solutions, have been reported. Since protein content is measured using a UV-vis absorption method, a control for light absorbance by the suspended solid particles is needed, reducing the accuracy of the determination due to the not negligible source of interference (Stayton *et.al.,* 2009).

A method to directly determine the amount of protein conjugated on the surface of nanoparticles is presently reported. A known amount of reagent dye is added to the protein-coated nanoparticles. Then they are centrifuged and the reagent remaining in the supernatant is titrated with an excess of protein. The protein coating on the surface of the nanoparticles is estimated by subtracting the unbound protein from the amount initially added to the reagent dye. The reagent dye concentration is transformed to BSA protein equivalents by a standard curve. Two controls are assayed, one with uncoated nanoparticles to estimate the possible unspecific adsorption of reagent dye, and another without nanoparticles to determine the initial amount of reagent dye.

In the Bio-Rad Protein Assay, the Coomassie blue dye binds to basic and aromatic amino acid residues, especially arginine (Bradford, 1976), displaying a color change in response to protein concentration. This is also known as the Bradford method (Compton, 1986). A color shift from 465 nm to 595 nm occurs in the presence of proteins. The absorbance increase at 595 nm follows Lambert and Beer's law, thus allowing accurate protein quantification by the following equation

$$Abs = -ln(I_t/I_0), \qquad (10)$$

where *Abs* is absorbance, I_t the transmitted intensity and I_0 the incident intensity.

As in all analytical methods, this procedure may have interferences. The interferences may be caused by chemical-protein or chemical-dye interactions. In general, the mass of a peptide or protein must be at least 3000 Daltons to be detectable with this reagent. Table V lists selected chemicals and concentrations that do not affect the color development of the dye. Because the reaction is carried

out in acidic conditions, basic buffers and detergents interfere with the assay. Contrarily to the manufacturer's report, organic solvents, such as acetone, ethanol, methanol and acetonitrile, significantly affect this assay.

Table V. *List of chemicals compatible with the Bio-Rad method for protein determination. Data from the Bio-Rad brochure "Bio-Rad Protein Assay" (Bio-Rad Laboratories, Hercules, CA).*

Chemical	Concentration	Chemical	Concentration
Acetate	0.6 M	Glycine	0.01 M
Adenosine	1 mM	Guanidine-HCl	
Amino acids		Malic acid	0.2 M
$(NH_4)_2SO_4$	1.0 M	$MgCl_2$	1.0 M
Acids	Low pH	Mercaptoethanol	1.0 M
ATP	1 mM	MES	0.7 M
Boric acid		NaCl	5 M
Citrate	0.05 M	NaSCN	3 M
Deoxycholate	0.01 %	Phenol	5 %
Dithiothrietol	1 M	Phosphate	1.0 M
DNA	1 mg/mL	Polyadenylic acid	1 mM
EDTA	0.1 M	Pyrophosphate	0.2 M
EGTA	0.05 M	RNA	0.3 mg/mL
Formic acid	1.0 M	SDS	0.1 %
Fructose		Na_3PO_4	
Glucose		Triton X-100	0.1 %
Glutathione		Tris	2.0 M
Glycerol	99 %	Urea	6.0 M

The method presented in this study is a direct and accurate technique to quantify the amount of protein conjugated (attached) to nanoparticles. Moreover, it confirms that nanoparticles can be functionalized with biological molecules.

III.2.2 Oxidative stress

At present, nanomaterials are being used commercially as catalysts, cosmetics in microelectronics and as drug carriers (Zhang *et.al.,* 2009; Rivero, *et.al.,* 2009; Wu *et.al.,* 2009). It is therefore foreseeable that human bodies will be increasingly exposed to nanomaterials. So, it is important to consider the risks entailed. Nanomaterial particles are smaller than cells and cell organelles, so they may penetrate the cellular membrane and produce important physical damage. Oxidative stress caused by nano-sized particles can damage lipids, carbohydrates, proteins and DNA. In particular, lipid peroxidation is considered highly dangerous as it alters cell membrane properties (Lin, *et.al., 2006*). For example, Fullerenes are lipophilic and are inserted into lipid-rich regions such as liver and gills in fish. Other nanomaterials have been shown to selectively translocate into the brain via the olfactory bulb in mammals and fish (Oberdosrster, 2004).

The interactions of nanomaterials with proteins, enzymes and DNA are thought to cause oxidative stress and cytotoxicity. In this regard, several proteins have been investigated during recent years, e.g. fibrinogen, hormones and lysine (Larsericsdotter *et.al.,* 2005; Norde *et.al.,*1999; Roddick-Lanzilotta *et.al.,* 1998).

The zebrafish is a useful model for investigating oxidative stress and cytotoxicity in vertebrates, in contrast to other vertebrate models, because it is completely transparent, facilitating visual multi-parameter observation and analysis, and because of its low cost and concordance with mammalian developmental phenotypes. Another important advantage of this animal model is that the morphological and molecular bases of tissue and organ development in zebrafish are, in general, either identical or similar to other vertebrates including man (Chen *et. al.,* 1996). Because of these advantages, the zebrafish has been considered as

an alternative model for traditional *in vivo* stress oxidative assays (Sipes *et. al., 2011).*

The oxidation of proteins in vertebrates has been the subject of several investigations (Stadtman and Oliver, 2005). Furthermore, oxygen radicals have been considered an important cause of oxidative modification of proteins, which may lead to their rapid degradation (Davies, 1987). Among the various oxidative modifications of amino acids in proteins, carbonyl formation may be an early marker for protein oxidation (Stadtman, 1991). This type of alteration was characterized as metal catalyzed oxidation of proteins, a reaction which has been extensively studied. The molecular mechanism of this type of protein oxidation has been reviewed elsewhere (Davies, 1990; Stadtman, 1990). In brief, redox cycling cations such as Fe^{2+} or Cu^{2+}can bind to cation-binding locations on proteins and with the aid of further attack by H_2O_2 or O_2 can transform side-chain amine groups of several amino acids into carbonyls (Stadtman, 1990, Dalle-done, 2001). The most likely amino acid residues to form carbonyl derivatives are lysine, arginine, proline and histidine. However, metal-catalyzed oxidation of proteins is not necessarily the only mechanism by which carbonyls are introduced into proteins.

Several approaches have been made to detect and quantify the levels of carbonyls in purified proteins as well as in proteins of crude extracts of various tissues. Among these are reactions with tritiated borohydride, reaction with 2,4 dinitrophenylhydrazyne (DNPH), and reaction with fluorescein thiosemicarbazide for electrophoresis (Levine *et.al.,* 1990). The most convenient procedure to be used on a routine basis is the spectrophotometric method for the detection of the reaction of dinitrophenylhydrazyne with protein carbonyls to form protein hydrazones (Dalle-done, 2001).

The procedure consists in breaking down tissue with an electrical or hand-operated homogenizer. An amount of 150-200 mg of tissue is homogenized with a buffer in plastic dishes. Subsequently, the nucleic acids are removed, because they may erroneously contribute to higher estimation of carbonyls. The supernatant is separated from the precipitate. Then, they are reacted with

dinitrophenylhydrazine. The final precipitates are dissolved in 6 M of guanidine hydrochloride solution. Finally, the determination of carbonyl content is calculated by obtaining the spectra at 355-390 nm of the DNPH treated samples (Reznick and Packer, 1994).

For sample calculation of carbonyl value: the molar extinction coefficient of DNPH is used to calculate the concentration of carbonyls (equation 11)

$$C = Abs\ (355\text{-}390\ nm) / (2.2 \times 10^4 / 10^6), \quad (11)$$

where *C* is the concentration of DNPH (nmol/ml). For the reproducibility assay an intraassay of variation is performed. Several different pieces of the same tissue are thus assayed for carbonyl contents.

The sample deviation is defined as for the reproducibility assays. An analysis of variation is performed with $|X_i - \overline{X}|$. The percent deviation is given by equation (12)

$$Percent\ deviation = (\Sigma_i X_i - \overline{X} / n \times 100) / \overline{X}. \quad (12)$$

The procedure described in this section using DNPH to estimate the levels of carbonyls in proteins is a very sensitive and reproducible assay (Reznick and Packer, 1994).

If a synthetic material is to be used for biomedical applications, an important issue that must be settled is its biocompatibility with the live organism. For example, hydroxyapatite is a biocompatible material (Santavirta et.al., 1991). However, bismuth germanate has not been studied yet. This work presents an analysis of the oxidative stress caused by bismuth germanate nanoparticles in different tissues of live zebrafish.

III.2.3 Lipid peroxidation

Lipids are a heterogeneous group of compounds with several important functions in the body such as being an efficient source of energy, and constituents of cell membranes and nerve tissues (Murray, 2000). When lipids are oxidized without release of energy, unsaturated lipids go rancid due to oxidative deterioration when they react directly with molecular oxygen. This process is called lipid peroxidation (Halliwell and Gutteridge, 1999; Gutteridge and Halliwell, 1990).

Lipid peroxides are non-radical intermediates derived from unsaturated fatty acids, phospholipids, glycolipids, and cholesterol. Their formation occurs in enzymatic or non-enzymatic reactions involving activated chemical species known as reactive oxygen species which are responsible for toxic effects in the body and are capable of damaging most body cells (Meier, 1990). These ROS include, among others, hydroxyl radicals, lipidoxyl or peroxyl radicals, singlet oxygen, and peroxinitrite formed from nitrogen oxide (NO). These chemical forms are defined as any species capable of independent existence that contains one or more unpaired electrons, unstable and very reactive (Halliwell and Chirico, 1993). They are formed either by the loss of a single electron or the gain of a single electron by a non-radical. They can easily be formed when a covalent bond is broken if one electron from each of the pair shared remains with each atom; this mechanism is known as homolytic fission. In water, this process generates the most reactive species, hydroxyl radical $OH^{\cdot}$. Chemists know well that combustion which is possible at high temperature to the rupture of C-C, C-H or C-O bonds, is a free-radical process. The opposite of this mechanism is the heterolytic fission in which, after a covalent break, one atom receives both electrons, which gives a negative charge, while the other remains with a positive charge.

In order to complete the analysis of the oxidative effect of bismuth germanate nanoparticles, lipid peroxidation levels were determined in different zebrafish tissues.

III.2.4 Flow Cytometry

Flow cytometry is a technique that simultaneously measures and then analyzes multiple physical characteristics of single particles, usually cells, as they flow in a fluid stream through a beam of light. The properties measured include a particle's relative size, relative granularity or internal complexity, and relative fluorescence intensity. These characteristics are determined using an optical to electronic coupling system that records how the cell or particle scatters incident laser light and emits fluorescence.

A flow cytometer is made up of three main systems: fluidics, optics, and electronics (Figure 22).

• The fluidics system transports particles in a stream to the laser beam for analysis.

• The optics system consists of lasers that illuminate the particles in the sample stream and optical filters that direct the resulting light signals to the appropriate detectors.

• The electronics system converts the detected light signals into electronic signals that can be processed by the computer. For some instruments equipped with a sorting feature, the electronics system is also capable of initiating sorting decisions to charge and deflect particles.

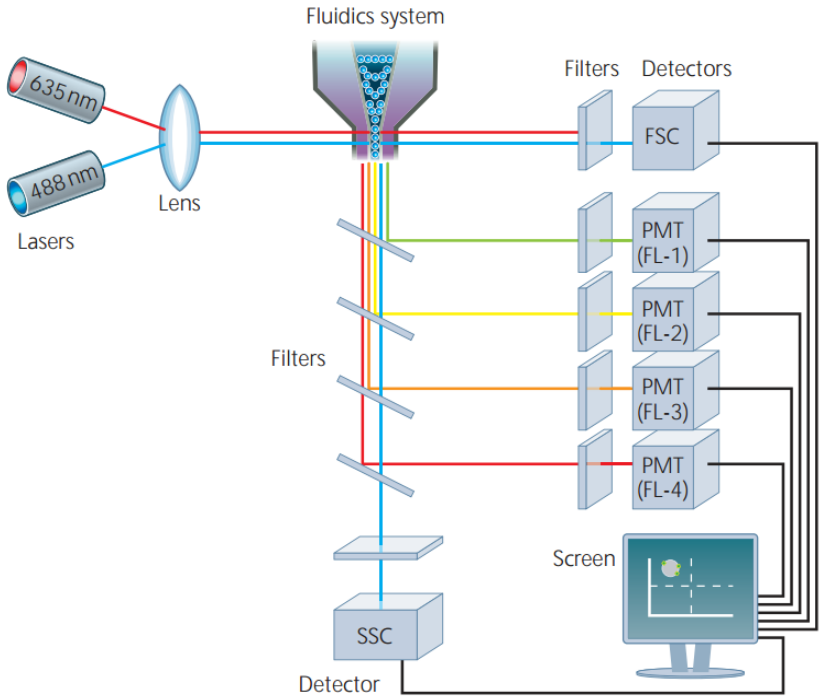

Figure 22. *Schematic overview of a typical flow cytometer. (Rashman, 2010, p. 7)*

In the flow cytometer, particles are carried to the laser intercept in a fluid stream. Any suspended particle or cell of 20 nm–150 micrometers in size is suitable for analysis. Cells from solid tissue must be disaggregated before analysis. The portion of the fluid stream where particles are located is called the sample core. When particles pass through the laser intercept, they scatter laser light. Fluorescent molecules present on the particle are detected, and their intensity is measured.

Light scattering occurs when a particle deflects incident laser light. The extent to which this occurs depends on the physical properties of a particle, namely its size and internal complexity. Factors that affect light scattering are the cell's membrane, nucleus, and any granular material inside the cell. Cell shape and surface topography also contribute to the total light scatter.

Forward-scattered light (FSC) is proportional to cell-surface area or size. FSC is a measurement of mostly diffracted light and is detected just off the axis of

the incident laser beam in the forward direction by a photodiode, as shown in Figure 23.

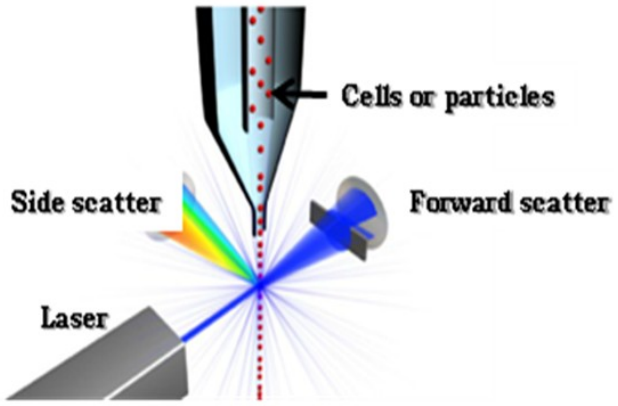

Figure 23. *Light-scattering properties of particles.*

Side-scattered light (SSC) is proportional to cell granularity or internal complexity. SSC is a measurement of mostly refracted and reflected light that occurs at any interface within the cell where there is a change in refractive index (Figure 23). SSC is collected at approximately 90 degrees to the laser beam by a collection lens and then redirected by a beam splitter to the appropriate detector (Biosciences, 2000).

Correlated measurements of FSC and SSC can allow for differentiation of cell types in a heterogeneous cell population. Major leucocyte subpopulations can be differentiated using FSC and SSC (Figure 24).

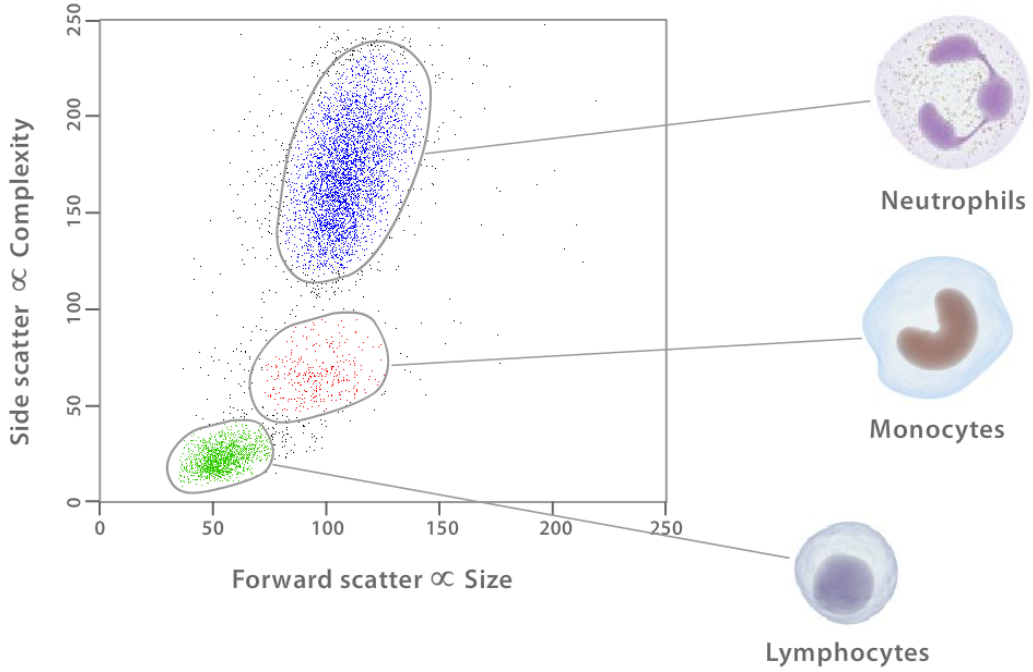

Figure 24*.Distribution of lymphoid cells according to their size and complexity. Lymphocytes are small cells with low internal complexity. Monocytes are medium size, with slightly more internal complexity. Neutrophils are large cells with a marked internal complexity.*

In fluorescence analysis, the range over which a fluorescent compound can be excited is termed its absorption spectrum. As more energy is consumed in absorption transitions than is emitted in fluorescent transitions, emitted wavelengths will be longer than those absorbed. The range of emitted wavelengths for a particular compound is termed its emission spectrum (Rashman, 2000).

The argon ion laser is commonly used in flow cytometry because the 488 nm light that it emits excites more than one fluorochrome (dye). When a fluorescent dye is conjugated to a monoclonal antibody, it can be used to identify a particular cell type based on the individual antigenic surface markers of the cell (Figure 25).

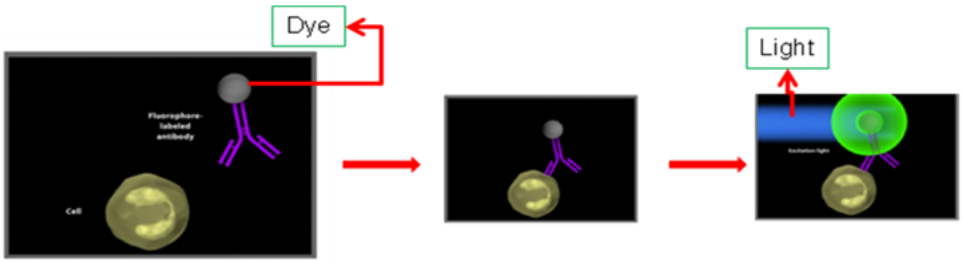

Figure 25. S*pecific binding of dye labeled antibodies to cell surface antigens.*

In a mixed population of cells, different fluorochromes can be used to distinguish separate subpopulations. The staining pattern of each subpopulation, combined with FSC and SSC data, can be used to identify which cells are present in a sample and to count their relative percentages. The cells can also be sorted if desired.

Furthermore, if europium-activated hydroxyapatite and bismuth germanate nanoparticles can be functionalized with antibodies and identify the human cancer cells, the flow cytometry technique give us the possibility to prove it.

III.2.5 Fluorescence microscopy

When light incides on a fluorescent molecule, it may absorb the light and then emit light of a different color. Fluorescein is a common fluorophore (dye) that acts this way, emitting green light when stimulated with blue excitation light. The wavelengths of the excitation light and the color of the emitted light are material dependent. Microscopy in the fluorescence mode has several advantages over the reflected or transmitted modes. It can be more sensitive. Often, it is possible to attach fluorescent molecules to specific parts of the specimen, making them the only visible ones in the microscope and it is also possible to use more than one type of fluorophore (Frigault *et.al.,* 2009; Tsien and Wagoner, 1995; Goldman *et.al.,* 2009). Thus, by switching the excitation light different parts of the specimen can be distinguished.

In conventional fluorescence microscopy a dyed specimen is illuminated with light of an appropriate wavelength and an image is formed from the resulting fluorescent light. In Figure 26 the excitation light is blue and the emitted light is green. The microscope uses a dichroic mirror (also called a ‘‘dichromatic mirror’’) that reflects light shorter than a certain wavelength, but transmits light of longer wavelength. Thus, the light from the main source is reflected and passes through the objective to the sample, while the longer-wavelength light from the fluorescing specimen passes through both the objective and the dichroic mirror. This particular type of fluorescence microscopy, in which the objective used by the illuminating light is also used by the fluorescing light in conjunction with a dichroic mirror, is called epifluorescence. In the case of reflected light microscopy, a beamsplitter is used in place of the dichroic mirror (Goldman *et.al.,* 2009; Hibbs, 2004).

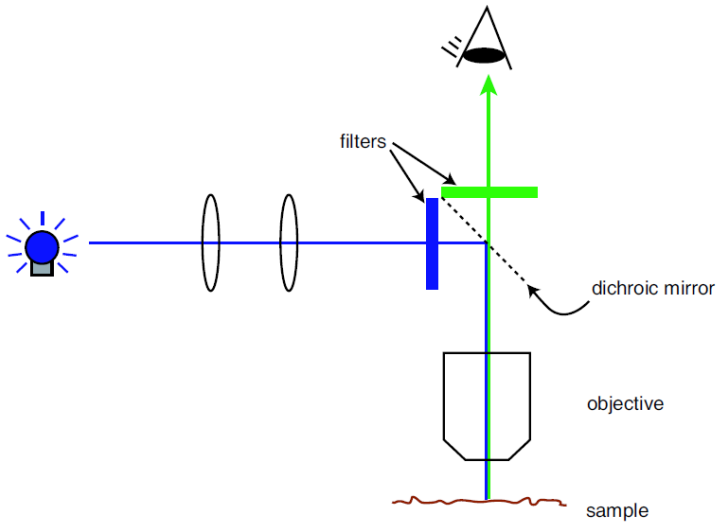

Figure 26. *Basic setup of a fluorescence microscope. Light from the source is reflected off the dichroic mirror toward the specimen. Returning fluorescence of a longer wavelength is allowed to pass through the dichroic mirror to the eyepiece. (View this art in color at www.dekker.com.)*

Fluorescence microscopy is a useful technique to detect the nanoparticles presently functionalized with antibodies and fluorophores, and allows to corroborate the flow cytometry results.

Chapter IV

Materials and Methods

This chapter is divided into three sections. First, materials and methodology used for the synthesis and characterization of europium-activated hydroxyapatite nanoparticles are described. Second, the synthesis and characterization of bismuth germanate nanoparticles are exposed, as well as the analysis of oxidative stress in zebrafish, and medical radiology. Third, the functionalization of both nanoparticles with W6/32 antibodies and leukemia cell recognition are explained.

IV.1 Europium-activated hydroxyapatite (HA:Eu)

IV.1.1 Synthesis of HA:Eu

Europium-doped hydroxyapatite powder was synthesized by a two-step process consisting of the sol-gel technique and subsequent annealing. A mixture containing 1.884 g of high purity $Ca_{10}(PO_4)_6(OH)_2$ (Sigma Aldrich, USA) and 0.116 g of Eu_2O_3 (Sigma Aldrich, USA) was dispersed in distilled water. A 4% HNO_3 solution was added under stirring. Separately, a solution of 5% of tartaric acid (Sigma Aldrich, USA) in distilled water was prepared and mixed with the former solution under stirring. The molar ratio of metal ions to tartaric acid was 1:2 (Taxac *et al*., 2009). The mixture was stirred for 24 h at room temperature with the final pH around 0.5. Then, the mixture was heated to 80°C for 2 h under stirring. Thereafter, the temperature was increased to 120°C and kept at this temperature until the solution became yellow. The material was dried and the resulting brown powder was calcined at 1200°C for 4 h and labeled as HA:Eu. The heating rate employed was 5°C min^{-1}, and after calcination, the same rate was used to cool down the muffle furnace.

IV.1.2 Physical characterization

The powder was analyzed by X-ray diffraction with a Phillips X'pert diffractometer with CuK_α radiation (λ = 0.15406 nm). Measurements in a 2θ = 10-80° range were taken with a step size of 0.1° and 1 sec dwell per point. Transmission electron microscopy (TEM) images were obtained with a JEOL-2010 operated at 200 kV accelerating voltage. Photoluminescence (PL) spectra were collected with a fluorescence spectrophotometer (Hitachi FL-7000). All measurements were performed at room temperature.

IV.1.3 Stability in physiological fluids

The photoluminescence of the HA:Eu nanoparticles in different body fluids was studied by dispersing the particles into human blood serum and urine. The body fluids were donated. One mg of HA:Eu was mixed into 1 mL of blood serum and dispersed in an ultrasonic bath. The urine dispersion was prepared as described above, 1 mg of HA:Eu in 1.5 mL of urine. An HA:Eu suspension was prepared with 1 mg in 1.5 mL of 50 mM cysteine and assayed at pH=1 as an extreme condition. A suspension with 1 mg HA:Eu in 1.5 mL distilled water was used as reference. In order to prove the reproducibility of the experiment, the experiment was repeated several times (10).

IV.1.4 pH stability

The stability of HA:Eu nanoparticles under different pH conditions was assayed in urine, water and blood serum dispersions. The basal pH values for urine, water and blood serum were 7,5 and 7.25, respectively. Extreme pH conditions were only explored for urine and water by adding nitric acid and ammonia solutions, to test stability under acid and basic environments,

respectively. The pH of these fluids was then adjusted to test HA:Eu nanoparticles stability at values 1, 5, 10 and 12 for urine and water.

IV.2 Bismuth germanate (BGO)

IV.2.1 Synthesis of BGO

Bismuth germanate oxide powder was synthesized by sol-gel and subsequent annealing. High purity $Bi_2O_3 \cdot XH_2O$ (4.049 g, Puratronic 99.999%) was mixed with GeO_2 (0.631 g, Alfa Aesar 99.98%) according to stoichiometric calculations and dispersed in a solution of 4% diluted HNO_3 (40 ml). In another flask, 2.58 g of L-tartaric acid (Aldrich, USA) were dissolved in 10 ml of deionized water and the individual solutions were mixed under constant stirring. These were then mixed and stirred for 24 h at room temperature; the resulting solution had pH 0.5. Thereafter, the mixture was heated under constant stirring at 80 °C for 2 h, which made it denser forming the sol. Subsequently, the sol was heated at 120 °C until a gel was produced and dried to form the precursor. The as-synthesized powders were annealed with slow thermal treatment (STT): first, they were heated in air in a muffle furnace, starting gradually from room temperature to 950°C at a rate of 1°C min^{-1}; the powders were maintained at this temperature for 4 h, and finally cooled down at the same rate. In attempt to produce a single phase of bismuth germanate a second annealing was performed maintaining the powders for 1 h at 800°C.

IV.2.2 Physical characterization

X-ray diffraction (XRD) patterns were collected with a Phillips X'pert diffractometer equipped with CuK_α radiation (λ = 0.15406 nm). Measurements in a 2θ = 20-60° range were taken with a step size of 0.1° and a 1 sec dwell per point. Transmission electron microscopy (TEM) images were obtained with a JEOL-2010 operated at 200 kV. Atomic Force Microscopy (AFM) images were obtained with on

XE-BIO microscope of Park Systems. The optical properties of the powders were studied with a fluorescence spectrophotometer (Hitachi FL-7000). A Nicolet 6700 spectrometer with attenuated total reflectance device was used to obtain the infrared spectra with a resolution of 2 cm^{-1} and accumulation of 32 scans. The BGO nanoparticles were characterized by Raman spectroscopy using a Jobin Yvon Horiba LabRam-HR system interfaced with an Olympus BX41 optical microscopy and an Ar laser (Olympus TH4-100, 20 mW at 532 nm) source. The scintillator properties were studied by radioluminescence (RL) measurements obtained by the D08B:XAFS2 beam line at the Brazilian Synchrotron Light Laboratory (LNLS) in Campinas/SP, Brazil, with the X-ray beam tuned at 7 keV. The RL signal was obtained using a spectrometer (Ocean Optics HR2000), and decay time was measured with a PTI GL3000 nitrogen-pulsed laser. The resulting transient fluorescence signal was analyzed with a Jobin-Yvon monochromator Triax 550 and a Horiba-Jobin Yvon i-Spectrum Two ICCD detector. All measurements were performed in air at room temperature.

IV.2.3 Functionalization of nanoparticles

Briefly, a set of BSA protein dilutions ranging from 0-10 $\mu g\ mL^{-1}$ was prepared. For each assay, 800 μL of BSA standard solution were mixed with 200 μL of Bio-Rad reagent and vortexed. Each dilution was then incubated for 5 min at 25°C and absorbance was read at 595 nm and room temperature using a spectrophotometer (Spectronic Genesyss 2, Spectronic Instruments). A protein (bovine serum albumin, BSA) standard curve was obtained, following the microassay indicated by the manufacturer (Bio-Rad, Protein Assay Dye Reagent). To obtain the standard curve, absorbance measurements were plotted against protein concentration.

The BGO functionalization method was standardized as follows. Fifty mg of BGO nanoparticles were mixed with 50 μL of bovine serum albumin (BSA) (8

mg/mL) and 10 μL of 0.1 M 1-ethyl-3-(3-dimethylaminopropyl) carbodiimide (EDC). The EDC is thought to link the protein to the particle surface (Martínez-Ortíz *et.al.,* 2011). The mixtures were completed up to 1 mL with 10 mM Tris-HCl buffer (pH 5.5) to maintain the protein stable and active. The suspensions were incubated at 37°C for 2 h and then centrifuged at 6,000 rpm for 4 min at 4°C. The suspensions of conjugated nanoparticles were washed two times with Tris-HCl buffer and then three times with distilled water, and the supernatant was recovered by centrifugation. Two controls were included, one with uncoated nanoparticles (BGO-EDC) to estimate the possible unspecific adsorption of reagent dye, and another with BGO nanoparticles and BSA protein without EDC as linker (BGO-BSA) to determine if the nanoparticles can be coated with BSA without linker.

IV.2.4 Protein quantification

To corroborate the protein functionalization of BGO, the attached protein was quantified. For protein quantification, 50 mg of coated and uncoated nanoparticles were suspended in 900 μL of distilled water and 100 μL of Bio-Rad reagent were added in a 1.5 mL Eppendorf tube. This amount of reagent dye was calculated to produce 0.5 absorbance (λ=595 nm) units with an excess of protein. After 15 min incubation, all suspensions were centrifuged at 6,000 rpm for 4 min. An aliquot of 500 μL of the supernatant of each suspension was transferred into a separate test tube to which excess BSA protein was then added (36 μL of 8 mg/mL BSA solution), and the unconjugated reagent dye was spectroscopically determined at an excitation wavelength of 595 nm. Absorbance measurements were transformed to BSA protein equivalents (μg/mL) using the standard curve. The amount of protein attached to the nanoparticles was estimated by subtracting the absorbance of the unconjugated reagent from that initially added. Two control determinations were included: the first was prepared by mixing 50 mg of uncoated

nanoparticles with 10 μL of EDC and 890 μL of distilled water; the second contained 50 mg of uncoated nanoparticles in 900 μL of distilled water.

IV.2.5 Stability in physiological fluids

Human urine photoluminescence was studied as described in section VI.1.3. As reference, a suspension with 1 mg BGO in 1.5 mL of distilled water was also prepared.

IV.2.6 pH stability

The stability of BGO nanoparticles under different pH conditions was assessed in urine and water dispersions. The measured pH values for urine and water were 7.2 and 5.7, respectively. Extreme pH conditions for urine and water fluids were explored adding a nitric acid or an ammonia solution to prepare acid and basic environments, respectively.

IV.2.7 Oxidative stress on zebrafish

The oxidative stress assay of the BGO powders and carbon nanotubes (for comparison) was performed by Yusimi Carrillo at the Institute of Biotechnology in Cuernavaca, Morelos as part of her undergraduate thesis (Carrillo, 2012). The method is therefore not described herein, but the results of her experiments are used in the present work and the Discussion includes them, with her permission.

IV.2.8 Medical radiology

One gram of uncoated and BSA-coated BGO powder were irradiated with a Bennett Trex medical (Linear MC150) radiology room, with an energy of 52 kV,

current of 255 mA exposure time of 1.333 s. The photo was captured with a Canon Powershot A3300 Digital Camera.

IV.3 Functionalization

IV.3.1 Nanoparticle functionalization with antibodies

After HA:Eu and BGO nanoparticle functionalization with BSA protein either with or without carbodiimide (EDC) as linker (described in Section III.4.3), the W6/32 monoclonal antibody (mouse IgG2a) that recognizes human HLA I molecules present on nucleated human cells was added at a concentration of 7.5 µg per 50 mg of nanoparticles (Table VI). W6/32 mAb was purified from ascitic fluid following institutional guidelines and provided by Dr. Y. Rosenstein.

***Table VI**. Mixed solution used for antibody functionalization of nanoparticles.*

	NP	NP+BSA	NP+EDC+BSA
Tris-HCl [10 mM] pH 5.5 (µl)	983	923	913
EDC [0.1 M] (µl)	-----	10	10
W6/32 [420 µg/ml] (µl)	17	17	17

Particles were incubated in this solution at 37ºC for 2 h. Primary antibody-functionalized nanoparticles were washed three times with 100 mM Tris-HCl buffer pH 7.4. Particles were centrifuged and the supernatant was recovered to determine the efficiency of MAb binding to the nanoparticles. Thereafter, the nanoparticles were resuspended in 500 µl of FACS solution (PBS pH 7.4, 2% fetal calf serum, 0.01% NaN_3 and incubated for 30 min at room temperature with a fluorophore-conjugated secondary antibody (goat-anti mouse IgG coupled with Alexa 488

(Invitrogen Co.), which is excited at 488 nm and emits at 519 nm. After this period, samples were washed with FACS solution and centrifuged at 1200 rpm (400g) for 5 min at room temperature. Subsequently, samples were analyzed via flow cytometry with a FACSCanto II cytometer and the DIVA software (BD Biosciences). Antibody-functionalized nanoparticles with no secondary antibody and nanoparticles without W6/32 but incubated with the secondary antibodiy only were used as controls. Data were analyzed with the FlowJo flow cytometry analysis software.

IV.3.2 Cellular recognition (targeting)

To assess the capacity of the antibody–loaded nanoparticles to recognize the cognate antigen (HLA I) of the W6/32 mAb on human cells, the acute monocytic leukemia cell line THP-1 [HLA I^+: A2, A9; B5] (ATCC TIB-202), was incubated with the particles at 1:20 cell: particle ratio for 2 h at 37 ºC in 5% CO_2. This mAb recognizes a public epitope present on all HLA I molecules (Parham P, et al., 1979). Controls included THP-1 cells, mAb loaded-nanoparticles and THP-1 cells with non-functionalized nanoparticles. A488 labeled anti-mouse IgG was used as secondary antibody as described for visualization of mAb binding to the nanoparticles surface. Samples were fixed with 4% paraformaldehyde prior to epifluorescence and flow cytometry measurements.

Chapter V

Results and Discussion

Results on the structure and luminescence characterization of europium-activated hydroxyapatite are discussed in section V.1 as well as the optical stability in different body fluids and pH conditions. Section V.2 presents and comments on the structural characterization and optical stability results in different body fluids at different pH conditions. Finally, section V.3. presents and discusses BGO functionalization with BSA protein, the oxidative stress of BGO nanoparticles and the functionalization of BGO and HA:Eu nanoparticles with W6/32 antibodies and their capacity to identify the antigen on the surface of leukemia human cells.

V.1 HA:Eu

V.1.1 Structural characterization

The X-ray diffraction patterns of the HA:Eu powder annealed at two different temperatures are shown in Figure 27. No significant difference was found between the samples annealed at 1000 and 1200 °C; the sample used in this investigation was the HA:Eu powder annealed at 1200°C. The X-ray diffraction pattern of this sample matches the profile of hydroxyapatite and β-tricalcium phosphate ($Ca_3(PO_4)_2$, JCPDS card file No.55-0898) phases. The HA structure is hexagonal with the space group P63/m (JCPDS card file No. 09-0432); this structure constitutes the main component of the powders, approximately 70 vol%.

The β-tricalcium phosphate phase is commonly found when HA is annealed at temperatures higher than 800°C (Bohner, 2000). The phosphate groups show affinity to bind to organic linkers such as carbodiimide (EDC). For example, EDC is

used to activate phosphate groups, and it links to peptides and proteins. Thus, the second phase is important because it provides phosphate groups and makes the functionalization with organic molecules more probable.

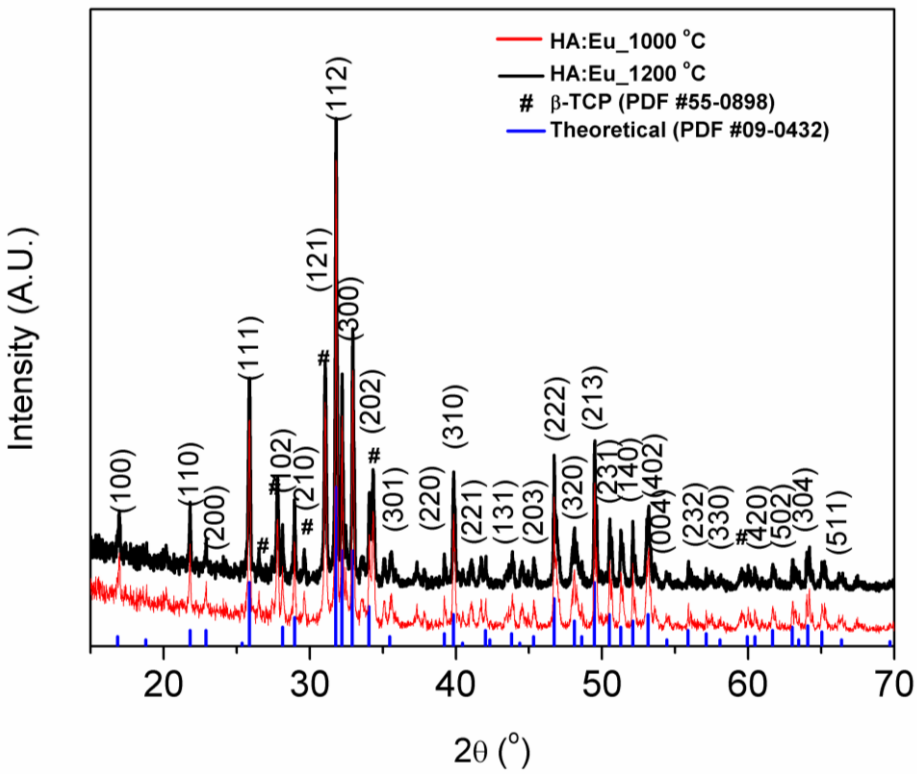

Figure 27. *X-ray diffraction powder pattern of $Ca_{10}(PO_4)_6(OH)_2$:Eu^{3+} powders produced by sol-gel and annealed at 1000 and 1200°C for 4h.*

Figures 28 (a) and (b) show typical TEM images of the annealed powders . The nanoparticles have regular shape and narrow size distribution (15 – 100 nm). The high-resolution image (Figure 29) shows the plane (1 0 0) with a spacing of 0.82 and the plane (1 0 1) with 0.55 nm of spacing along [0 0 $\bar{1}$] zone axis. The angle between the planes (1 0 0) and (1 0 1) was calculated and is 49.85° and confirms the presence of the hexagonal HA.

The particles size obtained in this experiment is convenient for biomedical applications such as biomarkers, because these require that nanoparticles can flow

along the circulatory system, and the circulatory system is formed by arteries, veins and capillaries, where the lowest diameters are 4-6 μm (Sharifian, 2003).

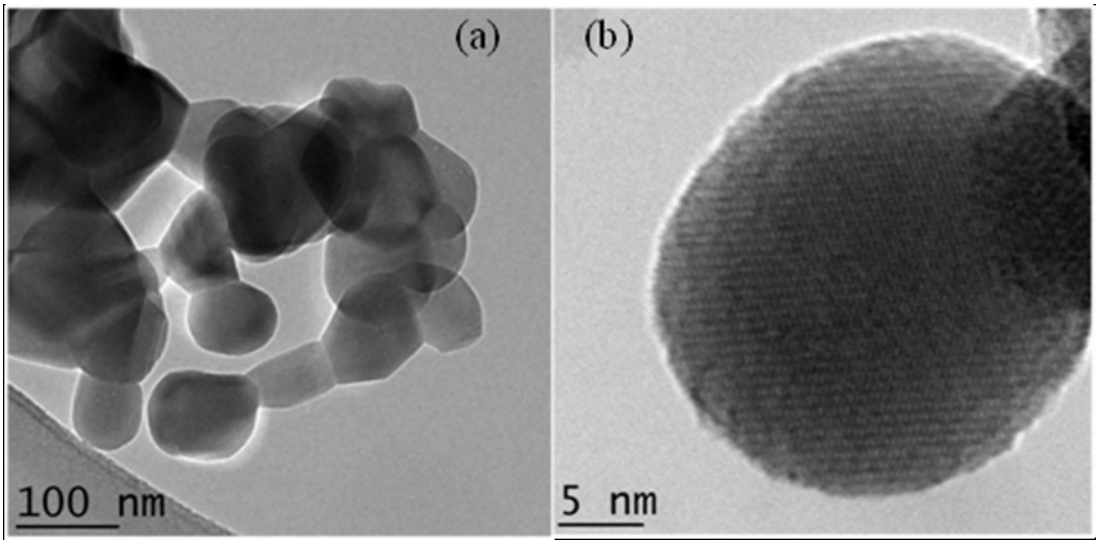

Figure 28. *TEM images of $Ca_{10}(PO_4)_6(OH)_2$:Eu^{3+} nanoparticles.*

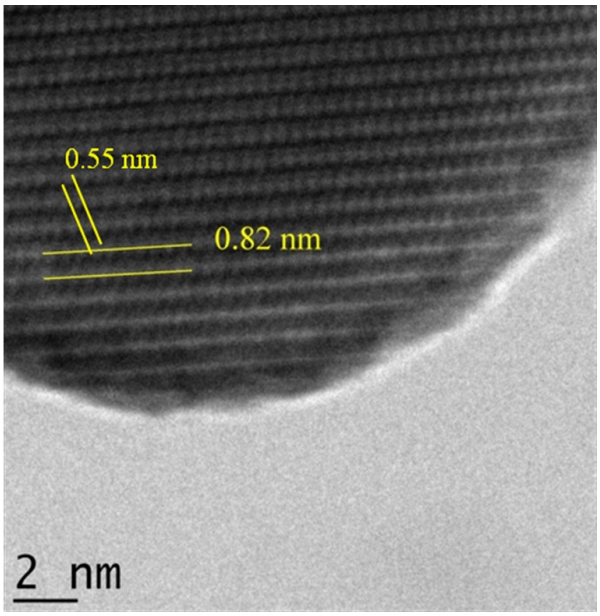

Figure 29. *High resolution TEM showing the planes separated by 0.82 nm and 0.55 nm.*

V.1.2 Photoluminescence in different fluids

In the human body, numerous waste compounds are generated by cellular metabolism. Many are rich in nitrogen and are filtered by the kidneys from the bloodstream, and eliminated as urine. Urine contains a range of substances that vary according with the type of compound/nutrients consumed. Aside from water, urine contains an assortment of inorganic salts and organic compounds, including urea: $(NH_2)_2CO$, proteins, hormones, and a wide range of metabolites (Adachi *et.al.,* 2006).

Since pH in the human body can change with some diseases, urine is a desirable medium for diagnosis and classification of diseases because it is easy to collect samples in large amounts and with a diversity of molecules. Urine is a key medium to analyze since its composition depends on effects in proximal organs, such as kidney failure resulting from high blood pressure and diabetic nephropathy, which is the most frequent cause of renal failure (Locatelli, 2003). Blood serum is another such revealing body fluid.

The stability of HA:Eu nanoparticles in urine at different pH values was therefore studied.

Figure 30 shows the excitation spectrum of the HA:Eu powder, and two maximum peaks are observed centered at 280 nm and 394 nm. The 394 nm peak was selected as excitation wavelength owing to two reasons; first, because it is located in the violet region which is less harmful than UV, and, second, because it exhibits the highest intensity. PL spectra were obtained using an excitation wavelength of 394 nm from samples dispersed in different biological fluids: urine (pH = 7), blood serum (pH = 7.25) and a cysteine solution (pH = 1), which were compared with the powder dispersed in water (pH = 7) and air (Figure 31). The PL emission spectral peaks correspond to the typical $^5D_0 \rightarrow {}^7F_j$ emissions attributed to Eu^{3+} in apatites. The HA structure has two types of Ca sites: Ca(I) with C_3 symmetry surrounded by nine oxygen atoms, and Ca(II) with C_s symmetry surrounded by six oxygen atoms and one OH^- ion (Jagannathan and Kottaisamy,

1995; Knubovets, 1993, Kottaisamy *et al.*, 1994). Martin et al. showed by time-resolved laser-induced fluorescence measurements that the Eu^{3+} substitutes the Ca^{2+} ions at both the Ca(I) and Ca(II) sites. The emission bands centered at 575 and 590 nm correspond to the $^5D_0 \rightarrow ^7F_0$ and $^5D_0 \rightarrow ^7F_1$ transitions of Eu^{3+} in the Ca(II) sites, respectively. The two peaks positioned at 620 nm and 626 nm are the transitions $^5D_0 \rightarrow ^7F_2$ of Eu^{3+} at the Ca(I) sites. The single PL emission peak at 613 nm observed only in the cysteine solution corresponds to the same transition $^5D_0 \rightarrow ^7F_2$ of Eu^{3+}; a possible explanation is that both the cysteine molecule and the fluid absorb in the range of 575-600 nm.

The relative intensities of the PL emission spectrum changed depending on the fluid. The change in intensity was most pronounced with cysteine, suggesting a possible complexation of the europium ion at the Ca(II) sites with cysteine, thereby quenching the $^5D_0 \rightarrow ^7F_0$ emission and affecting the other $^5D_0 \rightarrow ^7F_2$ emission peaks. The differences in the emission spectra obtained for urine and serum dispersions compared with water could be due to the change in particle surface structure caused by substitution of phosphate ions (around Eu^{3+}) by the serum or urine ligands. However, the most important observation is that Eu^{3+} emissions still occur in the different fluids.

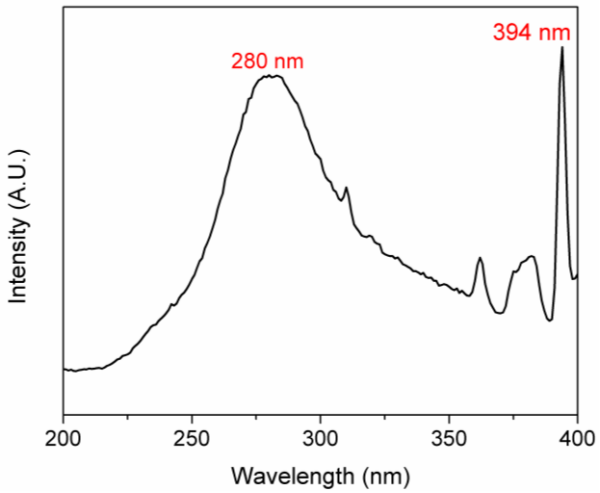

Figure 30. *Excitation spectrum of HA:Eu powders.*

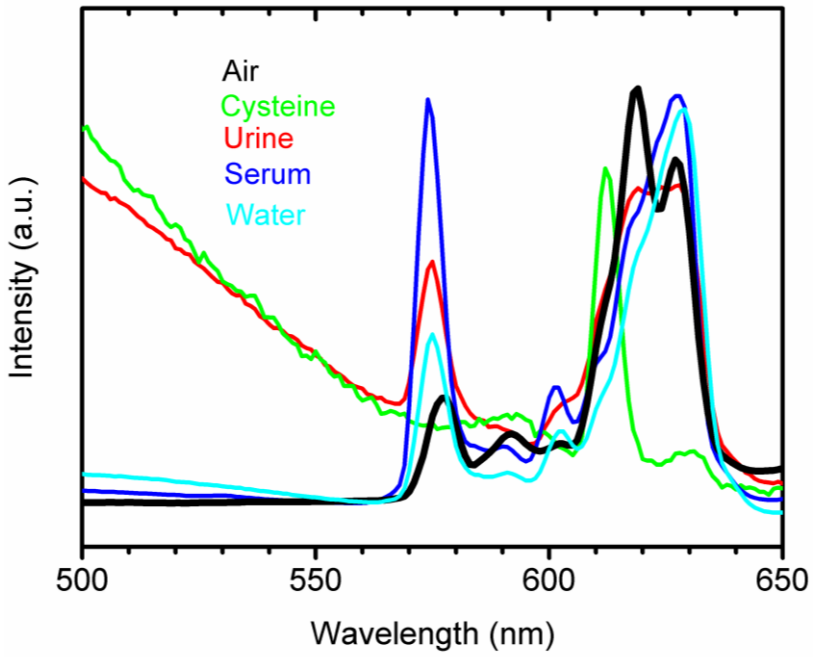

Figure 31. *Photoluminescence spectra of the HAp:Eu powder in different solutions: urine (red), cysteine (green), blood serum (blue), air (black) and water (cyan).* λ_{ex}*= 394 nm.*

V.1.3 Photoluminescence at different pH values

Figure 32 shows the PL spectra normalized with the 617 nm peak for the nanoparticles dispersed in distilled water with different pH values. A PL spectrum obtained from HA:Eu in air is also included. There is a slight difference in the profile of the PL peaks observed in the region of 613-630 nm for powder dispersions in water compared with the curve for powder dispersed in air; this slight difference could be an effect of absorption by the distilled water. However, there is no significant change in the PL spectrum of all dispersions in a pH range from acid to basic. A small reduction in total PL intensity was observed in dispersions with pH value which differ from neutral. Only in an extremely acidic solution (pH=1) did the PL emission fall to zero; one reason for this could be that the HA:Eu particles are completely dissolved in this aggressive environment.

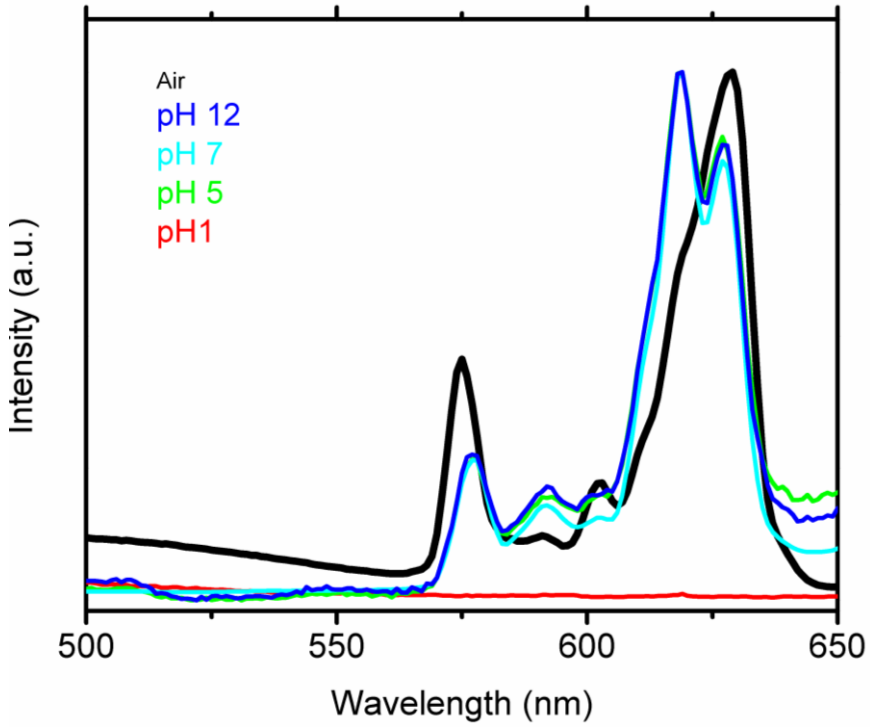

Figure 32. *Photoluminescence spectra of the HA:Eu powder dispersed in distilled water at different pH concentrations: pH 1 (red), pH 5 (green), pH 7 (black) and pH 12 (blue).*

PL spectra of powders dispersed in human urine with different pH values are presented in Figure 33. Urine from healthy human bodies (pH=7) has an intrinsic broadband emission in the range from 450 to 630 nm. The intrinsic broadband can be the emission of all organic molecules present in urine.

HA:Eu powder dispersions in urine showed the same emission peaks as observed for powders in air, but mounted over the urine emission.

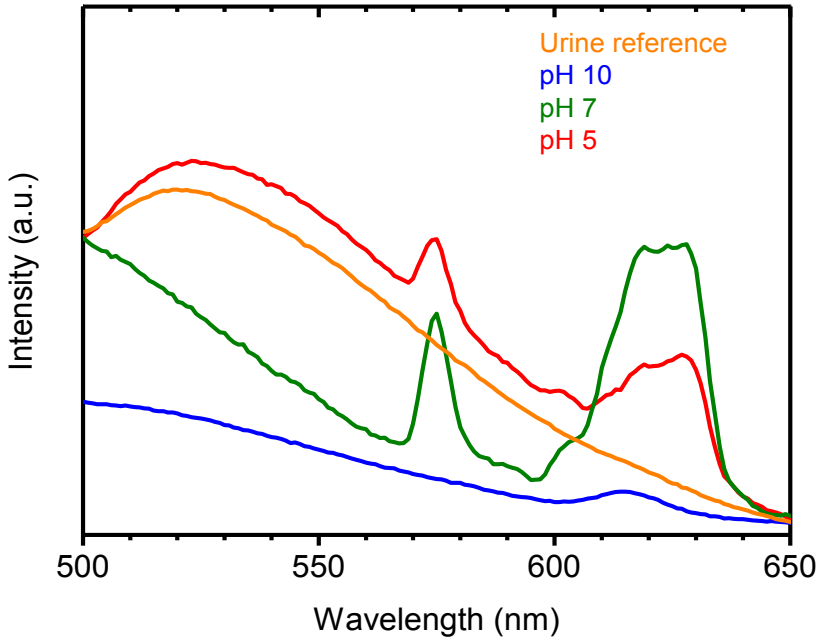

Figure 33. *Photoluminescence spectra of the HA:Eu powder dispersed in urine with different pH values: pH 5 (red line), ph 7 (black line) and pH 10 (blue line) and in air. Pure urine (without HA:Eu) is indicated in orange as a reference.*

HA:Eu powder dispersions in urine without pH alteration produced a uniform emission in the 610-630 nm range. Under highly alkaline conditions, powder and urine emissions strongly diminished, and for the HA:Eu powder almost vanished. Acid (pH 5) dispersions presented, a well identifiable powder emission although of less intensity. Eu^{3+} ion emissions still occur and are detectable, either immersed in urine or water at pH values between 5 and 12 (in water).

The stability of HA:Eu nanoparticles under different pH conditions was then tested and confirmed. In order to confirm the experiment reproducibility, Figure 34 shows measurements conducted on the first day of preparation and 10 days later for each pH value. A very similar behavior was observed on both days.

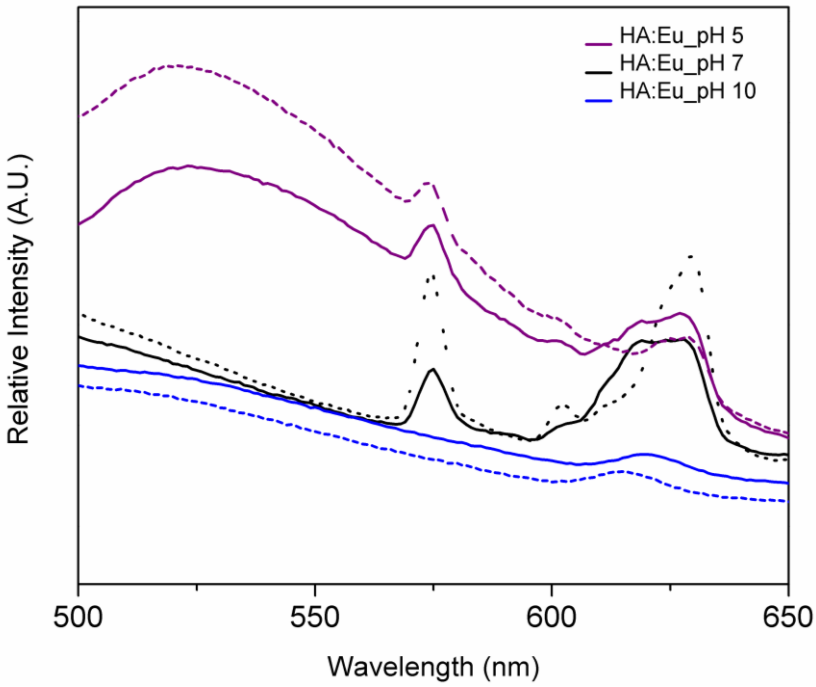

Figure 34. *Emission spectra of HA:Eu powders at different pH values measured on day 1 (solid line) and 10 days after solution preparation (dashed line).*

The photoluminescent emission between the 610-630 nm of HA:Eu nanoparticles (excited with λ=394 nm) may be used to mark cells or tissues. The biocompatibility of HA:Eu nanoparticles reduce the risk of potential toxic effects (Hamlekhan *et al.*, 2010). The excitation energy used in the current experiments is lower than the excitation energy of QD's (λ=254 nm). In addition, these HA:Eu nanoparticles can be chemically functionalized with the appropriate targeting ligands such as carbodiimide, antibodies, or proteins, which confer to them specific affinity for the cell wall or receptors of tumor cells (Cai *et al.*, 2006).

V.2 BGO

V.2.1 Structural characterization

X-ray diffraction patterns of BGO powders produced by sol gel after the annealing process (slow thermal treatment, STT) are shown in Figure 35. The diffraction peaks of the samples which were annealed at 850°C and 900°C were

indexed in agreement with the JCPDS Cards No. 340416 for cubic $Bi_4Ge_3O_{12}$, 270050 for β-Bi_2O_3 and 771641 for Bi_2GeO_5. These different phases were obtained because the thermal treatment was close to the eutectic point as previously explained in Figure 10. To obtain a pure $Bi_4Ge_3O_{12}$ phase the sample was annealed twice, first at 950°C then at 800°C. The second annealing was enough to obtain a single phase, which crystallized in the typical body-centered cubic structure of $Bi_4Ge_3O_{12}$ with a group space $I\bar{4}3d$. Excellent crystallinity of the powders was confirmed from the high signal/noise ratio of the diffraction patterns.

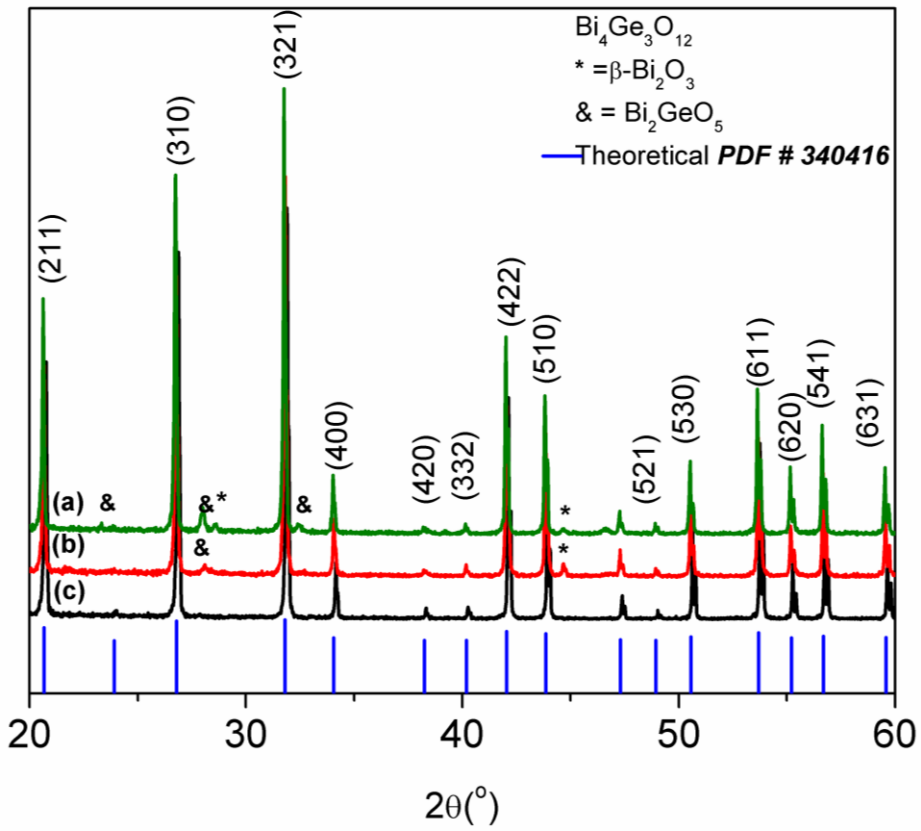

Figure 35. *XRD pattern of $Bi_4Ge_3O_{12}$ phosphor powders produced by sol gel followed by annealing process, (a) 840* °C, (b) 900 °C and (c) 950 °C and 800 °C

Transmission electron microscopy analysis confirmed the crystal structure and revealed the morphology of the nanocrystals. Figure 36 shows representative TEM images of the powders. The inset of Figure 36, shows a high-resolution (HR)

TEM image of the BGO cubic structure observed along the [$\bar{1}$ 3 $\bar{3}$] zone axis. The nanoparticles have a spherical shape and a size distribution of around 10 nm. The image shows the (3 2 1) and (3 1 0) planes with 0.32 and 0.28 nm of spacing, respectively, and an angle between them of 21.62 °. TEM corroborated the results obtained by XRD and confirmed the presence of the cubic BGO. To the best of our knowledge this is the first time that BGO nanoparticles have been synthesized with a size lower than 500 nm (De Jesus *et.al.* 2009).

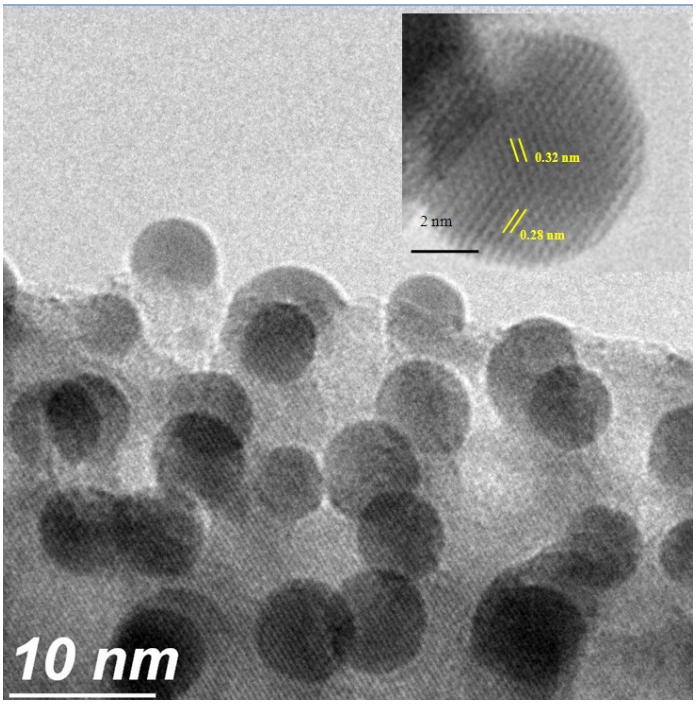

Figure 36. *TEM image showing nanocrystalline particles of BGO synthesized by sol gel followed by an annealed.*

V.2.2 Optical properties

The photoluminescence spectra (excitation and emission) of the sample are shown in Figure 37. The excitation spectra determined the wavelength of maximum emission of the phosphor material. The maximum relative intensity values of the

excitation peaks are centered at 250 and 280 nm, near the band gap edge of the BGO crystals (Polosan, 2010). The BGO sample yielded blueish-white luminescence when excited with UV photons, thus presenting a broadband emission in the visible region, where the maximum peak was centered at 485 nm, associated with the $^3P_1 \rightarrow {}^1S_0$ of Bi^{3+} electron transition. Photoluminescence properties of single crystal BGO have been reported (de Jesus *et.al.*, 2010) and a typical PL spectrum is included in Figure 36 for comparison. The emission band of the BGO powder at 485 nm is similar to the single crystal emission peak.

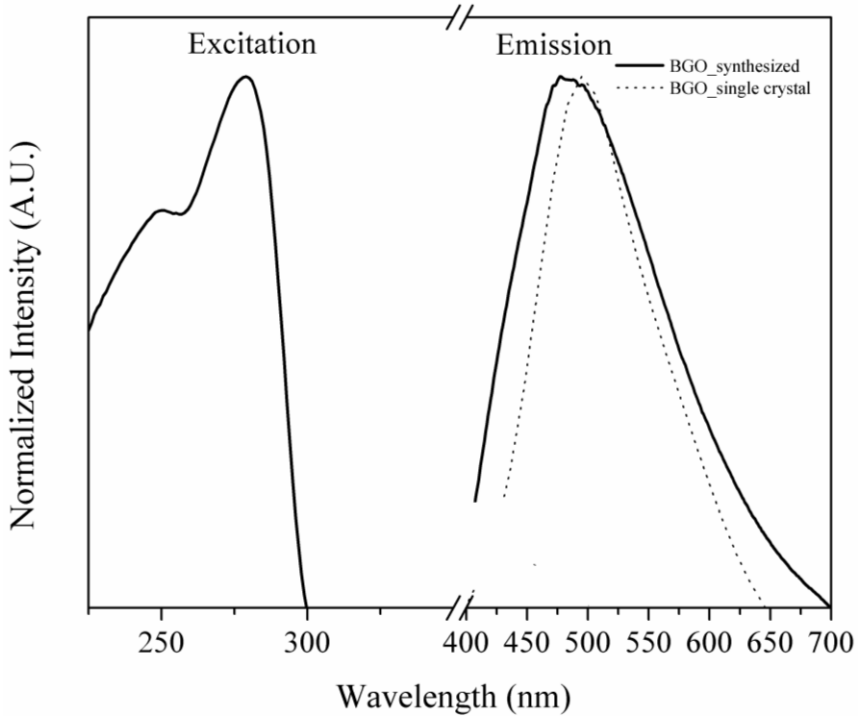

Figure 37. *Photoluminescence spectra of BGO nanoparticles. The PL spectrum of the single crystal BGO (de Jesus et al., 2010) shows similar broadband emission.*

The two excitation peaks detected by PL at 250 and 284 nm are ascribed to $^1S_0 \rightarrow {}^3P_1$ and $^1S_0 \rightarrow {}^1P_1$, respectively. The $^3P_0$ state is the lowest excited state of Bi^{3+}, however, $^3P_0 \rightarrow {}^1S_0$ emission is forbidden. Since the $^3P_0$ level is situated below the $^3P_1$ level, at low temperatures the $^3P_0 \rightarrow {}^1S_0$ occurs, while at higher temperatures

(room temperature) the practically allowed $^3P_1 \rightarrow {}^1S_0$ emission takes over (Boulon et al,). Hence, the observed emission of Bi^{3+} originates from the thermal population of the $^3P_1$ level and the $^3P_1 \rightarrow {}^1S_0$ electronic transitions. Weber *et al.*, (Weber, 1975) estimated the radiative decay rate from the levels $^3P_1$ and $^3P_0$ integrating the absorption cross-section and the Einstein A-B relationship. Decay time for $^3P_0$ is longer than for $^3P_1$. If $^3P_1$ levels are within a few *KT* (*K*: Boltzman constant and *T*: temperature) of $^3P_0$, lifetime shortening of the latter due to increased radiative decay may be anticipated.

In order to characterize and identify if the synthesized BGO nanoparticles possess similar or identical properties (radioluminescence and short decay time) to those for single BGO crystal, radioluminescence and decay time experiments were performed. The radioluminescence experiment revealed a single emission peak centered at 500 nm (Figure 38). For comparison, the RL curve reported for the single crystal BGO under X-ray excitation is also included in Figure 38 (de Jesus *et.al.*, 2010). In both luminescence experiments, the emission peaks derives from the $^3P_1 \rightarrow {}^1S_0$ electron transition in the Bi^{3+} ions (Weber *et. al.,* 1973). Figure 39 shows the luminescence decay curve of the emission at 485 nm eV under 280 nm excitation. According to the decay time theory (section III.1.5) an exponential fit was applied to determine the decay time which was 294 ns. Decay time of single crystal BGO is 300 ns as reported by Blasse and Grabmaier (1994); the decay time obtained in this work was quite similar.

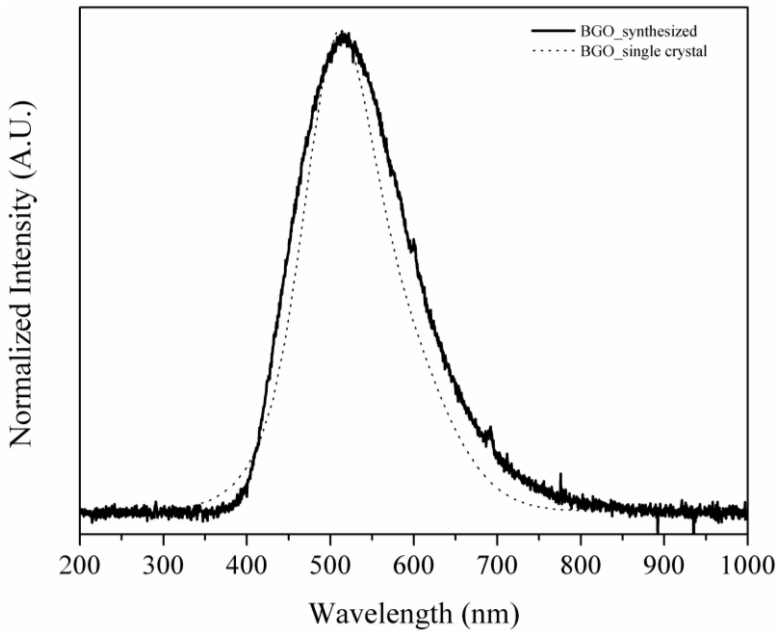

Figure 38. *RL spectra of $Bi_4Ge_3O_{12}$ synthesized by sol-gel and annealed by STT. RL spectra of single crystal BGO (de Jesus et al., 2010) shows a highly similar emission peak.*

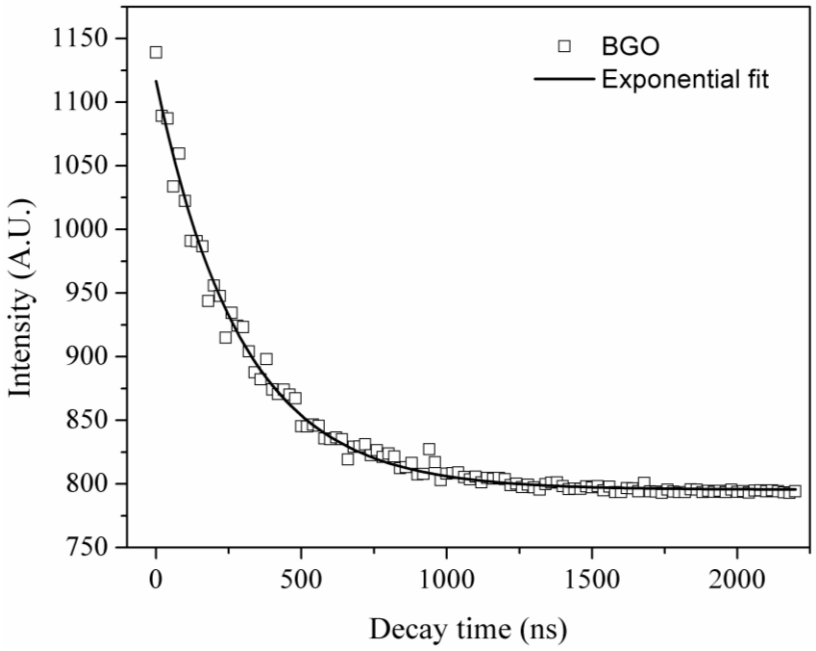

Figure 39. *Plot of photoluminescence intensity as a function of time of $Bi_4Ge_3O_{12}$ nanoparticles under 280 nm excitation.*

PL, RL and decay time experiments of BGO nanoparticles presented quite similar optical properties to the single crystal BGO, making them promising candidates for scintillation applications. For example, BGO is generally used in the single crystal form for high energy detectors in medical equipments such as PET and MRI. However, is difficult to produce a single crystals, while the BGO powders produced in this work are easily to be obtained, and could be an alternative to replace the single crystal detectors.

V.2.3 Functionalization of BGO nanoparticles with BSA protein

Figure 40 displays the standard absorbance curve obtained using BSA as protein standard reacted with the Coomassie blue dye. A linear response was obtained when absorbance was plotted at 595 nm *vs* protein concentration. The following equation presents the linear behavior of the standard curve as well as the Chi square (r^2) of the linear fit.

$$[protein]\ (\mu g\ mL^{-1}) = 13.23\ (Abs_{595}) \qquad r^2 = 0.989 \qquad (12)$$

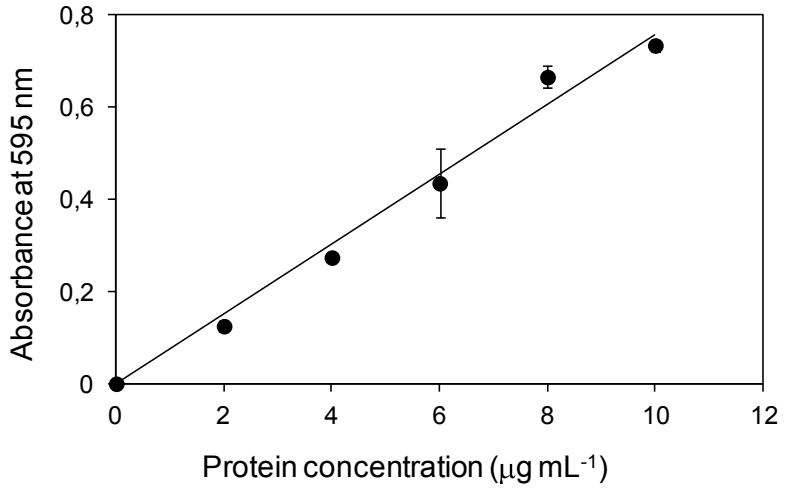

Figure 40. *Standard absorbance curve of Bio-Rad protein reagent (coomassie blue) with bovine serum albumin (BSA).*

The conjugated protein determination showed a value of 134.9 ±62.3 μg protein/g BGO, the control experiments of all nanoparticles (BGO-EDC-BSA; BGO-BSA; BGO-EDC; BGO) showed no Coomassie blue adsorption (Figure 41).

The Bio-Rad Protein Assay is a dye-binding assay in which a color change occurs in response to protein concentration. The Coomassie blue binds to basic and aromatic amino acid residues, especially arginine (Compton *et. al.,*1985), displaying a color change in response to protein concentration. A color shift from 465 nm to 595 nm occurred in the presence of proteins, suggesting that the BSA protein can be attached to the surface of the nanoparticles.

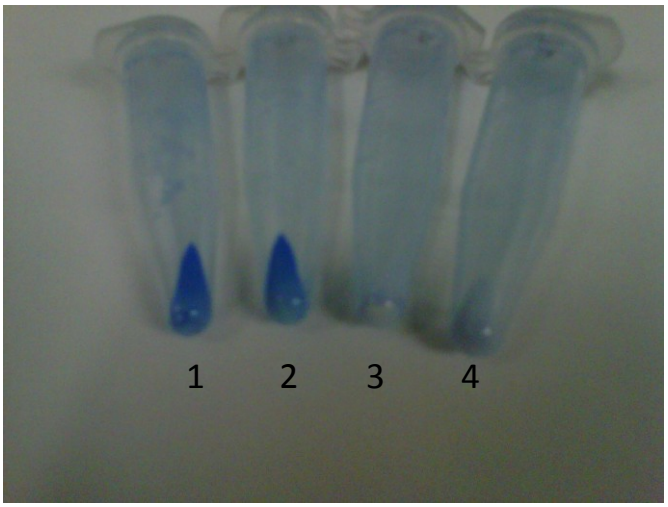

Figure 41. *BGO nanoparticle preparations after protein reagent treatment and later centrifugation. 1) BGO nanoparticles treated with BSA in the presence of EDC in 10 mM Tris HCL. 2) BGO nanoparticles treated with BSA in the absence of EDC in 10 mM Tris HCL. 3) BGO nanoparticles treated with EDC and without BSA in 10 mM Tris HCL. 4) BGO nanoparticles in 10 mM Tris HCL without BSA and EDC.*

Figure 42 shows AFM images of the powders with and without BSA functionalization. Particles were observed of regular shape and narrow size distribution with an average particle size between 8-40 nm for uncoated particles and 50-90 nm for coated particles.

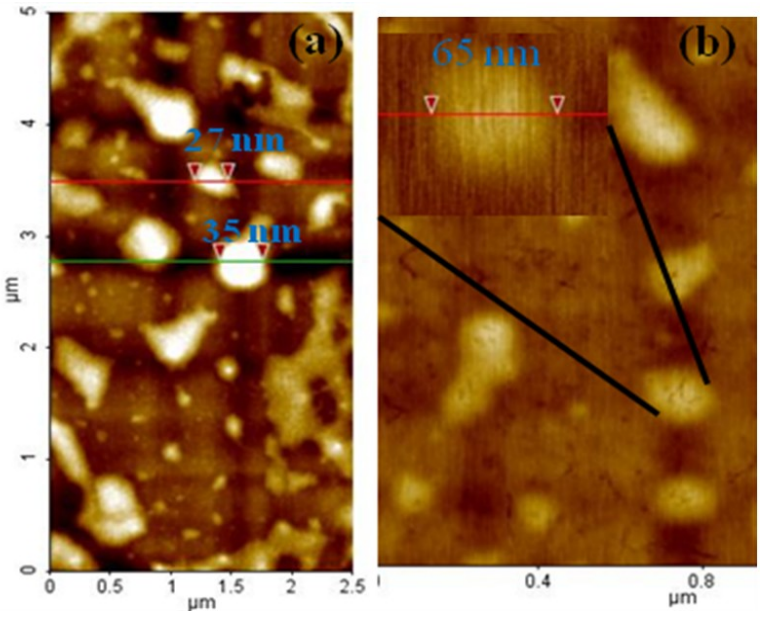

Figure 42. *AFM image of BGO nanoparticles. The red and green lines are the AFM section analysis that show a nanoparticle size between (a) 27-35 nm before, and 65 nm after BSA functionalization.*

To identify the amino groups that characterize the EDC and BSA organic molecules, infrared and Raman spectroscopy were conducted. The infrared spectrum of uncoated BGO shows intense bands of Bi-O and Ge-O (Beneventi *et. al.,* 1996; Rojas *et. al.,* 2010; Yu *et. al.,* 2011) moieties in the low wavenumber region, as shown in Figure 43. The NH_2 functional groups that characterize proteins show specific peaks between 1500 and 2000 cm^{-1}. After the BGO functionalization with BSA, the powder showed bands of O-H and N-H vibrational modes, which reveal the presence of water and amino acid molecules. The wide band around 3300 cm^{-1} results from hydrogen bonds at different degrees involving water or amino groups, thus widening the range of vibrational frequencies. The bending mode of amino groups at 1650 cm^{-1} (Nakamoto *et. al.,* 2009) clearly confirms the presence of BSA and no changes were detected in BGO vibrations at 1095, 857, 780 and 480 cm^{-1}. Thus, the molecular integrity of BGO was maintained in the functionalized BGO particles, which is needed to preserve the light emission properties of BGO.

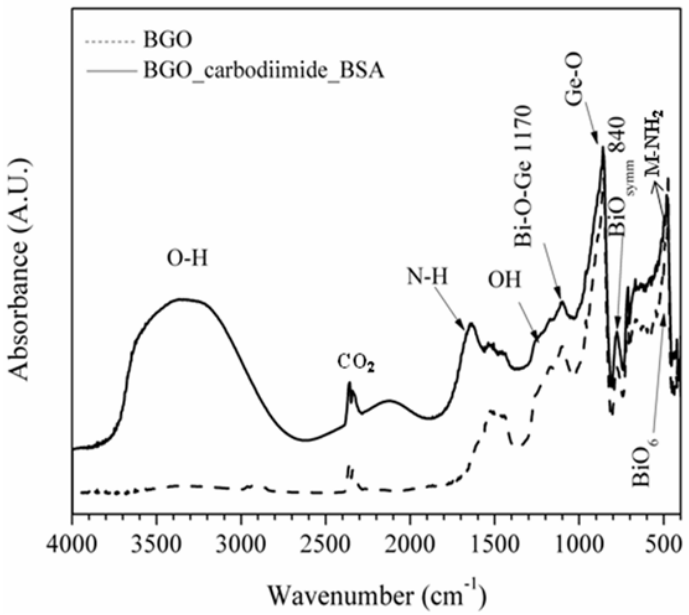

Figure 43. *Infrared spectra of BGO nanoparticles before (dash line) and after BSA functionalization (solid line).*

Raman analyses conducted on BGO particles showed a typical profile (Figure 44) formed by lattice vibrations below 300 cm^{-1} and Bi-O or Ge-O fractions up to 730 cm^{-1}, as reported elsewhere (Benevent *et. al.,* 1994; Rojas *et. al.,* 2010; Cho *et. al.,* 2001). A band of low intensity at 530 cm^{-1} is detected in the spectra of samples treated with EDC and BSA; it has higher intensity in the EDC-BSA treated sample, which can be assigned to the amino groups of the protein chains, since the amino groups linked to metal centers present a skeletal bending mode between 550 and 250 cm^{-1} (Nakamoto *et. al.,* 2009). This signal can be considered as preliminary evidence suggesting the linking of the proteins to the BGO particles through amino groups. This vibrational mode is confirmed with shoulder observed in the FTIR spectrum of the BGO-EDC-BSA sample near 550 cm^{-1}.

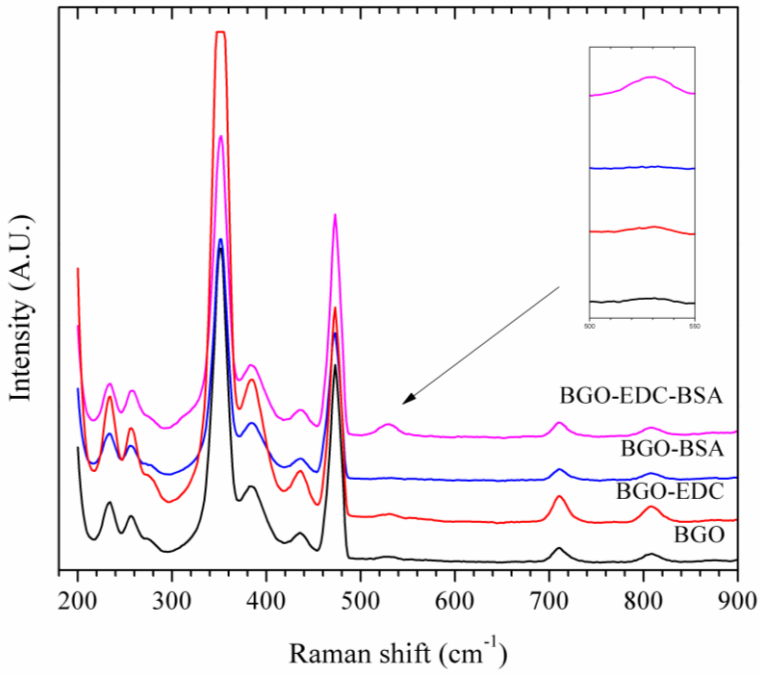

Figure 44. *Raman analysis of BGO at different stages of BSA functionalization.*

V.2.4 Photoluminescence in different fluids

In order to prove if BGO powders can function as synthetic biomarkers, it must firstly be tested if the luminescence of nanoparticles is detectable in different chemical environments such as serum, urine, water and air. PL spectra were obtained from samples immersed in different organic fluids: urine (pH = 7.2), blood serum (pH = 7.28) and carbodiimide-BSA solution (pH = 5.5), and were compared with the powder dispersed in water (pH = 5.7) (Figure 45). The PL emission peak at 485 nm corresponds to the typical $^3P_1 \rightarrow {}^1S_0$ emission attributed to Bi^{3+}. The relative intensity of the PL emission spectrum did not change depending on the fluid; in the case of serum it was slightly shifted. This slight shift in the emission spectrum of blood serum may be because the molecules in serum such as proteins, lipids, antibodies and antigens absorb in the region from 425 to 475 nm, as shown in Figure 46.

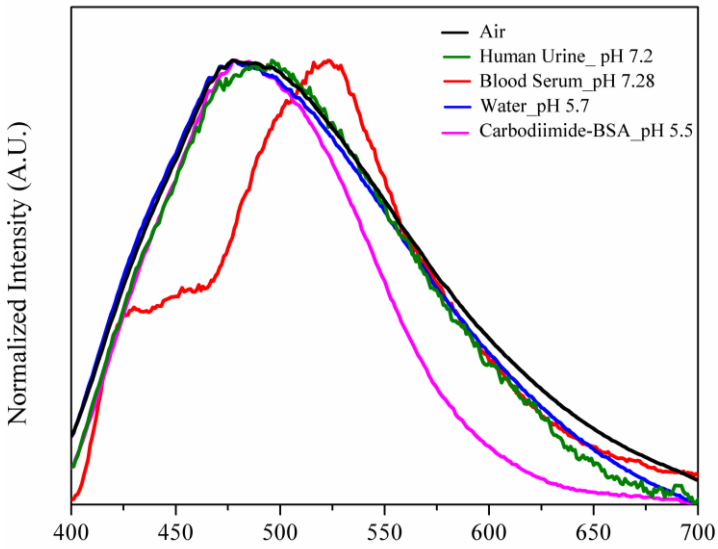

Figure 45. Photoluminescence spectra of the BGO powder in different fluids: human urine (green), blood serum (red), water (blue), BSA protein (pink) and air (black). λ_{ex}=280 nm.

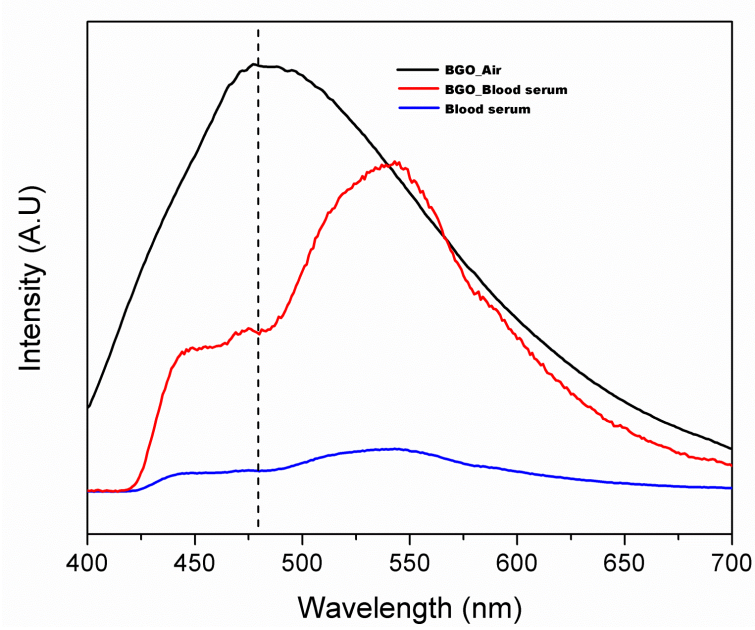

Figure 46. *Emission spectra of BGO powders in air (black), BGO with blood serum (red) and blood serum (blue).*

V.2.5 Photoluminescence at different pH values

Figure 47 shows the intensity of PL spectra for the nanoparticles dispersed in distilled water at different pH values. A PL spectrum obtained from the nanoparticles in air is also included. The photoluminescence diminished in all dispersed solutions probably due to the light absorption of the media, and the chemical environment may perhaps degrade the nanoparticles. Nonetheless, under extreme acid conditions (pH= 5.7 and 1) PL emission of BGO nanoparticles still occurs, in contrast with HA:Eu nanoparticles, in which, under acid conditions (pH=1) luminescence falls to zero. This resistance against acid pH opens the possibility of using the BGO nanoparticles for biological applications.

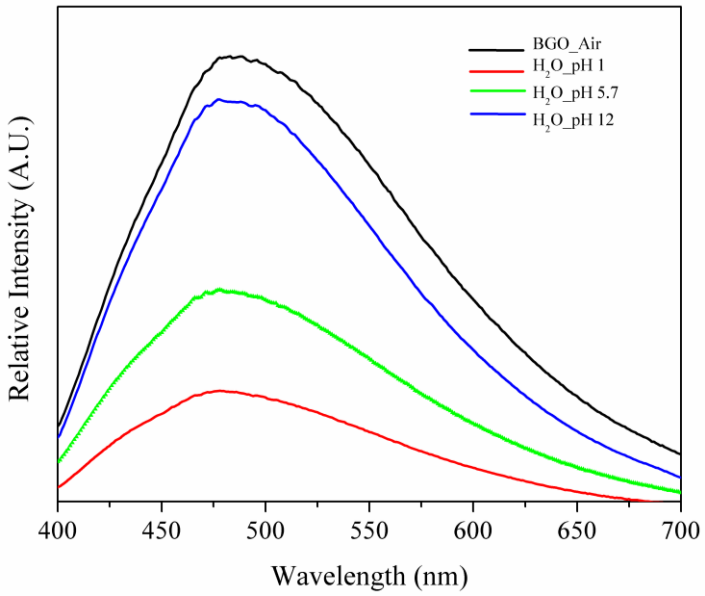

Figure 47. *PL emission spectra of BGO nanoparticles dispersed in distilled water with different pH values: pH 1(red), pH 5.7 (green) and pH 12 (blue). Emission spectrum in air (without fluid) was included for comparison (black).* λ_{ex}*=280 nm.*

PL spectra of BGO powders dispersed in human urine with different pH values are shown in Figure 48. Urine from healthy human bodies (pH=7.2) presented an intrinsic broadband emission in the range from 425 to 700 nm.

Powder dispersions in urine showed the same emission peaks as observed for BGO powders in air, but the spectra displayed noise owing to the broadband of human urine. All emission peaks were at 485 nm as in the water solution. BGO in acid (pH 1) dispersion was less intense than in alkaline dispersions. BGO powders were stable either immersed in urine or water for pH values between 1 to 12.

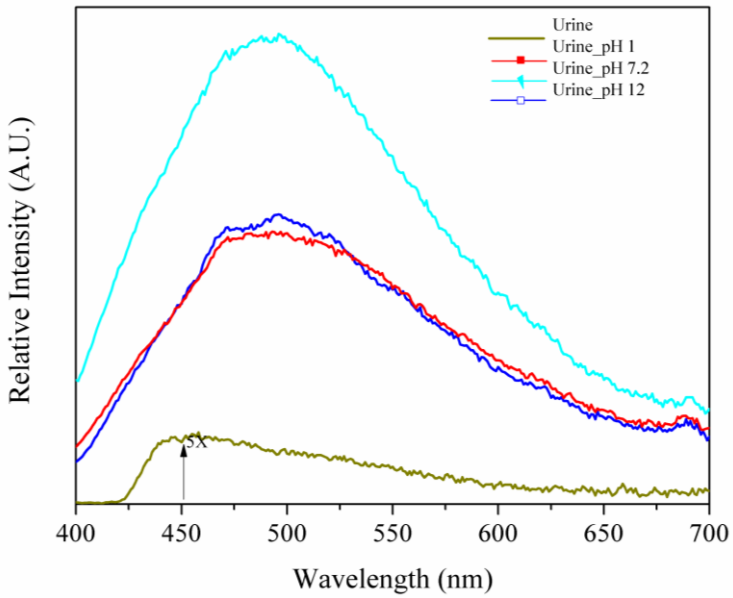

Figure 48. *PL emission spectra of BGO powder dispersed in human urine with different pH values: pH 1 (red curve), pH 7.2 (cyan curve) and pH 12 (blue curve). Pure human urine (without BGO) is indicated in olive as a reference.* λ_{ex}*=280 nm.*

Urine, blood serum and cerebrospinal fluid are convenient for cancer diagnosis because they can be easily obtained and contain significant information such as antibodies, antigens and pH.

On the other hand, gastrointestinal cancer alters the pH profile in humans, which initiates extremely acidic in the stomach at pH of 1-2.5, then in the small intestine it increases to pH 6.6 and finalizes at pH 7.0 in the colon (Evans *et. al.,* 1988; McColl *et.a.,*1998; Correa and Schneider, 2005). Thus, the BGO nanoparticles are an excellent candidate for biomedical applications as biomarkers because they are stable in the pH range from 1 to 12 preserving their

luminescence properties. Additionally, the small size of the particles would facilitate their flow through the body.

V.2.6 Oxidative stress assay

The biomedical application of BGO nanoparticles requires toxicity studies because the nanoparticles will be put in contact with living cells. The capacity of reactive oxygen species (ROS) to modify the proteins has been the subject of extensive research for some years (Stadtman and Oliver, 2005). Proteins, and also other major constituents of membranes, are targets for ROS attack and this damage is known as oxidative stress (Davies, 1987). Proteins can undergo direct or indirect damage following interaction with ROS, including peroxidation, damage to specific amino-acid residues, degradation and fragmentation. The consequences of protein damage as a response mechanism to stress are loss of enzymatic activity, altered cellular functions such as energy production, and changes in the type and level of cellular proteins. Protein oxidation products are usually aldehydes, keto compounds, and carbonyls. Among the various oxidative modifications of amino acids in proteins, carbonyl formation may be an early marker of protein oxidation. Increases in carbonyl levels have been detected in several diseases such as rheumatoid arthritis (Chapman *et.al.,* 1989) and ischemia-reperfusion injury to heart muscles (Serbinova *et.al.,* 1992). Another example of specific target of oxidative damage are lipids; all cellular membranes are especially vulnerable to oxidation due to their high concentration of unsaturated fatty acids. The main oxidative damage in lipids is their peroxidation (Halliwell *et. al.,* 1999). The significance of the damage inflicted upon biological systems by ROS cannot be overestimated, as they are implicated in numerous disease processes, including degenerative diseases and tumor formation (Kohen and Nyska, 2002).

Protein oxidation and lipid peroxidation generated by BGO nanoparticles and multi-wall carbon nanotubes (MWCNT) (used for comparison since they are

also proposed materials for biomedical applications) were analyzed in different tissues. According to the literature (Oberdorster, 2004; Larsericsdotter *et.al.,* 2005; Norde *et.al.,*1999; Roddick-Lanzilotta *et.al.,* 1998), cells may be damaged by nanomaterials due to the affinity of these nanomaterials to localize in regions rich in proteins and lipids. In the present study, liver, gill, brain, ovary and testicle tissues were selected to test oxidative stress caused by BGO nanoparticles. The latter two tissues were selected because they are particularly rich in hormones, and hormones are proteins.

Figure 49 shows the different levels of protein oxidation in the studied tissues. The capacity of MWCNT and BGO nanoparticles to affect proteins can be appreciated in the increased carbonyl content. The presence of carbonyl groups in proteins was therefore used as a marker of ROS-mediated protein oxidation (Levine *et.al.,* 1997).

The amount of oxidized protein was lower with 1 ppm of BGO than the effect of the H_2O_2 exposure used as positive control, except in liver. The effect of BGO was always lower than the effect of MWCNT at 1 ppm. Results improved markedly when BGO concentration was lowered to 0.5 ppm, since the level of oxidation in all the organs was less than 50% that of the H_2O_2 and MWCNT (at 0.5 ppm) treatments. Besides, the low carbonyl content observed with BGO, 0.5 ppm only caused a slightly higher protein oxidation in fish than the control experiment which used only water. At this concentration, the oxidative stress effect of BGO nanoparticles is negligible.

Lipid peroxidation was the complementary assay to evaluate the oxidative stress degree caused by MWCNT and BGO nanoparticles. Fish exposed to 1 ppm of BGO showed equal lipid peroxidation levels as those caused by H_2O_2 in ovaries, gills and brain, while the levels caused by 1 ppm of MWCNT doubled the value of BGO nanoparticles in the same organs. In liver and testicles, the lipid peroxidation caused by BGO nanoparticles was higher than that caused by H_2O_2 and the levels reached 75-80% of the values induced by 1ppm of MWCNT.

Treatments with 0.5 ppm of BGO produced a lipid peroxidation compared to that obtained with H_2O_2. Nevertheless, when compared with the control using water, the increment induced by BGO particles was 66% in liver, 60% in ovaries, 33% in testicles, 8% in gills and 10% in the brain. The levels of protein oxidation and lipid peroxidation at 0.5 ppm BGO concentration are close to the control assay using water, which suggests low oxidative stress at this nanoparticle concentration.

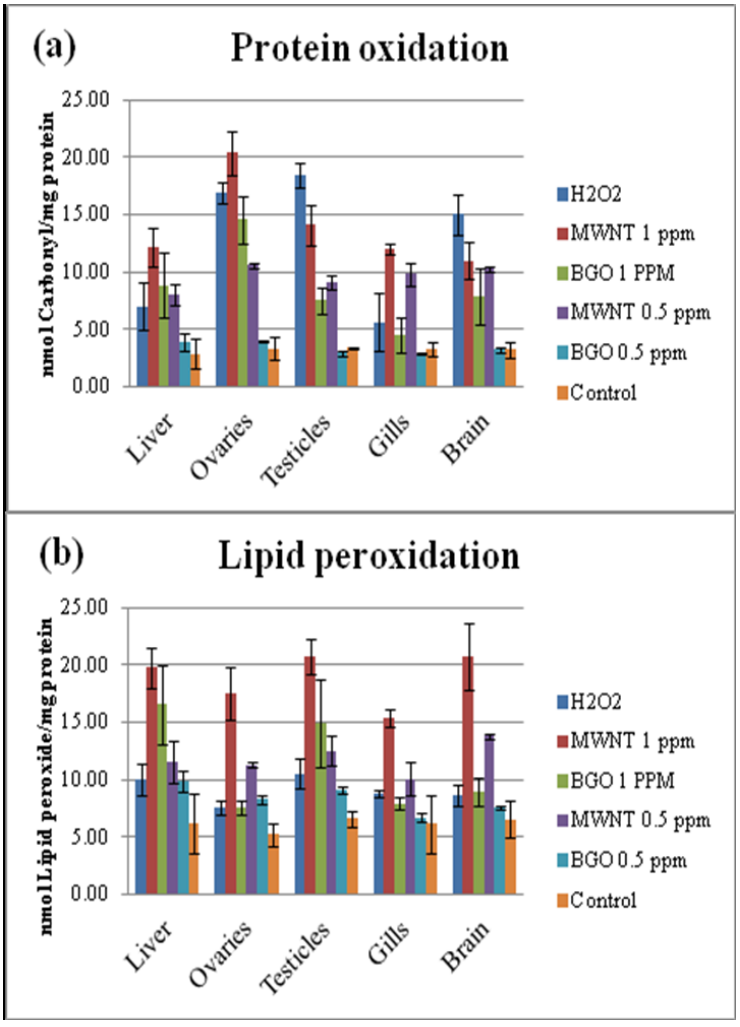

Figure 49. *Protein oxidation and lipid peroxidation at different concentration of BGO nanoparticles and multi-wall carbon nanotubes (MWNT). The MWNT (red) and BGO (green) with a concentration of 1 ppm and MWNT (purple) and BGO (cyan) with a concentration of 0.5 ppm (purple). All concentrations were compared with the peroxide, H_2O_2 (blue) and using water as control (orange).*

V.2.7 Medical radiology

Figure 50 shows the uncoated and coated BGO nanoparticles with BSA protein irradiated with an X-ray source with an energy of 52 kV and a current of 255 mA for 1.333 sec of exposure time. Medical radiology is a standard technique for identification of neoplasms and problems in bones. In order to avoid unnecessary radiation doses to the patient, recent experiences have shown that there is a need to consider many factors such as voltage, current and time exposure (Kumar *et.al.,* 2011). It is important to keep the radiation doses in patients to a minimum, because the use of X-rays in medicine for diagnosis represents the largest man-made source of public exposure to ionizing radiation. The radiology parameters used in this experiment correspond to those typically used to obtain a hand radiography of a 33-year old human (Kumar *et. al.,* 2011). The BGO nanoparticles functionalized with BSA protein irradiated with X-ray radiation preserved their luminescence properties. The emission in the blueish-white visible region was observed (Figure 50) and captured with a camera. The images demonstrate that functionalized BGO particles can emit light with low X-ray doses, which are frequently applied to obtain human radiographs (Huda *et.,* 2010). This may be used to locate BGO nanoparticles efficiently within a human body with low X-ray doses.

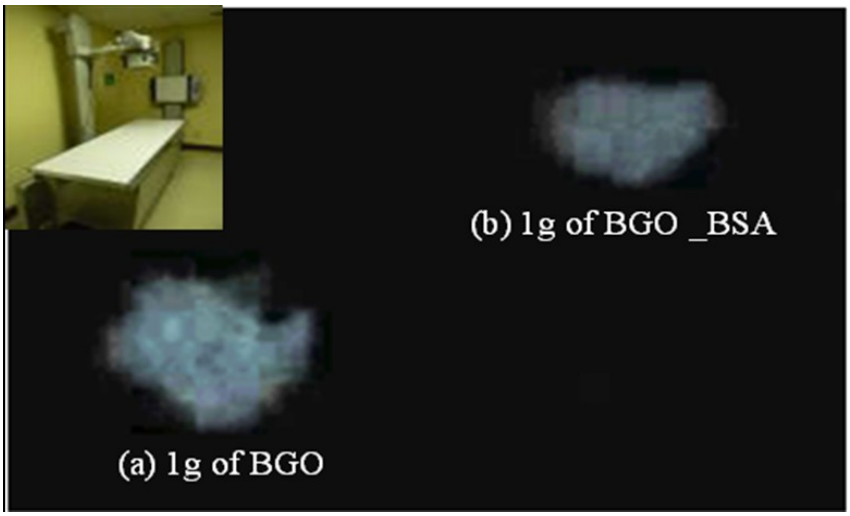

Figure 50. *BGO nanopowders uncoated (a) and coated with BSA protein (b) under X-ray excitation with an energy of 52 kV with a current of 255 mA with a exposure time of 1.333 sec in a radiology room (inset).*

V.3 HA:Eu and BGO nanoparticles functionalization

V.3.1 Antibody functionalization and cell recognition

The side scatter (SSC, complexity) and forward scatter (FSC, size) profile of non-functionalized and Ab- coated HA:Eu and BGO nanoparticles were investigated by flow cytometry. Figure 51 shows where the non-functionalized HA:Eu and BGO nanoparticles are positioned in the forward scatter (FSC) versus the side scatter (SSC) in a log-log plot. The plots show a distribution along the 10^4 to 10^5 values that confirms the heterogeneity of both nanoparticles. The pattern was identical independently of whether particles were functionalized with the W6/32 mAb (not shown) or not.

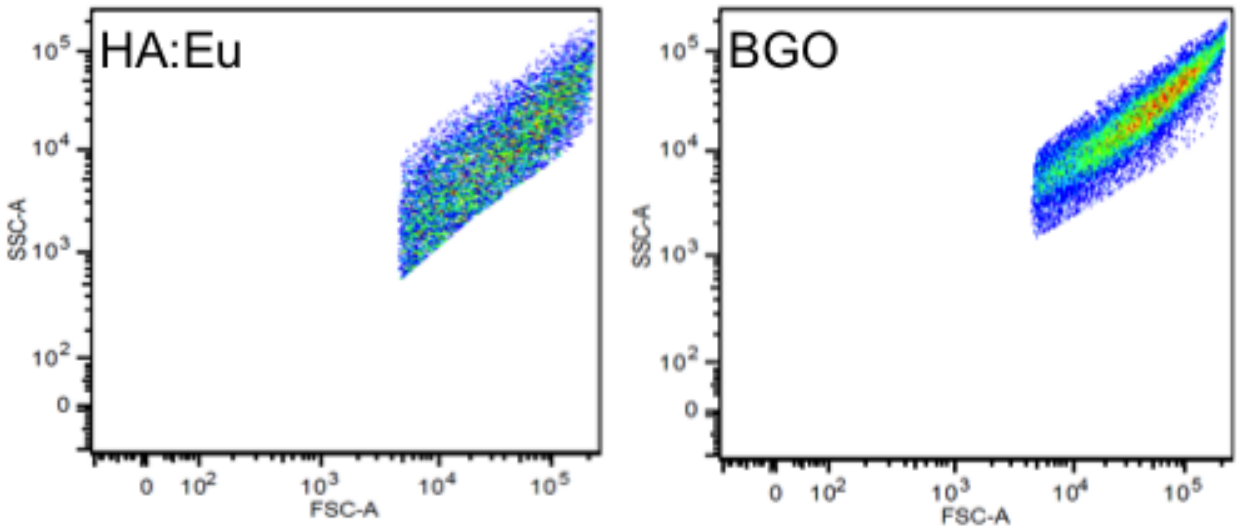

Figure 51. *Scattering of non-conjugated HA:Eu and BGO nanoparticle.*

Secondly, we evaluated the capacity of coupling antibodies to particles that were either functionalized with BSA and carbodiimide, only carbodiimide or left untreated prior to adsorb the W6/32 mAb by measuring the binding of a fluorophore-labeled secondary antibody to the nanoparticles. Figure 52 represents the histograms of the different suspensions prepared with the HA:Eu and BGO nanoparticles (Table IV); nanoparticles without antibodies were added as negative controls. Almost 100% of the HA:Eu and BGO nanoparticles were more fluorescent than their counterparts, which were either not functionalized with the W6/32 mAb but incubated with the A488-labeled secondary antibody (control), or functionalized with the W6/32 mAb but not incubated with the secondary antibody probe (data not shown).

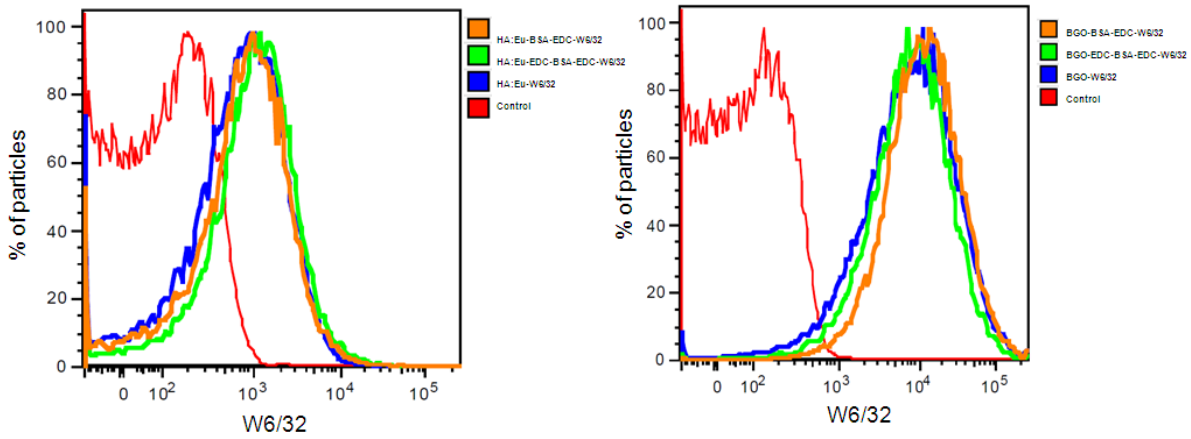

Figure 52. *Histograms of W6/32-conjugated HA:Eu and BGO nanoparticles subsequently treated with fluorophore-conjugated anti-mouse IgG. A solution of nanoparticles without antibody was added as control.*

Quantitative flow cytometry was then carried out to assess whether the binding capacity of the W6/32 mAb to its cognate antigen (HLA I) on the THP-1 cell surface was not lost during the carbodiimide (EDC) treatment of the nanoparticles. Figure 53 A shows the relative size (FSC) and complexity (SSC) of both the nanoparticles (NP) and cells (THP-1) on a linear scale. The NP plot is for HA:Eu and was the same for BGO (not shown here). Interestingly, when the THP-1 cells were incubated with the HA:Eu- or the BGO- W6/32 labeled particles, the complexity/granularity of the cells was enhanced (upward shift) as a result of the binding of the antibody-labeled particles to the HLA-I molecules on the cell surface (blue dot plot), as compared to THP-1 cells incubated with particles not labeled with mAb (red dot plot) (Figure 53 B, upper panels). The positive shift of the histograms shown on the lower panels of Figure 53 B indicate that, of the total viable cells, almost 100% bound mAb-labeled nanoparticles that were tagged by the Alexa 488 labeled-secondary antibody.

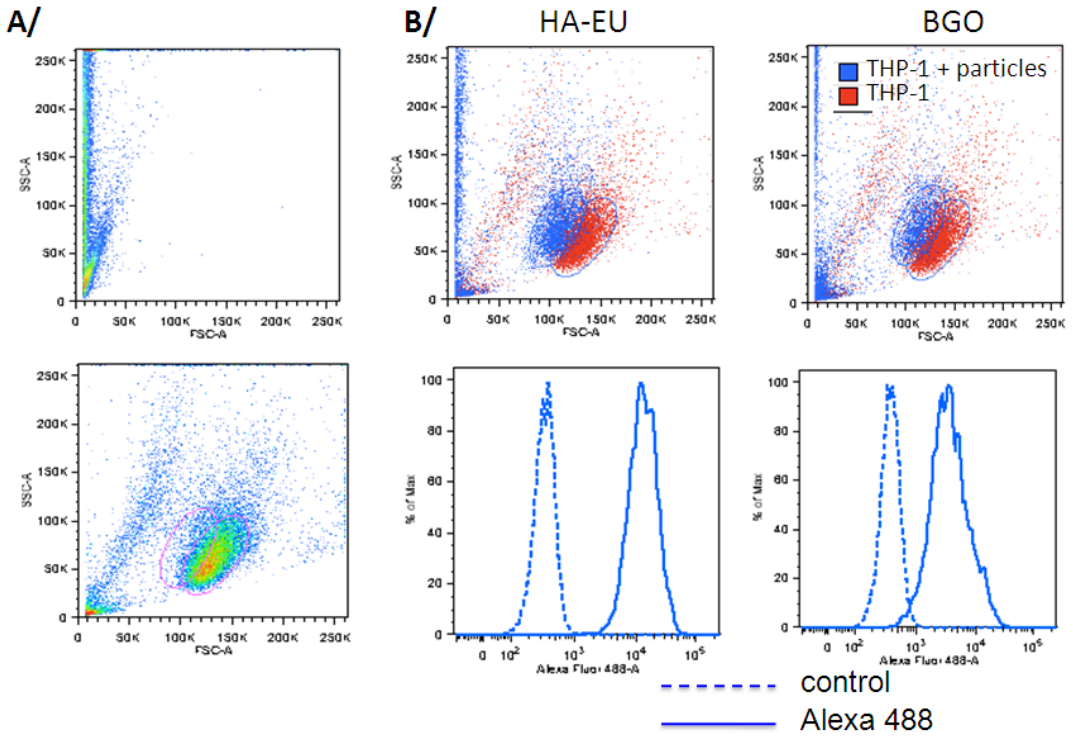

Figure 53. *HA-Eu- and BGO-W6/32 mAb labeled recognize HLA-I molecules on THP-1 cells. A/ Relative size and complexity of nanoparticles (NP, upper panel) and control THP-1 cells (lower panel) on a linear scale. B/ Complexity of THP-1 cells incubated with mAb-labeled nanoparticles (blue dot plots) or without nanoparticles (red dot plots) upper panel. Fluorescence histogram of the THP-1 cells combined with the W6/32-functionalized nanoparticles (lower panel), incubated with or without Alexa488 secondary antibody (continuous line and dashed line, respectively).*

THP-1 cell recognition by the W6/32-functionalized HA:Eu and BGO nanoparticles was also assessed via optical microscopy. HA:Eu and BGO nanoparticle association to the cell membranes was confirmed. Figure 54 displays in green the emission at 519 nm of the Alexa 488 fluorophore conjugated to the secondary antibody, which confirms that the W6/32 mAb-labeled HA:Eu nanoparticles can recognize their cognate antigen on the cell surface. The red emission is due to the HA:Eu nanoparticles, which preserved their photoluminescence properties despite the functionalization with the two antibodies.

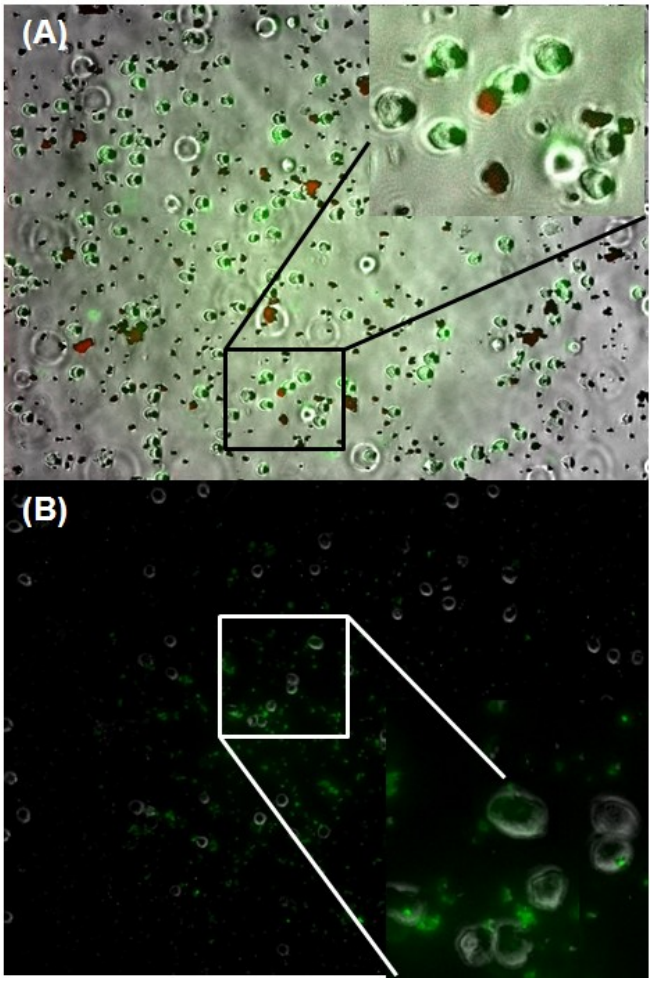

Figure 54. *A) Composite image with red and green filter in brightfield of the THP-1 cell recognition by the IgG-fluorophore antibody labeled HA:Eu nanoparticles. B) Image of fluorescence on the THP-1 cell surface due to BGO nanoparticles functionalized with W6/32 antibody. Objective 60X and ocular 10X, final magnification 600X.*

The most important result of this work is that HA:Eu and BGO nanoparticles can be functionalized with W6/32 antibodies, and that they recognize cell surface molecules such as the MHC I molecules on THP-1 cells. This proves that BGO and HA:Eu are suitable as biomarkers.

In addition to this result, a further benefit emerged from this study. The quite similar scintillating behavior of BGO nanoparticles compared with the commercial

single crystal BGO detectors suggests that BGO nanoparticles could be good components of high-energy detectors.

Other features of BGO found in this study prove that it is an interesting candidate for further biological applications such as revealing the presence and position of tumors. These features are the lower oxidative stress caused by BGO, when compared with carbon nanotubes and H_2O_2; the fluorescence detected under excitation with low emissions of X-rays even when the nanoparticles were coated with BSA; antibody recognition of neoplastic cell antigens by functionalized BGO nanoparticles together with their scintillation properties; and, lastly, their stability in different biological environments.

Summary Results

In summary, the present thesis was focused on the hypothesis that the luminescent properties of europium-activated hydroxyapatite (HA:Eu) and bismuth germanate (BGO) nanoparticles are stable in body fluids, and that these nanoparticles can be appropriately functionalized to identify human tumor cells.

Europium-activated hydroxyapatite and bismuth germanate nanoparticles were synthesized by the sol-gel method with subsequent annealing at 950 and 1200°C, respectively. Physical characterization of the nanoparticles was done by XRD, TEM, PL; additionally, RL was tested for BGO. These results showed luminescent nanoparticles that proved to be highly stable in different body fluids at different pH values.

Analysis of oxidative stress caused in different body tissues of zebrafish showed less damage to proteins and lipids caused by BGO nanoparticles than by carbon nanotubes.

HA:Eu and BGO were functionalized with BSA protein and, according to the protein quantification experiments, the following protein concentrations were attached to each nanoparticles species: HA:Eu 79.3, and BGO 134.9 (μg protein /g NP).

To test if the synthesized nanoparticles can be used in biomedical applications, they were functionalized with the monoclonal W6/32 antibody, which recognizes the HLA 1 human antigen. Both HA-Eu and BGO nanoparticles preserved their luminescent properties before and after functionalization (Figure 55). In addition, the functionalized nanoparticles recognized HLA 1 and attached to

the surface of the membrane of human acute monocytic leukemia cells, line THP-1.

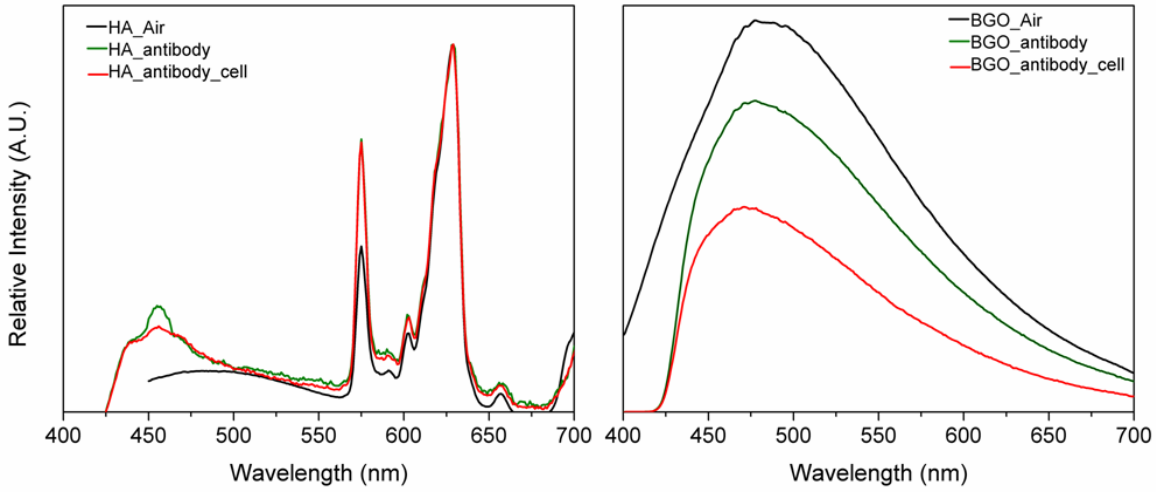

Figure 55. *Emission spectra of HA and BGO nanoparticles in air (black line);of antibody-functionalized nanoparticles (green line) suspended in FACS buffer, and of antibody-functionalized nanoparticles suspended in FACS buffer containing THP-1 cells (red line).*

Figure 55 shows that the luminescence properties of both nanoparticle types were preserved. When emission spectra were read in buffer, and then with added THP-1 cells, luminescence diminished progressively probably due to the light absorption of the different media.

The results of this thesis indicate that HA-Eu and BGO nanoparticles are promising candidates to be considered as biomarkers.

Conclusions

- Eu-activated hydroxyapatite and bismuth germanate nanoparticles were successfully synthesized by the sol-gel method.

- PL, RL and decay time results suggest that BGO nanoparticles are suitable for scintillation applications.

- Eu-activated hydroxyapatite and bismuth germanate nanoparticles presented high optical stability in organic components such as human urine, blood serum and proteins. Additionally, they preserved their luminescence properties under different pH concentrations.

- The low toxicity and photoluminescence stability of Eu-activated hydroxyapatite and bismuth germanate nanophosphors render them promising as biomarkers for medical applications.

- HA:Eu and BGO nanoparticles were successfully functionalized with BSA protein and with W6/32 antibody.

- W6/32 antibody-functionalized HA-Eu and BGO nanoparticles recognized human acute monocytic leukemia cells.

- Further investigations are needed to determine the applicability of these nanoparticles to specific cancer cell detection of human neoplasms.

References

- Alivisatos A. P.2000, *Naturally Aligned Nanocrystals*. Science. 289: 736-737.

- Alivisatos A.P., Gu W.W. and Larabell C. 2005, *Quantum dots as cellular probes*. Annu. Rev. Biomed. Eng. 7: 55-76.

- Allen T.M., Cullis P.R. 2003, *Drug delivery systems: Entering the mainstream*. Science. 303:1818-1822.

- Andreeta M.R.B, de Jesus F.A.A.A., Hernandes A.C. and Macedo Z.S. 2010, *Bismuth germanate films prepared by Pechini method*. Opt. Mat. 32: 1286-1290.

- Aoki H. 1991, *Science and Medical Applications of Hydroxiapatite*. Japan. Asoc. of Apati. Scien. 1-214.

- Atkinson A., Meyer B., StuBing D., Hagen W., Schmidt K. and Bathmann U.V. 2002, *Feeding and energy budgets of Antartic krill at the onset of winter.* Juveniles and adults. Limnol. Oceanogr. 47: 953-956.

- Bae Y.H. 2009, *Drug targeting and tumor hetereogenety*. J. control. Releas. 133: 2-3.

- Balamurugan A., Kannan S. and Rajeswari S. 2002, *Bioctive sol-gel hydroxyapatite surface for biomedical applications-in vitro study*. Trend. Biomater. Artif. Organs. 16:18-20.

- Beneventi P., Bersani D., Lottici P.P. and Kovacs L. 1995, *A Raman study of* $Bi_4(Ge_xSi_{1-x})_3O_{12}$ *crystals.* Sol. Stat. Commun. 93:143-146.

- Betts F. and Posner A.S. 1974, *An X-ray radial distribution study of amorphous calcium phosphate*. Mater. Res. Bull. 9: 353–360.

- Bicknese S., Zahra Shahrokh, Stephen B. Shohet, and A. S. Verkman. 1992, *Single photon radioluminescence:Theory and spectroscopic properties*. J. Biophys. 63: 1256-1266.

- Blanchard C.R. 1996, *Atomic Force Microscopy*. The chemical educator. Springler, New York.

- Blasse G. and Grabmaier B.C. 1994, *Luminiscent materials*. Springer, New York.

- Bohner M. 2000, *Calcium orthophosphates in medicine: from ceramics to calcium phosphate cements*. Injury 31: D37–47.

- Bordun O.M. 2001, *Influence of oxygen vacancies on the luminescence of thin $Bi_4Ge_3O_{12}$ films*. J. Appl. Spectr. 68: 974-978.

- Bradford, M.M. 1976, *A rapid and sensitive method for the quantitation of microgram quantities of protein utilizing the principle of protein-dye binding*. Anal. Biochem. 72: 248-254.

- Brinker, C.J., Scherer, G.W. 1990, *Sol-gel science*. Academic Press, San Diego.

- Bruchez M., Jr., Moronne M., Gin P., Weiss S., Alivisatos A. P., Chan W. C. W., Nie S. M. 1998, *Semiconductor Nanocrystals as Fluorescent Biological Labels.* Science, 281: 2016 -2018.

- Byrne J.D, Betancourt T., Brannon-Peppas L. 2008, *Active targeting schemes for nanoparticle systems in cancer therapeutics*. Adv. Drug. Deliv. Rev. 60:1615–1626.

- Cai W., Shin D.W., Chen K., Gheysens O., Cao Q., Wang S.X., Gambhir S.S. and Chen X. 2006, *Quantitative PET of EGFR expression in xenograft-bearing mice using ^{64}Cu-labeled cetuximab, a chimeric anti-EGFR monoclonal antibody*. Nano. Lett. 6: 669.

- Carrillo Vital Y.,2012, *Monitoreo de estrés oxidativo causado por nanopartículas en pez cebra (Danio rerio) usando la oxidación de proteínas y la peroxidación de lípidos como biomarcador*. Rev. de Toxicolo. 1:35-37

- Chan W.C.W. 2006, *Bionanotechnology progress and advances.* Biolo. of Blood and Marrow Transplant. 12:87-91.

- Chapman M.L., Rubin B.R., Gracy R.W. 1989, *Increased carbonyl content of proteins in synovial fluid from patients with rhematoid arthritis*. J Rheumatol. 16:15-18.

- Chapman Y.P., Courchesne E.B. and Derenzo S.E. 2008, *Bi^{3+} Luminescence in BiO_2Cl (A = Sr, Ba) and $BaBiO_2Br$*. J. Lumin. 128: 87–91.

- Chiodini N., Fasoli M., Martini M., Rosetta E., Spinolo g., Nikl M., Solovieva N., Baraldi A., Capelletti R. and Vedda A. 2002, *High-efficiency SiO_2:Ce^{3+} glass scintillators*. Appl. Phys. Lett. 81:4374-4376.

- Cho J.H., Kim S.J. and Yang Y.S. 2001, *Structural change in $Bi_4(Si_xGe_{12-x})_3O_{12}$ glasses during crystallization.* Sol. Stat. Commun. 119:465-470.

- Cho K, Wang X, Nie S, Chen ZG, Shin DM. 2008, *Therapeutic nanoparticles for drug delivery in cancer*. Clin. Cancer. Res. 14:1310–1316.

- Christoffersen J., Christoffersen M.R, Larsen R., Moller I.J. 1991, *Regeneration by surface-coating of bone char used for defluoridation of water*. Wat. Res. 2:227-229.

- Chung C. and Chan C.C. 1994, *Application of BGO detector to monitor in situ ^{16}N concentration in a reactor pool*. J. Radioanalytical and Nuclear Chem. 180: 131-371.

- Cohen B.I., Setoguchi T., Mosbach E.H., McSherry C.K., Stenger R.J., Kuroki S., Soloway R.D. 1987, *An animal model of pigment cholelithiasis*. Am. J. Surg. 53:130-8.

- Compton, S.J. and Jones, C.G. *Mechanism of dye response and interference in the Bradford protein assay*. 1985, Anal. Biochem. 151: 369-374.

- Davies K.J.A. 1987, *Protein damage and degradation by oxygen free radicals*. J. Biol. Chem. 262:9895-9901.

- De Araujo T.S., Macedo Z.S., De Oliveira P.A.S.C. and Valerio M.E.G. 2007, *Production and characterizationof pure and Cr^{3+}-doped hydroxyapatite for biomedical applications as fluorescent probes*. J. Mater. Sci. 42: 2236-2243.

- De Jesus F.A.A., Silva R.S. and Macedo Z.S. 2010, *Synthesis of $Bi_4Ge_3O_{12}$ ceramic scintillators by the polymeric precursor method*. J Therm. Anal. Calorim. 100: 537–41.

- De Jesus F.A.A., Silva R.S., Hernandes A.C. and Macedo Z.S. 2009, *Effect of pH on the production of dispersed $Bi_4Ge_3O_{12}$ nanoparticles by combustion synthesis*. J. European Ceram. Soc. 29: 125-130.

- Deeb M.E., Hosny M., Sharawy M. 1989, *Osteogenesis in composite grafts of allogenic demineralized bone powder and porous hydroxyapatite*. J. Oral Maxillofac. Surg. 47: 50-56.

- Denissen H.W., de Groot K., Makkes P.C., Van den Hooff A., Klopper P.J. 1980, *Tissue response to dense apatite implants in rats*. J. Biomed. Mater. Res. 6:713-721.

- Dorenbos P. 2002, *Crystal field splitting of lanthanide $4f^{n-1}5d$-levels in inorganic compounds*. J. of Alloy. and Compoun. 341:156–159

- Drucker D.A., Capello W.N., D'Antonio J.A., Hile L.A. 1991, *Works in progress #6. Total hip arthroplasty using a hydroxyapatite-coated acetabular and femoral component.* Orthoped. Revi. 20:179-192.

- Ouenzerfi R., Kbir-Ariguib N., Trabelsi-Ayedi M. and Piriou B. 1999, *Spectroscopic study of Eu^{3+} in strontium hydroxyapatite $Sr_{10}(PO_4)_6(OH)_2$*. J. Lumin. 85:71–77.

- El-Ouenzerfi R., Goutaudier C., Cohen-Adad M.T., Panczer G. and Boulon G. 2003, *Luminescent properties of rare-earth (Eu^{3+}, Eu^{2+} and Ce^{3+}) doped apatitic oxyphosphosilicates*. J. Lumin. 103:426–33.

- Esterbauer, H. and Cheeseman, K.H. 1990, *Determination of aldehydic lipid peroxidation products: malonaldehyde and 4-hidroxynonenal*. Metho. in Enzimolo. 186.

- Eychmüller A. 2000, *Structure and Photophysics of Semiconductor Nanocrystals*. J. Phys. Chem. B 104: 6514- 6528.

- Fakruddin M, Hossain Z, Afroz H. 2012, *Prospects and applications of nanobiotechnology: a medical perspective*. J. Nanobiotechnology. 10:31-33.

- Feynman R. P. 1961, *In Miniaturization*, Reinhold, New York, p. 282-296.

- Frigault, M.M., Lacoste, J., Swift, J.L and Brown, C.M., 2009. *Live-cell microscopy: Tips and tools.* J. Cell. Sci. 122:753–767.

- Fujimoto, J.G and Farkas, D., Eds., *Biomedical Optical Imaging*, Oxford University Press, 2009.

- Gaft M., Reisfeld R., Panczer G., Shoval S., Champagnon B. and Boulon G. 1997, *Eu^{3+} luminescence in high-symmetry sites of natural apatite*. J. Lumin. 74: 572–574.

- Gao, X.H., Yang, L., Petros, J.A., Marshall, F.F., Simons, J.W. and Shuming, N. 2006, *The pinpoint promise of nanoparticle-based drug delivery and molecular diagnosis*. Biomole. Engenie. 23:171-184.

- Gay G.A. and Gebicki, J.M. 2003, *Measurement of protein and lipid hydroperoxides in biological systems by the ferric–xylenol orange method*. Anality. Biochemis. 315:29-35.

- Gfroerer T. 2000, *Photoluminescence in Analysis of Surfaces and Interfaces*.*Encyclopedia of Analytical Chemistry* Wiley, Chichester.

- Goldman, R.D., Swedlow, J.R and Spector, D.L., Eds. 2009, *Live Cell Imaging: A Laboratory Manual, Second Edition*, Cold Spring Harbor Laboratory Press.

- Goldys E.M., Drozdowicz-Tomsia K, Jinjun S, Dosev D, Kennedy IA, Yatsunenko S and Godlewski M. 2006, *Optical Characterization of Eu-Doped and Undoped Gd_2O_3 Nanoparticles synthesized by the Hydrogen Flame Pyrolysis Method.* J. Amer. Chem. Soc. 128: 14498-14505.

- Graeve A.O., Kanakala R., Madadi A., Williams B.C. and. Glass K.C. 2010, *Luminescence variations in hydroxyapatites doped with Eu^{2+} and Eu^{3+} ions*. Biomaterials 31: 4259-4267.

- Greskovich C.and Duclo S. 1997, *Ceramic Scintillators*. Annu. Rev. Mater. Sci. 27:69–88.

- Grundmann M. 1999, *The present status of quantum dot lasers.* Physica E. 5:169.

- Guerrero, Aldo. 2012, Síntesis por el método hidrotermal y catodoluminiscencia de nanovarillas de ZnO dopado con Mn. Thesis.

- Gullotti E, Yeo Y. 2009, *Extracellularly activated nanocarriers: a new paradigm of tumor targeted drug delivery*. Mol. Pharm. 6:1041-51.

- Gutteridge J.M., Halliwell B. 1990,*The measurement and mechanism of lipid peroxidation in biological systems*. Trends Biochem. Sci.15:129-135.

- Haglund E., Seale-Goldsmith M.M., Leary J.F. 2009, *Design of multifunctional nanomedical systems*. Ann. Biomed. Eng. 37:2048-63.

- Hahn M.A., Singh A.K., Sharma P., Brown S.C., Moudgil B.M. 2011, *Nanoparticles as contrast agents for in-vivo bioimaging: current status and future perspectives*. Anal. Bioanal. Chem. 399: 3–27.

- Halliwell B., Gutteridge J.M.C. 1999, *Free radicals in biology and medicine*. 3rd ed. Oxford: Oxford University Press.

- Hamlekhan, M. Mozafari, N. Nezafati, M. Azami, and H. Hadipour. 2010, *A proposed fabrication method of novel PCL-GEL-HAp nanocomposite scaffolds for bone tissue engineering applications*. *Composites* 4:123.

- Han Y., Wang X. and Li S. 2009, *A simple route to prepare stable hydroxyapatite nanoparticles suspension*. J. Nanopart. Res. 11: 1235-1240.

- Hell, S.W. 2009, *"Microscopy and its focal switch,"* Nat. Methods. 6:24–32.

- Hellman, S. 1993, *Dogma and Inquisition in Medicine. Cancer.* 71: 2430-2433.

- Hench L.L. and Ethridge E.C. 1982, *Biomaterials: An interfacial Approach*. Academic Press, New York.

- Hibbs, A.R., 2004, *Confocal Microscopy for Biologists*, Springer, New York.

- Huda W. and Mettler FA. 2010, *Relationship between radiographic techniques (kilovolt and mill ampere-second.* J. of Radiati. Protect. Dosimet. 141:43-49.

- Hulka B.S. 1990, *Overview of biological markers. In: Biological markers in epidemiology*. Oxford University press, New York, 3-15.

- Iliescu T., Maniu D., Chis V., irimie F.D., Paizs C. and Tosa M. 2005, *NIR surface enhanced Raman spectroscopy and bands assignment by DFT calculation of non natural β-amino acids.* Chem. Phys. 310:189-199.

- Jabir N.R., Tabrez S., Ashraf G.M., Shakil S., Damanhouri G.A., Kamal M.A. 2012, *Nanotechnology-based approaches in anticancer research*. Int. J. Nanomed. 7:4391-408.

- *Jagannathan R. and Kottaisamy M. 1995, Eu^{3+} luminescence: A spectral probe in $M_5(PO_4)_3X$ apatites (M=Ca or Sr; X=F^-, Cl^-, Br^- or OH^-) J. Phys. Cond. Matter. 7:8453-8466.*

- Jain K.K. 2010, *Advances in the field of nanooncology.* BMC Med. 8: 83-87.

- Jain K.K. 2008, *Recent advances in nanooncology*. Technol Cancer Res Treat. 7:1-13.

- Joris, S.J. and Amberg, C.H. 1971, *The nature of the deficiency in nonstoichiometric hydroxyapatite. II.Spectroscopic studies of calcium and strontium hydroxyapatite*. *J. Phys. Chem. 75*: 3172–3178.

- Jun Y.W., Huh Y.M. and Choi J.S. 2005, *Nanoscale size effect of magnetic nanocrystals and their utilization for cancer diagnosis via magnetic resonance imaging.* J. Am. Chem. Soc. 127:5732-5733.

- Kaufmann E.N. 2003, *Characterization of materials.* Wiley, New York.

- Kawasaki T**.**, Niikura M**.**, Takahashi S**.**, Kobayashi W. 1987, *Strontium-phosphate hydroxyapatite high-performance liquid chromatography*. Biochem. Int. 15:1137-49.

- Khan S.R. and Glenton P.A.1995, *Deposition of calcium phosphate and calcium oxalate crystals in the kidneys.* J. Urol. 153: 811-817.

- In: The Chemistry of Surfaces. 1972, Kibby, C. L. and Hall, W. K., .*Surface Properties of Calcium Phosphates* Marcel Decker Inc., New York. 663-730.

- Kim I.S. and Kumta, P.N. 2004, *Sol-gel synthesis and characterization of nanostructured hydroxyapatite powder*. Mater. Sci. and Eng. B 111: 232-236.

- Knubovets. 1993, *Structural mineralogy and properties of natural phosphates*. Rev. Chem. Eng. 9:161-165.

- Kohen R. and Nyska A. 2002, *Oxidation of biological systems: Oxidative stress phenomena, antioxidants, redox reactions, and methods for their quantification.* Toxicolo. Patholo. 30:620-650.

- Kottaisamy M., Jagannathan R., Jeyagopal P., Rao R.P. and Narayan R. L. , 1994, *Eu^{2+} luminescence in $M_5(PO_4)_3X$ apatites, where M is Ca^{2+}, Sr^{2+} and Ba^{2+}, and X is F^-, Cl^-, Br^- and $OH^\$$*. J Phys. D: Appl. Phys. 27: 2210.

- Koutsopoulos S, Kontogeorgou A, Petroheilos J, Dalas E. *Calcification The mechanism of biological mineralization* 135:33–44.

- Kumar G.A., Kumar P. and Malleswararao V. 2011, *Evaluation on X-ray exposure parameters considering tube voltage and exposure time*. Int. J. Engine. Sci. Technol. 3:3210-3215.

- Kumari L., Lin J.H. and Ma Y.R. 2007, *Synthesis of bismuth oxide nanostructures by an oxidative metal vapour phase deposition technique*. Nanotechnology 18: 595-605.

- Langer R. 1998, *Drug delivery and targeting*. Nature 392: 5-10.

- Langer R. 2003, *Where a pill won't reach*. Sci. Am. 288: 50-57.

- Langer R. and Peppas N.A. 2003, *Advances in biomaterials, drug delivery, and bionanotechnology*. Al. Che. J. 49: 2990-3006.

- Lazoryak B.I., Strunenkova T.V., Vovk E.A., Mikhailin VV., Shpinkov I.N. and Romanenko Y. 1996, *The new phosphates $Ca_9MLn_{2/3}(PO_4)_7$ (M¼ Li, Na; Ln¼ rare earth, Y, Bi)*. Mater. Res. Bull. 31:665–71.

- Lebugle A., Zahidi E. and Bonel G. 1986, *Effect of structure and composition on the thermal decomposition of calcium phosphates (Ca/P ¼ 1.33)*. React Solid 2:151–61.

- Lee E.S., Oh K.T., Kim D., Youn Y.S. and Bae Y.H. 2007, *Tumor pH-responsive flower like micelles of poly(L-lactic acid)-b-poly(ethylene glycol)-b-poly(L-histidine)*. J controlled Release 123:19-26.

- Levine R.L, Williams J.A, Stadtman E.R. and Schacter E. 1994*, Carbonyl assays for determination of oxidatively modified proteins. Methods Enzymol.* 233: 346-357.

- Lin F.H., Liao C.J., Chen K.S. and Sun J S. 1998, *Preparation of high-temperature stabilized b-tricalcium phosphate by heating deficient hydroxyapatite with $Na_4P_2O_710H_2O$ addi*tion. Biomaterials 19:1101–7.

- Liu D.M., Troczynski T. and Tseng W.J. 2001, *Water-based sol–gel synthesis of hydroxyapatite: process development.* Biomaterials 22:1721–30.

- Locatelli F, Canaud B, Eckardt KU, Stenvinkel P, Wanner C, Zoccali C. 2003, *The importance of diabetic nephropathy in current nephrological practice*. Nephrol. Dial. Transplant. 18:1716-1725.

- Macedo Z.S., Silva R.S., Valerio M.E.G. and Hernandes A.C. 2004, *Radiation detectors based on laser sintered $Bi_4Ge_3O_{12}$ ceramics*. Nuclear Instrum. Meth. B, 218: 153-157.

- Madani S.Y., Naderi N., Dissanayake O., Tan A. and Seifalian A.M. 2011*, A new era of cancer treatment: carbon nanotubes as drug delivery tools*. Int. J. Nanomed. 6: 2963–2979.

- Martin C. R. 1994, *Nanomaterials: A Membrane-Based Synthetic Approach*. Science 266: 1961-1966.

- Martínez Castro J., Flores R. and Vazquez Duhaltl R. 2011, *Molecular design of laccase cathode for direct electrón transfer in a biofuel cell*. Biosenso. and Bioelectro. 26: 2626-2631.

- Mavropoulos E., Rocha-Leão M.H., da Rocha N.C.C., Prado da Silva M.H., and A.M. Rossi. 2007, *Hydroxyapatite-alginate composite for lead removal in artificial gastric fluid*. J. Mater. Res. 22: 3371-3377.

- *Mayeux R. 2004, Biomarkers: Potential Uses and Limitations*. J. Amer. Soc. for Exp. NeuroThe. 1:182-188.

- Mehmel A.M. 1973, *Applied Mineralogy*. Springer, Wien.

- Meier B., Radeke H., Selle S. 1990, *Human fibroblasts release reactive oxygen species in response to treatment with synovial fluids from patients suffering from arthritis*. Free. Radic. Res. Commun. 8:149-60.

- Melcher C.L., Schweitzer J.S., Liberman A. and Simonetti J. 1985, *Temperature Dependence of Fluorescence Decay Time and Emission Spectrum of Bismuth Germanate*. IEEE Trans. Nuc. Sci. NS-32: 1:529-532.

- Meyers M.A., Chen P.Y., Lin A. and Seki Y. 2008, *Biological materials: Structure and mechanical properties*. Progres. in Material. Scien. 53:1–206.

- Mitchell G.P., Mirkin C.A., Letsinger R.L. 1999, *Programmed assembly of DNA functionalized quantum dots.* J. Am. Chem. Soc. 121: 8122-8123.

- Monma H., Ueno S. and Kanazawa T. 1981, *Properties of hydroxyapatite prepared by the hydrolysis of tricalcium phosphate*. J. Chem. Technol. Biotechnol. 31:15–24.

- Mortier A., Lemaitre J. and Rouxhet P.G. 1989, *Temperature-programmed characterization of synthetic calcium-deficient phosphate apatites*. Thermochim. Acta. 143: 265–282.

- Murray M.G.S., Wang J., Ponton C.B. and Marquis P.M. 1995, *An improvement in processing of hydroxyapatite ceramics*. J. Mater60. Sci. 30: 3061–3074.

- Murray R.K., Granner D.K., Mayes P.A. and Rodwell V.W. 2000, B*iochemistry*. 25th ed. Stamford, Connecticut: Appleton & Lange.

- Naga A.P. and Siddiqui A. 2011, *Nanomedical platform for drug delivery*. J. Nanomed. Nanotechnol. 2:122.

- Nakamoto K., 2009, *Infrared and Raman Spectra of Inorganic and Coordination Compounds: Applications in coordination, organometallic, and bioinorganic chemistry. Part 2, Infrared and Raman Spectra of Inorganic and Coordination Compounds.* New Jersey :John Wiley & Sons.

- Niemeyer, C. M. 2001, *Nanoparticles, Proteins, and Nucleic Acids: Biotechnology Meets Materials Science.* Angew. Chem. 40:4128-4158.

- Nikl M. 2006, *Scintillation detectors for X-rays*. Meas. Sci. Technol. 17: R37–R54.

- Nitsch K., Cihlar A., Klimm D., Nikl M. and Rodová A. 2005, *Na-Gd phosphate glasses: Preparation, thermal and scintillating properties.* Therm. Anal. Calorim. 80: 735-738.

- Oberdorster E. 2004, *Manufactured nanomaterials (Fullerenes C_{60}) induce oxidative stress in the brain of juvenile largemouth bass.* Environmen. Healt. Perspect. 112:1058-1062.

- Omura N. E., Jeffrey S. Dover, Kenneth A. Arndt and Arielle N. B. Kauvar. 2003, *Treatment of reticular leg veins with a 1064 nm long-pulsed Nd:YAG laser*. J. Acad. Dermatol. 48:76-81.

- Oviedo M.J., Contreras O., Rodriguez C.E., Macedo Z.S., Hirata G.A. and McKittrick J. 2012, *Photo- and radioluminescence characteristics of bismuth germanate nanoparticles by sol–gel and pressure-assisted combustion synthesis*. Opt. Mater. 34:1116-1119.

- Parham P. 1979, *Use of a monoclonal antibody (W6/32) in structural studies of HLA- A,B,C, antigens*. J. Immunol. 123: 342-349.

- Park Ji-Ho, Gu Luo, Vo Maltzahn Geoffrey, Ruoslahti Erkki and Bhatia Sangeeta. 2009, *Biodegradable luminescent porous silicon nanoparticles for in vivo applications*. Nature 8:331-336.

- Paschalis E.P., Zhao Q., Tucker B.E., Mukhopahayay S., Bearcroft Fowler BO. 1995, *Degradation potential of plasma-sprayed hydroxyapatite-coated titanium implants* J. Biomed. Mater. Res. 12:1499-14505.

- Paschalis EP, Zhao Q, Tucker BE, Mukhopadhayay S, Bearcroft JA, Beals NB, Spector M, Nancollas GH. 1995, *Degradation potential of plasma-*

sprayed hydroxyapatite-coated titanium implants. J. Biomed. Mater. Res. 29(12):1499-505.

- Peppas N. A. and Langer R. 1994, *New challenges in biomaterials*. Science 263: 1715-1720.

- Perera F.P. and Weinstein I.B. 2000, *Molecular epidemiology: recent advances and future directions*. Carcinogenesis 21:517–524.

- Person M., Madsen J., Ostergaard S., Ploug M. and Kjaer A. 2011, *^{68}Ga-labeling and in vivo evaluation of a uPAR binding DOTA-and NODAGA-conjugated peptide for PET imaging of invasive cancers*. Nuclear Med. And Biol. Article in press.

- Philp D., Stoddart J. F. 1996, *Selbstorganisation in natürlichen und in nichtnatürlichen Systemen.* Angew. Chem., 108:1242-1286.

- Pimpinelli and J. Villain. 1998, *Physics of Crystal Growth*. Cambridge University Press.

- Polosan S. 2010, *Dynamics of energy absorption versus crystallization in $Bi_4Ge_3O_{12}$ (BGO) amorphous materials*. Mat. Res. Bull. 45:1492-1495.

- Polosan S. and Secu M. 2010, *X-ray excited luminescence and photoluminescence of $Bi_4(GeO_4)_3$ glass-ceramics*. Radiation Measurements. 45:409-411.

- Polosan S., Apostol E., Secu M. and Aldica G.H. 2005, *BGO glasses: Structural and optical characterization*. Phys. Stat. Solid. 2:93-96.

- Posner A.S., Perloff A. and Diorio A.D. 1958, *Refinement of the hydroxyapatite structure*. Acta Cryst. 11:308.

- Pramanik S., Agarwal A.K., Rai K.N. and Garg A. 2007, *Development of high strength hydroxyapatite by solid-state-sintering process*. Ceramics Int. 33: 419-426.

- Rahman T. 2010, *Introduction to flow cytometry*. ABD serotec Manual.

- Ranganathan R, Madanmohan S, Kesavan A, Baskar G, Krishnamoorthy YR, Santosham R, Ponraju D, Rayala SK, Venkatraman G. 2012, *Nanomedicine: towards development of patient-friendly drug-delivery systems for oncological applications*. Int. J. Nanomedicine. 7:1043-60.

- Ranganathan R, Madanmohan S, Kesavan A, et al. 2012, *Nanomedicine: towards development of patient-friendly drug-delivery systems for oncological applications*. Int J Nanomedicine. 7:1043–1060.

- Ratner B. D.,Hoffman A. S., Schoen J. F. and Lemons. 1996, *J. E. Biomaterials Science, an Introduction to Materials in Medicine.* 1-8.

- Rauschmann M.A., Wichelhaus T.A., Stirnal V., Dingeldein E., Zichner L., Schnettler R. and Alt V. 2005, *Nanocrystalline hydroxyapatite and calcium sulphate as biodegradable composite carrier material for local delivery of antibiotics in bone infections*. Biomaterials 26: 2677-2684.

- Remacle F., Levine R. D. *Quantum Dots as Chemical Building Blocks: Elementary Theoretical Considerations.* 2001, Chem.Phys.Chem. 2: 21- 36.

- Rhee S.H. 2002, *Synthesis of hydroxyapatite via mechanochemical treatment*. Biomaterials 23: 1147-1152.

- Robert N.J., Vogel C.L., Henderson I.C. 2004, *The role of the liposomal anthracy-clines and other systemic therapies in the management of advanced breast cancer.* Semin. Oncol. 31:106-146.

- Rodnyi P.A. 1997, *Physical Processes in Inorganic Scintillators* (New York: CRC Press).

- Rojas S.S., De Souza J.E., Andreeta M.R.B. and Hernandes C. 2010, *Influence of ceria addition on termal properties and local structure of bismuth germanate glasses.* J. of Non-Crystall. Sol. 356: 2942-2946.

- Schmid G. 1994, *Clusters and Colloids*, Wiley. Weinheim.

- Serbinova W, Kwaja S, Reznick AZ and Packer L. 1992, *Handbook of antioxidants Free Radical*. Res. Commun. 17:49.

- Sharifian H. and Gharekhanloo F. 2003, *Evaluation of average diameter of lower extremity veins in acute and chronic thrombosis and comparison with normal persons by Doppler sonography*. Acta. Medica. Iranica. 41:180-182.

- Shepherd J.A., Gruner S.M., Tate M.W. and Tecotzky M. 1997, *Study of afterglow in x-ray phosphors for use on fast-framing charge-coupled device detectors*. *Opt. Eng.* 36: 3212–22.

- Spedding F. H. and Daane A. H. 1971, *The Rare Earths*. Wiley, New York.

- Stadtman E.R. and Oliver CN. 1991, *Metal-catalyzed oxidation of proteins*. J. Biol. Chem. 266: 2005-2008.

- Straubinger R.M., Lopez N.G., Debs R.J., Hong K. and Papahadjopoulod D. 1988, *Liposome-based therapy of human ovarian cancer: parameters determining potency of negatively charged and antibody-targeted liposomes.* Cancer Res. 48: 5237-5245.

- Subbiah R, Veerapandian M, Yun KS. 2010, *Nanoparticles: functionalization and multifunctional applications in biomedical sciences*. Curr. Med. Chem.17: 4559-77.

- Sun S., Murray C. B., Weller D., L. Folks, A. Moser. 2000, *Monodisperse FePt Nanoparticles and Ferromagnetic FePt Nanocrystal Superlattices* Science 287: 1989-1992 .

- Tadic D. and Epple M. A. 2004, T*horough physicochemical characterisation of 14 calcium phosphate-based bone substitution materials in comparison to natural bone*. Biomaterials 25: 987–94.

- Tamerler C, Sarikaya M. 2009, *Molecular biomimetics: nanotechnology and bionanotechnology using genetically engineered peptides*. Philos Transact A Math. Phys. Eng. Sci. 367: 1705-26.

- Taton T.A., Mirkin C.A., Letsinger R.L. 2000, *DNA array detection with nanoparticles probes*. Science 289: 1757-1760.

- Taxak V.B., Khatkar S.P., Han S.D., Kumar R. and Kumar M.. 2009, *Tartaric acid-assisted sol–gel synthesis of Y2O3:Eu3+ nanoparticles*. J. Alloy. Comp. 469: 224.

- Ternane R., Trabelsi-Ayedi M., Kbir-Ariguib N. and Piriou B. 1999, *Luminescent properties of Eu^{3+} in calcium hydroxyapatite*. J. Lumin. 81:165–70.

- Toriyama M., Ravaglioli A., Krajewski A., Celotti G. and Piancastelli A. 1996, *Synthesis of hydroxyapatite – based powders by mechano-chemical method and their sintering*. J. Eur. Ceram. Soc. 16:429–36.

- Townley C.O. 1995, *Bioceramics: Materials and Applications*. Edited by G. Fishman, A. Clare and L.L. Hench (Ceram. Trans. 48, The American Ceramic Society, Westerville, OH, 23.

- Uchida A, Shinto Y, Araki N, Ono K. 1992*, Slow release of anticancer drugs from porous calcium hydroxyapatite ceramic.* Journal of Orthopaedic 10: 440-445.

- Vacanti, C. A. 2001, MRS Bulletin, 26:798.

- Valais I.G., Michail C.M., David S.L., Konstantinidis A., Cavouras D.A., Kandarakis I.S. and Panayiotakis G.S. 2008, *Luminescence Emission Properties of (Lu; Y)2SiO_5:Ce (LYSO:Ce) and (Lu; Y)AlO_3:Ce (LuYAP:Ce) Single Crystal Scintillators Under Medical Imaging Conditions*. IEEE Nuclear Sci. 55: 785.

- Valerio M. E.G., Jackson R. A. and Z.S. Macedo 2005, *Modelling intrinsic defects and transport mechanisms in the bismuth germanate crystalline system*. Phys. Stat. Sol. 2: 485-489.

- Van Eijk C.E.W. 2002, *Inorganic scintillators in medical imaging*. Phys. Med. Biol. 47:R85.

- Von Recum, A.F. and LaBerge, M. 1995, *Educational Goals for Biomaterials Science and Engineering: Perspective View*, J. of Appl. Biomat. 6: 137-144.

- Wagner S., Rothweiler F., Anhorn M., Sauer D., Riemann I., Weiss E., Katsen-Globa A., Michaelis M., Cinatl Jr J., Schwartz., Kreuter J., Von Briesen H. and Langer K. 2010, *Enhanced drug targeting by attachment of an anti av integrin antibody to doxorubicin loaded human serum albumin nanoparticles* ,Biomaterials 31: 2388–2398.

- Walsh WR, Guzelsu N. 1994, *Compressive properties of cortical bone: mineral-organic interfacial bonding.* Biomaterials 15:137-45.

- Wang M, Thanou M. 2010, *Targeting nanoparticles to cancer*. Pharmacol. Res. 62:90-9.

- Weber M.J. and Monchamp R.R. 1973, *Luminescence of $Bi_4Ge_3O_{12}$: Spectral and decay properties*. J. Appl. Phys. 44: 5495-5499.

- Whitesides G. M., Mathias J. P., Seto C. T.1991, *Molecular self-assembly and nanochemistry: a chemical strategy for the synthesis of nanostructures* Science. 254:1312-1319.

- Williams D.F. Definition in biomaterials. Elsevier, Amsterdam 1987.

- Wright A.O., Seltzer M.D., Gruber J.B. and Chai B.H.T. 1995, *Site-selective spectroscopy and determination of energy levels in Eu^{3+}-doped strontium fluorophosphates*. J Appl. Phys. 78:2456–67.

- Xiaohu Gao, Yuanyuan C, Levenson R, Chung L.W. and Nie S. 2010, *In vivo cancer targeting and imaging with semiconductor quantum dots*. Nature Biotech. 22:8.

- Y. Xiao, X. Gao, G. Gannot, M.R. Emmert-Buck, S. Srivastava, P.D. Wagner, M.A.Amos and P.E. Barker. *Quantitation of HER2 and telomerase biomarkers in solid tumors with IgY antibodies and nanocrystal detection*. International Journal of Cancer, posted online Jan. 23, 2008.

- Yamasaki N, Kai T, Nishioka M, Yanagisawa K, Ioku K. Porous Nishioka M. Yanagisawa K. and Ioku K. 1990, *Porous hydroxyapatite ceramics prepared by hydrothermal hot- pressing*. J. of Mater. Scien. Lette. 9:1150-1151.

- Yan G., Donglu S., Lian J., Zhongyun D., Wang W., Cho H., Liu G., Wang L. and Ewing R., 2008, Quantum dot conjugated hydroxylapatite nanoparticles for in vivo imaging. Nanotechnology. 19: 175102-6.

- Yanagisawa K, Yamasaki N. 1990, *Solidification of Glass Powder with Simulated High-Level Radioactive Waste During Hydrothermal Hot-Pressing*. J. of the Ameri. Ceram. Soc. 73(2):317-322.

- Yang H. and Xia Y. 2007, *Biotechnology: Enabling biomedical research with nanomaterials.* Adv. Mat. 19: 3085-3087.

- Yang P., Quan Z., Li C., Kang X., Lian H. and Lin J. 2008, *Bioactive, luminescent and mesoporous europium-doped hydroxyapatite as a drug carrier*. Biomaterials 29:4341-4347.

- Zhu G., Zhu X., Fan Q. and Wan X. 2011, *Raman spectra of amino acids and their aqueous solutions*. Spectectrochimica Acta. Part A Molec. And Biomol. Spec. 78:1187-1195.

- Zounani A., Zambon D. and Cousseins J.C. 1992, *Optical properties of Eu^{3+} activated $Sr_{10}F_2(PO_4)_6$ elaborated by coprecipitation*. J. Alloys. Compd. 188: 82–6.

Glossary

- **Antibody:** A blood protein produced by the body in response to and counteracting an antigen.
- **Antigen:** Molecule that is able to provoke an immune response
- **Biocompatible:** Is the ability of a material to perform with an appropriate host response in a specific situation
- **Bioactive:** The ability to integrate in bone structures and support bone ingrowth, without breaking down or dissolving.
- **Cell:** The smallest structural and functional unit of an organism, consisting of cytoplasm and a nucleus enclosed in a membrane.
- **Cysteine:** Is an amino acid with the chemical formula $HO_2CCH(NH_2)CH_2SH$, a building block of proteins that are used throughout the body.
- **Disease:** A disorder of structure or function in a human, animal, or plant especially one that produces specific symptoms or that effects a specific part.
- **Epidemiology:** the branch of medicine concerned with the incidence and distribution od diseases and other factors relating to health.
- **Hydrolysis:** Cleavage of a covalent bond with accompanying addition of water, -H being added to one product of the cleavage and –OH to the other.

- **Latency:** The time between exposure to a pathogen, chemical or radiation, and when symptoms first become apparent.

- **Ligand:** A molecule that binds to another. Often, a soluble molecule such as a hormone or neurotransmitter that binds to a receptor.

- **Leukemia:** Is a type of cancer of the blood or bone marrow characterized by an abnormal increase of immature white blood cells called blasts.

- **Osteoconductive:** Occurs when the bone graft material serves as a scaffold for new bone growth that is perpetuated by the native bone.

- **Pathogen:** An organism or order agent that causes disease.

- **Serum:** Is the component that is neither a blood cell (serum does not contain white or red blood cells) nor a clotting factor; it is the blood plasma with the fibrinogensremoved. Serum includes all proteins not used in blood clotting (coagulation) and all the electrolytes, antibodies, antigens, hormones, and any exogenous substances (e.g., drugs and microorganisms).

- **Tissue:** Is a cellular organizational level intermediate between cells and a complete organism. A tissue is an ensemble of cells, not necessarily identical, but from the same origin, that together carry out a specific function. These are called tissues because of their identical functioning.

- **Treatment:** Administration or application of remedies to a patient or for a disease or injury.

- **Urine:** The waste product secreted by the kidneys that in mammals is a yellow to amber-colored, slightly acid fluid discharged from the body through the urethra.